

ULTRA THIN FILMS FOR SENSING AND HEATING OF MICROPROBES

Proefschrift

ter verkrijging van de graad van doctor
aan de Technische Universiteit Delft,
op gezag van de Rector Magnificus prof.ir. K.C.A.M. Luyben,
voorzitter van het College voor Promoties,
in het openbaar te verdedigen

op woensdag 18 september 2013 om 15.00 uur

door

Angelo GAITAS
Master of Science, University of London - Royal Holloway
geboren te Athens, Griekenland

Dit proefschrift is goedgekeurd door de promotoren:

Prof.dr. P.J. French

Prof.dr. Y.B. Gianchandani

Samenstelling promotiecommissie:

Rector Magnificus,	voorzitter
Prof.dr. P.J. French,	Technische Universiteit Delft, promotor
Prof.dr. Y.B. Gianchandani,	University of Michigan, promotor
Prof.dr. G.J.M. Krijnen	Universiteit Twente
Prof.dr.ir. H.S.J. van der Zant	Technische Universiteit Delft
Prof.dr.ir. R. Dekker	Technische Universiteit Delft
Dr.ir. A. Bossche	Technische Universiteit Delft
Dr. C.K. Yang	Mapper Lithography
Prof.dr. G.Q. Zhang	Technische Universiteit Delft, reservelid

This research was funded by PicoCal Inc. through funding from the National Science Foundation and the National Institutes of Health.

Printed by Ipskamp Drukkers

ISBN 978-94-6191-881-9

Copyright © 2013 A. Gaitas.

All rights reserved. No part of this publication may be reproduced, stored in a retrieval system, or transmitted, in any form or by any means, electronic, mechanical, photocopying, recording, or otherwise, without the prior permission in writing from the proprietor.

Alle rechten voorbehouden. Niets uit deze uitgave mag worden verveelvoudigd, opgeslagen in een geautomatiseerd gegevensbestand, of openbaar gemaakt, in enige vorm of op enige wijze, hetzij elektronisch, mechanisch, door fotokopieën, opnamen, of op enig andere manier, zonder voorafgaande schriftelijke toestemming van de rechthebbende.

Contents

1	Introduction.....	1
1.1	Micro-cantilevers for deflection and thermal sensing.....	2
1.1.1	Deflection sensing	2
1.1.2	Thermal applications	3
1.1.3	Advantages of metal film elements	4
1.2	Motivation and summary of work.....	6
1.2.1	Key findings	7
1.3	Organization of this thesis.....	9
2	Overview of micromachining	11
2.1	Introduction	12
2.2	Photolithography	12
2.3	Surface micromachining	13
2.4	Bulk micromachining.....	15
2.5	Conclusions	18
3	Overview of micro-cantilevers	19
3.1	Introduction	20
3.2	Detection of cantilever movement	20
3.3	Operation.....	23
3.4	Conclusions	26
4	Design and fabrication of devices.....	27
4.1	Thermal modeling	28
4.3	Mechanical and piezoresistive modeling	33
4.4	Silicon cantilever devices.....	40
4.4.1	Designs	40

4.4.2 Fabrication	42
4.5 SiO ₂ /Si ₃ N ₄ /SiO ₂ cantilever	47
4.5.1 Designs	47
4.5.2 Fabrication	48
4.6 Polyimide cantilevers	51
4.6.1 Designs	51
4.6.2 Fabrication	52
4.7 Conclusions	54
5 Temperature sensitivity of thermal probes	55
5.1 Introduction	56
5.2 Scanning thermal probe.....	58
5.3 Gold wire calibration.....	61
5.3.1 Device & fabrication	61
5.3.2 Noise thermometry	62
5.4 Experimental results and discussion	66
5.4.1 Thermal probe calibration and hot-spot scans.....	66
5.4.2 FEA simulations	69
5.5 Conclusions	73
6 Thin film deflection sensor for material characterization.....	75
6.1 Introduction	76
6.2 Cantilever mechanics, the gauge factor, and noise	77
6.2.1 Cantilever mechanics and the gauge factor	77
6.2.2 Noise.....	81
6.3 Experimental set-up.....	82
6.4 Experimental results and discussion	84
6.5 Conclusions	90

7	A Piezo-thermal probe for thermomechanical analysis	91
7.1	Introduction	92
7.2	Heat transfer between cantilever tip and substrate	93
7.3	Scanning system	97
7.4	Experimental results and analysis	98
7.4.1.	Displacement sensing	98
7.4.2.	Thermomechanical analysis	99
7.4	Conclusions	102
8	Probe array for high throughput applications	105
8.1	Introduction	106
8.2	Element characterization and probe-sample contact	107
8.3	Topographical scanning	109
8.4	Thermo-mechanical applications	110
8.5	Conclusions	113
9	Tip-based chemical vapor deposition	115
9.1	Introduction	116
9.2	Device and experimental set-up	117
9.3	Experimental results and discussion	118
9.4	Conclusions	120
10	A Polymer micro-cantilever for explosive detection	123
10.1	Introduction	124
10.2	Coating for explosive adsorption	127
10.3	Characterization of the cantilever sensor	130
10.4	Explosive detection	131
10.5	Conclusions	134
11	Thin metal microbolometers for SThM	135

11.1 Introduction	136
11.2 Measurements and results of titanium thin films	138
11.3 Measurements and results of tungsten thin films	143
11.4 Scanning thermal microscopy	147
11.5 Conclusions	149
12 Conclusions and future research	151
12.1 Future work	155
Appendix 1. Fabrication processes	157
1. Fabrication of silicon cantilever	157
2. Fabrication of silicon nitride cantilever	158
3. Fabrication of polyimide cantilever	159
Bibliography	161
Summary	177
Samenvatting	179
Acknowledgements	181
List of Publications	183
About the author	187

1

Introduction

This dissertation aims to advance the current state of cantilevers with integrated metal thermal (heater) and deflection sensing elements. To this end, the research consists of exploring the properties of thin films with thicknesses of 100 nm or less and studying a number of applications in thermal sensing, micro-heating, and deflection sensing. In detail the goals are to: a) enhance the performance of metallic sensors used in scanning probe microscopy; b) study ultra thin metal films and how can these be used as sensing elements for deflection sensing (scanning probe topography, explosive detection, biomaterial detection), thermal sensing, heating, and other applications; c) simplify the sensing instrumentation (such as atomic force microscopes and chemical and biological detection systems) by embedding various sensing mechanisms on the cantilever. In order to achieve these goals a number of novel microfabrication processes were developed. In addition, various applications in scanning probe microscopy and micro-cantilever sensing have been presented.

1.1 Micro-cantilevers for deflection and thermal sensing

1.1.1 Deflection sensing

Scanning probe methods developed during the last three decades offer high-resolution images of sample properties. First introduced by G. Binnig et al. in 1986 [Binnig, 1986], scanning probe microscopes (SPM) measure properties such as topographical variations, thermal conductance, temperature, capacitance, optical absorption, frictional forces, or magnetic field at localized spots. The SPM has been a very successful research tool. Due in part to their high sensitivity [Pinnaduwege, 2005; Li, 2007; Berger, 1997; Fritz, 2000; Moulin, 2000] microcantilevers are used in a number of applications including SPM and atomic-force microscopy (AFM) [Albrecht, 1990], material characterization such as thermomechanical analysis (TMA) [Hammiche, 2001; Price, 1999; Hammiche, 2000], nanolithography [Majumdar, 1992], high-density data storage [Mamin, 1992; Mamin, 1995], biological sensing [Florin, 1995], cell elastography [Costa, 2004], measurement of material properties such as adhesion, stiffness, elasticity and viscosity [Bhushan, 1999], and in trace chemical detection including in the area of explosives detection [Fair, 1999].

The optical lever method [Meyer, 1988] is commonly used to detect nanoscale bending of cantilevers in atomic force microscopy (AFM) and in chemical sensing [Moulin, 2000]. However, this method requires a bulky optical setup, which results in lack of portability and high manufacturing costs. There are also challenges associated with applying the optical lever method when the cantilever is in liquid environments or when the cantilever is too small to reflect the laser.

In an effort to address these deficiencies, piezoresistive deflection-

sensing elements are integrated onto micromachined cantilevers to increase sensitivity, and reduce complexity and cost. These sensing elements are made by selectively doping silicon [Chui, 1996; Chui, 1998; Tortonese, 1993], by depositing and patterning metal or metal oxide films, such as gold [Li, 2007; Calleja, 2003; Arlett, 2010], indium tin oxide [Wisitsoraat, 2007; Gregory, 2003], and nichrome [Allen, 2009], or by depositing and patterning other materials such as amorphous carbon [Peiner, 2006].

1.1.2 Thermal applications

Thermal measurements at the nanometer scale are of both scientific and industrial interest. In the past three decades, scanning microscopy using thermally sensitive probes has been applied to a variety of applications. For instance, scanning thermal microscopy (SThM) has been used in lithography research, in cell biology applications [Ocola, 96; Li, 2001; Li, 2003], in material characterization [Hammiche, 1996; Gaitas, 2006], Joule heating [Luo, 1996], material variations in semiconductor devices [Lai, 1995], subsurface imaging of metal particles [Hammiche, 1996], data storage and several other applications [Vettiger, 2000; Lerchner, 2000; Majumdar, 1999].

Various thermal probes have been developed since the invention of SThM by Williams and Wickramasinghe in 1986 [Williams, 1986]. These probes use a metal or semiconductor film bolometer for measuring the temperature at the tip. In order to operate effectively, microbolometers must have a high temperature coefficient of resistance¹ (TCR) and low noise characteristics. In addition, the materials used to manufacture microbolometers must be inexpensive and compatible with current CMOS processes.

¹ The TCR of a material is defined as "the increase in the resistance of a 1 Ω resistor of that material when it is subjected to a rise of temperature of 1 K" [Bird, 2012] and is used to measure the sensitivity of a bolometer.

These are the primary conditions that have to be met as part of the continuing effort to develop even smaller, better performing microbolometers.

To date, various materials have been used to fabricate microbolometers. Polycrystalline and amorphous silicon have a high temperature coefficient of resistance (up to 0.05/K) but exhibit adverse noise characteristics [Hull, 1999; Eminoglu, 2003; Henini, 2002]. Vanadium oxide, on the other hand, has a TCR of approximately 0.05 /K and a superior noise equivalent temperature difference (NETD). However, vanadium oxide introduces a significant number of deposition problems [Henini, 2002; Ryu, 2008; Wood, 1993]. Thin film metallic microbolometers, in contrast, have very low noise characteristics. However, bulk metallic films have low TCR (0.005/K) [Block, 1973; Li, 2000; Henini, 2002].

1.1.3 Advantages of metal film elements

Compared with doped-silicon sensing elements, metal film elements have important advantages including simplified fabrication, a lower manufacturing cost [Zhu, 2011], and the capability to scale down to smaller dimensions while maintaining sensitivities [Li, 2007] and exhibiting lower noise. Metallic sensing elements also enable the use of alternative substrate materials (such as polymers), that tend to exhibit higher compliance properties, improved thermal isolation, and are more robust (less brittle) compared to Si or Si₃N₄ cantilevers [Li 2, 2001; Johansson, 2005; Gaitas, 2009].

Metal film sensing elements with thickness larger than 10 nm exhibit bulk material behavior and typically have gauge factors² of about 2 or smaller [Li, 2007; Calleja, 2003; Johansson, 2005; Li, 2000]. Ultrathin metal film sensing elements with thickness less than 10 nm have demonstrated increased piezoresistive sensitivity [Li, 1994]. The gauge factor increases with decreasing thickness with ultrathin discontinuous films having larger resistances and higher gauge factors [Knight, 1969; Witt, 1974]. When the film is thin enough so that the film thickness is less than the mean free path of the free electrons then the gauge factor increases sharply [Jen, 2003].

The electrical properties of granular metals vary as the composition of a metal and non-metal mixture changes [Adkins, 1997]. Metal deposition goes through four phases before it starts behaving like a bulk film: nucleation, island formation, formation of island networks, and formation of continuous (but porous) film [Nowroozi-Esfahani, 1990; Chopra, 1979; Matthews, 1983; Neugebauer, 1962]. The first three phases are considered discontinuous. Typically, island films have negative temperature coefficient of resistance (TCRs) while porous films have a positive TCR [Nowroozi-Esfahani, 1990; Chopra, 1979; Esfahani, 1992; Morris, 1977; Wetzig, 2006]. However, the TCR for porous films is lower than that of a thick bulk film. It is well established that there exists a metal-insulator or a superconductor-insulator transition as a function of film thickness for metal films at cryogenic temperatures. It is interesting to note that this transition typically occurs for films with a resistance on the order of quantum resistance.

² The gauge factor of a strain gauge is defined as "the ratio of relative change in electrical resistance to the mechanical strain ϵ . ϵ is the relative change in length" [Harsányi, 2000] and is widely used as a measure of sensitivity.

1.2 Motivation and summary of work

In this work thin metal films will be evaluated. The gauge factor, resistance, film thickness, and TCR will be quantified in order to determine the usefulness of these sensors in several industrial and commercial applications. In this thesis ultrathin films are films with thicknesses of 100 nm or less. Gold is used initially because of its non-corrosive nature and good electrical conductivity. Titanium, irridium, and tungsten were also studied as heating and bolometric materials for scanning thermal probes.

This dissertation aims to advance the current state of cantilevers with integrated thin film metal elements (≤ 100 nm). To this end, the research consists of exploring the properties of thin films with thicknesses of 100 nm or less and studying a number of applications in thermal sensing, micro-heating, and deflection sensing. As described above thin metal elements on cantilevers offer several advantages. However, the performance of these elements has not been studied at thicknesses less than 10 nm for industrial and research applications.

There are several unanswered challenges that this thesis will address:

- a) Can ultrathin metal films meet the sensitivity requirements to be used as bolometers and scanning thermal probes? As described above, ultra thin films during their first three phases of the four-phase deposition exhibit a negative TCR. One motivation is to explore the maximum lower negative bound of TCR and examine if it is universal for metals.
- b) Can ultrathin metal films meet the deflection sensing requirements to be used in scanning probe microscopy and chemical sensing applications? Past research has indicated that the gauge factor increases with decreasing thickness, but these

findings have not been combined with state-of-the-art cantilevers in order to address applications in scanning probe microscopy.

c) Can these devices be used for industrial applications simplifying already established processes offering an inexpensive or improved performance alternative?

The following will be studied: a) the sensitivity of thermal sensing using scanning micro-cantilever probes with 10 nm metal sensing elements; b) deflection sensing of scanning micro-cantilever probes with 5 nm and 10 nm metal sensing elements and their application in material characterization; c) the integration of thermal and deflection sensing mechanisms on a micro-cantilever with applications in material characterization; d) the scaling to an array of integrated thermal and deflection sensing mechanisms with applications in scanning probe microscopy; e) the use of micro-cantilevers for chemical vapor deposition reactions at the nanoscale; f) the integration of a sensing element on a polymer micro-cantilever used in explosive detection; g) the study of increasingly thinner metal films (<10 nm) at the metal-insulator transition regime in order to enhance the temperature coefficient of resistance of micro-bolometers for scanning thermal microscopy. In order to achieve these goals a number of microfabrication processes were developed.

1.2.1 Key findings

The minimum detectable temperature change of a 10 nm thin film cantilever thermal sensor is 0.4 K, corresponding to 17 ppm changes in probe resistance. Finite element analysis simulations indicated that a bow-tie metallization design could yield an additional 5- to 7-fold increase in sensitivity.

The piezoresistance³ (elastoresistance) is considerably enhanced from bulk gold with gauge factor of 2 and from the reported 2.6 for 30 nm thin films [Li, 1994]. The gauge factor was 3.24 for the 10 nm sensor and 4.1 for the 5 nm sensors, doubling from the bulk gold.

Thin film properties near the metal-insulator transition (MIT) regime (thicknesses < 10 nm and in some cases < 2 nm) have shown improved thermal sensitivity of microbolometers, with the temperature coefficient is greatly enhanced approaching 0.95%/K.

The cantilevers operate without the need of a complicated optical lever required by AFM systems. In addition, the cantilevers have a very large dynamic range of tens of microns. This feature enables monitoring movement of tens of microns in the out-of-plane axis (Z-axis), which allows for a deeper insight into the mechanical properties of materials. These devices are used for thermomechanical analysis (TMA) by successfully integrating two separate elements on one cantilever. These devices are scaled to a 7-cantilever array and used for high throughput melting point measurements, material characterization of mechanical properties, and scanning probe microscopy.

Manufacturing of individual nanostructures was achieved with a moving nano-heater that directs a chemical vapor deposition reaction (nano-CVD) demonstrating a tip-based nanofabrication (TBN) method. Localized nano-CVD of copper (Cu) and copper oxide (CuO) on a silicon (Si) and silicon oxide (SiO₂) substrate from gasses is demonstrated. This technique is applicable to other materials.

³ Although the right term is elastoresistance, in this thesis as with many other publications, the term piezoresistance is used for gold deflection sensing.

A polyimide cantilevers with a thin metallic sensing elements is used to detect tri-nitro-benzene (TNB) in vapor phase via process that involves a change in the surface stress of the cantilever. The level of sensitivity is greatly enhanced by x 30 compared to what was previously found when the colorimetric sensing material is used alone.

1.3 Organization of this thesis

Chapters 2 and 3 provide an overview of micromachining and micro-cantilevers respectively. Chapter 4 presents the designs of the cantilevers that were fabricated including various simulations that helped improve the designs. Then three different fabrication processes are described in detail.

Chapter 5 presents a novel method for calibrating a thin film (≤ 10 nm) thermal probe using a precalibrated gold wire. Using this method the minimum detectable temperature change on the substrate using the thermal sensing element was measured at 0.4 K, corresponding to 17 ppm changes in probe resistance. In chapter 6 a silicon cantilever with an ultrathin film (≤ 5 nm) deflection sensor made of gold is presented for scanning probe microscopy and material characterization. The sensor has a gauge factor of twice as much as that of bulk gold. Chapter 7 describes a silicon cantilever that integrates both a deflection sensor and a thermal sensor made of thin gold films (≤ 10 nm) used for thermomechanical analysis. Chapter 8 presents an array of cantilevers like the ones described in chapters 5, 6, and 7 for high throughput applications.

Chapter 9 presents the manufacturing of individual nanostructures with a moving nano-heater made of thin metal film (≤ 100 nm) that

directs a chemical vapor deposition reaction (nano-CVD) demonstrating a tip-based nanofabrication (TBN) method.

Chapter 10 employs the concepts of ultrathin film gold (≤ 10 nm) deflection sensing developed earlier integrated on a polyimide cantilever and used for vapor explosive detection.

Chapter 11 presents thin metal microbolometers made of tungsten and titanium near the metal-insulator transition regime (≤ 100 nm) where the temperature coefficient of resistance increases to 0.95%/K. These findings were used to develop silicon nitride cantilevers for scanning thermal microscopy.

Chapter 12 concludes the thesis with a summary of the work and with future applications and directions in research and development.

2

Overview of micromachining

The devices used in this thesis are based in micro- or nano- electro-mechanical systems (MEMS or NEMS) technology and fabricated with micromachining methods. In MEMS (or NEMS) integrated circuit (IC) batch processing techniques are used to produce miniature devices that have mechanical and electrical parts with feature sizes from a few nanometers to millimeters. These devices are able to sense and actuate and are commercially found in airbags, blood pressure sensors, inkjet printer heads, projection display chips, computer disk drive read/write heads, biosensors, micro-cantilevers for scanning probe microscopy and many more products. In this chapter the basic fabrication methods will be introduced.

2.1 Introduction

MEMS fabrication can be subdivided into three categories: bulk micromachining, surface micromachining and high-aspect-ratio micromachining. For the devices developed in this thesis the first two are needed and thus will be described. This chapter will focus on the techniques used to fabricate the devices presented. First photolithography is described, then bulk and surface micromachining are described including the materials used, the deposition techniques, and the etching techniques. Packaging, passivation, and encapsulation are not discussed since the devices developed are used in laboratory settings.

2.2 Photolithography

In photolithography a pattern is transferred on the surface of a silicon wafer. Typically the wafer is covered with a dielectric material such as silicon dioxide. A layer of photoresist, which is a light sensitive polymer, is deposited. A photomask is brought in contact with the wafer. The mask is a glass plate with chromium patterns. Ultraviolet radiation exposes the areas of the photoresist where there are no mask patterns. There are two types of photoresist: positive photoresist that gets stronger with radiation exposure and negative that gets weaker. Following exposure, the film is developed by using a solution to remove the exposed or unexposed areas depending on the kind of photoresist used. In the gap that is created a material such as a metal can be deposited. Buffered oxide etch (BOE, a.k.a. buffered HF) may be used to remove the oxide layer underneath. Then the remaining photoresist is removed with a heated remover solution. Ultrasonic vibrations may be used to expedite the removal, as well as IPA and DI water to clean the wafer before drying.

2.3 Surface micromachining⁴

Surface micromachining entails depositing thin films and selectively removing them to yield free standing structures. The process is shown in Fig. 2.1, although this can be augmented with additional sacrificial and mechanical layers. There are many combinations of sacrificial and mechanical layers. Stress control is important, and low tensile stress and a minimum stress profile is preferred [Guckel, 1988]. Releasing without stiction is another important issue that is addressed by freeze-drying, super critical drying, vapor-etching, and dry etching.

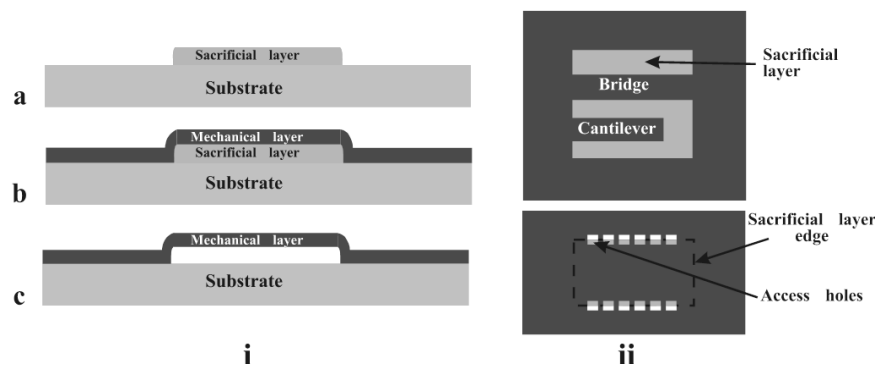


Fig. 2.1. Basic Surface micromachining process [French, 2005], (ia) deposition and patterning of sacrificial layer, (ib) deposition and patterning of mechanical layer and (ic) sacrificial etching, (ii) lateral view of typical structures.

Typically silicon is used as a substrate material. Si_xN_y , SiO_2 , SiC are used as device materials or insulators. A variety of metals and compounds are widely used, examples are Au, Cu, Al, ZnO, W, etc. and various organic materials such as polymers [Kovacs, 1998]. Polymers are typically deposited using casting. In casting a

⁴ Parts of 2.2 including Fig. 2.1 were adapted from [French, 2005] with the author's permission.

material is sprayed or spun, creating a thin film on the substrate. In addition to polymers such as polyimide, casting is also used for photoresist.

In surface micromachining, silicon is used as a foundation layer upon which the devices are built by adding layers that are used as structural layers or are removed and thus act as sacrificial layers. Figure 2.2 is an example of a cantilever that is suspended after removing a sacrificial layer of titanium.

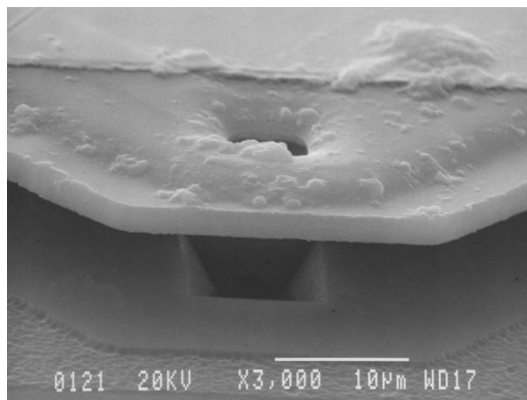


Fig. 2.2. A surface micromachined cantilever is shown. The top suspended part is made of polyimide, while the bottom part is silicon oxide and silicon. The cantilever also includes a tip as seen in the SEM picture. A notch is formed by anisotropic wet etching. The sacrificial material is Ti and it is removed with 5% HF.

There are several methods to deposit materials. In chemical vapor deposition (CVD) a substrate is immersed in a chamber and gases are inserted. These gases react and deposit on the substrate. Variations of CVD include low pressure CVD (LPCVD) and plasma enhanced CVD (PECVD). CVD can be used for polysilicon, silicon dioxide, silicon nitride, synthetic diamond, carbon nanotubes and several other materials.

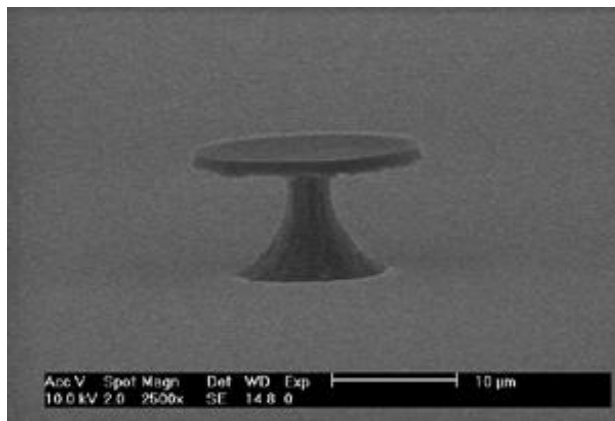
Physical vapor deposition (PVD) is another method for deposition. In PVD a material is detached from its source and deposited to the substrate of interest such as a silicon wafer. PVD is mainly used to deposit metals and metal oxides. There are two main methods for PVD: evaporation and sputtering. Evaporation requires a vacuum chamber where both the substrate and the source are placed. The source is heated enough to evaporate the material which is then condensed on the substrate. In sputtering, inside a vacuum chamber, an RF power source causes an inert gas such as argon to ionize. The ions are accelerated and impact the source material causing it to break off. The material then condenses on the substrate.

Epi-micromachining, where the epitaxial layer is used as the mechanical layer, is a variation on surface micromachining. There are a number of epi-micromachining processes. The silicon micromachining by plasma etching process (SIMPLE), forms micromachined devices in one etch step. The merged epitaxial lateral overgrowth (MELO) process is part of selective epitaxial growth (SEG). Finally, in epi-poly a polysilicon layer is grown in the epitaxial reactor. Epi-poly offers flexibility in machining of horizontal dimensions. Otherwise, the mechanical layers can be formed simultaneously as in the single crystal epi [Gennissen, 1997].

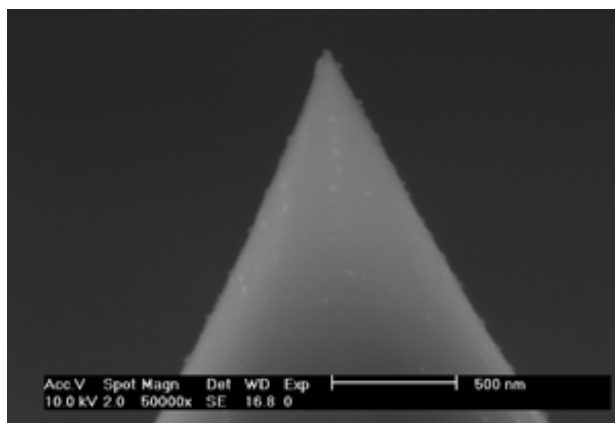
2.4 Bulk micromachining

In bulk micromachining parts of the silicon substrate are removed in order to form channels, through wafer holes, and grooves etc.. Etching is also used to remove silicon oxide and other materials. There are two main etching techniques: dry etching and wet etching.

Wet etching entails the use of an isotropic or anisotropic chemical etchant. Isotropic etchants, such as HNA (a mixture of hydrofluoric acid, nitric acid and acetic acid), etch at the same rate in all directions [Kovacs, 1998]. While, anisotropic etchants, such as potassium hydroxide (KOH), etch faster in a preferred crystal orientation of the silicon, for example perpendicular to the (110) plane, and slower perpendicular to the (100) and (111) planes. An example of anisotropic etch is the hole shown in Fig. 2.2 and the oxide cap in Fig. 2.3. Doping, such as boron doping, is sometimes used to affect the etching rate. In wet etching both the wafer along with the etchant are immersed in a bath.



(a)



(b)

Fig. 2.3. Examples of DRIE etching. The etched material is polysilicon. An oxide layer is wet etched in buffered hydrofluoric acid (BHF) creating a round protective layer seen in (a). Then DRIE is used to isotropically etch the polysilicon layer using SF_6 and O_2 gases. A partially DRIE etched pillar, with the oxide cap still on, is shown in (a). By continuing to DRIE etch ultimately the cap falls. The oxide cap is then removed and the result is a very sharp tip (b).

Dry etching can be categorized in three types: vapor phase etching, sputter etching, and reactive ion etching (RIE). In vapor phase etching a wafer is introduced in a chamber with gases that etch the material on the wafer. Typically this technology is used to etch silicon dioxide with hydrogen fluoride (HF) or silicon with xenon difluoride (XeF₂). Sputter etching ions bombard a material to remove the areas that will be etched. RIE employs an RF power source to ionize the gases that are then accelerated towards the substrate. The ions react etching the material and form another gas in a chemical reaction isotropically etching the material. When the ions have higher energies they can physically knock out parts of the material without creating another gas anisotropically etching the material. These two types of etching can be adjusted accordingly. Deep RIE (DRIE) or "Bosch process" can etch hundreds of microns deep at very fast rates. This is done by alternating two gas compositions. One gas composition forms a polymer that is dissolved fast in the horizontal direction by the second gas composition and slower on the vertical sidewalls. Examples of DRIE are shown in Fig. 2.3.

2.5 Conclusions

This chapter provided an overview of techniques used to fabricate the devices presented. First photolithography was discussed, then the materials used and the deposition techniques. Finally the etching techniques under two main methods (bulk and surface micromachining) are described. In the following chapter the basics of cantilever operation will be described.

3

Overview of micro-cantilevers

This chapter provides a short review of micro-cantilevers, their use, and operation⁵. One of the simplest devices based on microelectromechanical systems (MEMS) and nanoelectronic systems (NEMS) is the microcantilever. Initially cantilevers were used in atomic force microscopy and scanning probe microscopy (SPM) [Binnig, 1986]. These cantilevers included a sharp tip and found numerous applications such as in topographical measurements, magnetic [Martin, 1987], thermal measurements [Williams, 1986], elastography [Costa, 2003], maskless lithography [Basu, 2004], data storage and other applications [Vettiger, 2000; Lerchner, 2000; Majumdar, 1999]. Ultimately cantilevers found their way in a number of applications other than SPM as outlined below.

⁵ The review provided is not exhaustive and several details and aspects were omitted in the interest of brevity.

3.1 Introduction

Cantilever use is ubiquitous beyond the application of AFM and SPM and has been extensively applied to many fields. An exhaustive list of all of micro-cantilever applications is beyond the scope of this chapter. Indicative applications include electronic nose for remote gas detection such as explosive detection [Baller, 2000; Yinon, 2003], in serum detection of biomolecules such as glucose [Subramanian, 2002], detection of proteins such as PSA [Wu, 2001], and measuring the mass of cells [Kidong Park, 2008].

The author started working with cantilevers for scanning probe microscopy and scanning thermal microscopy in applications such as subsurface detection [Gaitas, 2006], hot spot detection, and high speed and frictional imaging [Gaitas, 2006^B]. He also used cantilevers for biological applications such as single cell elastography [King, 2010], patch clamping [King, 2011], single cell manipulation [Gaitas, 2011^{Mag}] and lysis [Gaitas, 2011^{Mag}]. The author has also developed methods for imaging using laser light [Gaitas, 2008] and using thermal vibrations [Mitra, 2009].

3.2 Detection of cantilever movement

There are several methods to detect cantilever movement. The most common are light-based techniques where a laser light is reflected on the back side of the cantilever, the light is collected, and the movement of the cantilever is tracked. Several variations of this method are presented below.

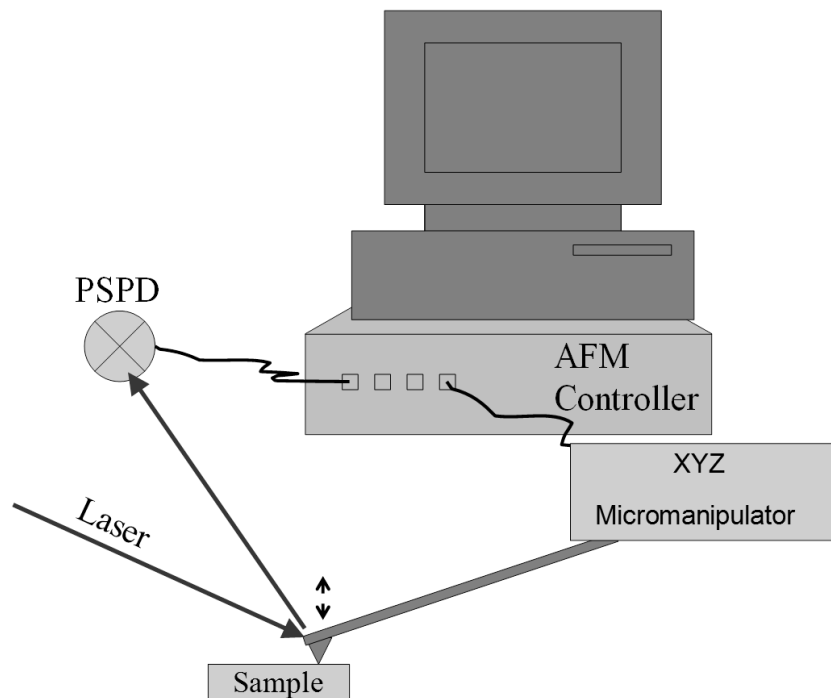


Fig. 3.1 The probe movement is controlled using the AFM's position-sensitive photodetector (PSPD). The optical deflection method is used to detect cantilever movement.

When the cantilever probes are used with an AFM, the probe is operated by scanning a cantilever tip across a sample and making measurements at discrete points. The most common deflection detection method is the optical method [Meyer, 1988], which uses a laser beam that is reflected off the back side of the cantilever probe. The reflected beam is detected by a position sensitive detector (PSD). As the cantilever moves, the reflected light falls at different spot of the PSD. These changes can be correlated to cantilever deflection. This method offers very high resolution. However, it is more expensive than other techniques, less portable, and it is problematic when measuring in liquids. There are several

other techniques that use a light beam for deflection detection. These techniques are: the interferometry method [Erlandsson, 1988], the optical diffraction grating method [Manalis, 1996], the charge coupled device method [Kim, 2003], the triangulation displacement meter deflection detection [Gaitas, 2008], and the confocal displacement meter deflection detection [Gaitas, 2008].

The piezo-resistive [Tortonese, 1993] and piezo-electric deflection detection [Minne, 1995] method entail embedding a resistive sensing element close to the surface of the cantilever and recording the stress change of the cantilever by measuring the change in resistance of the cantilever. This is typically done using a Wheatstone Bridge circuit and amplifiers. The cantilever element is one of the arms of the bridge. PZT and ZnO, are the most common piezo-electric for microcantilever applications. For the piezo-resistive sensor the sensing elements are made by selectively doping silicon [Tortonese, 1993; Chui, 1996] by depositing metal or metal oxide films on cantilevers such as gold (elastoresistive) [Li, 2007; Calleja, 2003], indium tin oxide [Wisitsoraat, 2007], nichrome [Allen, 2009], or by depositing other materials such as amorphous carbon [Peiner, 2006].

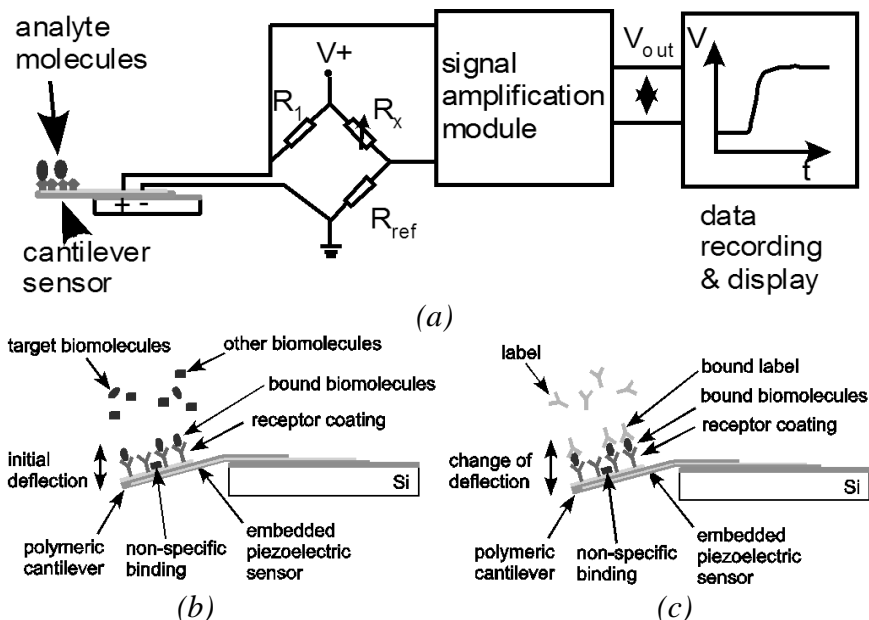


Fig. 3.2 (a) Schematic circuit diagram of a cantilever used for biomolecule detection. The binding between receptors and target molecules changes the surface stress, which results in the deflection of the cantilever, detected with the embedded elastoresistive sensor. (b) Measure the initial deflection when the target biomolecules are bound. (c) Measure the final deflection after the labels are bound to the target molecules.

3.3 Operation

A cantilever can be operated in a dynamic mode or a static mode. In a dynamic mode changes in the resonant frequency are measured. These changes reflect changes in the mass and surface stress of the cantilever [Chen, 1995]. In AFM this mode is also referred to as tapping mode. In tapping mode, the cantilever is oscillated near the resonance frequency using piezoelectric actuators, and the cantilever tip touches the surface periodically, producing a scan without scratching the surface. As the cantilever

approaches the surface, the amplitude of its oscillations changes due to the tip-sample interaction. This measurement is used to map out topographical features. Typically the probe is operated in closed loop feedback (constant amplitude) to avoid non-linear effects. In conventional dynamic mode the cantilever is oscillated via an external piezoelectric element. Alternative approaches include: cantilever with integrated piezoelectric actuation [Rogers, 2004], cantilever with integrated thermomechanical Al/SiO₂/Si bimetallic actuation and integrated piezoresistive readout [Pedrak, 2003], and cantilever with integrated thermomechanical actuation [Lee, 2007; Mitra, 2009].

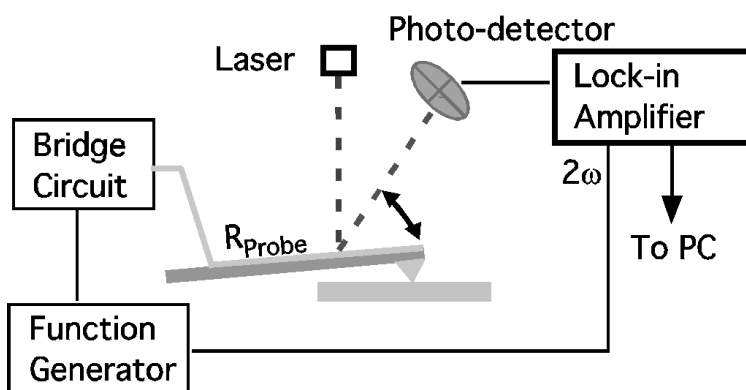


Fig. 3.3 Sinusoidal alternating current (AC) oscillations produced by a function generator drive an AC current and cause the cantilever to vibrate. The AFM laser is reflected into the photodetector by the cantilever. The deflection signal is fed into a lock-in amplifier [Mitra, 2009].

In static mode the changes in surface stress are measured by measuring the changes in deflection. In AFM this mode is also referred to as contact mode. This mode requires a simpler set-up than the dynamic mode. Static mode is preferred when piezoresistive readouts are used. It is also preferred when additional

measurements are taking place. Examples where contact is required are: scanning thermal imaging [Gaitas, 2006], frictional force measurements [Gaitas, 2006B], single cell elastography [King, 2010], and patch clamping [King, 2011]

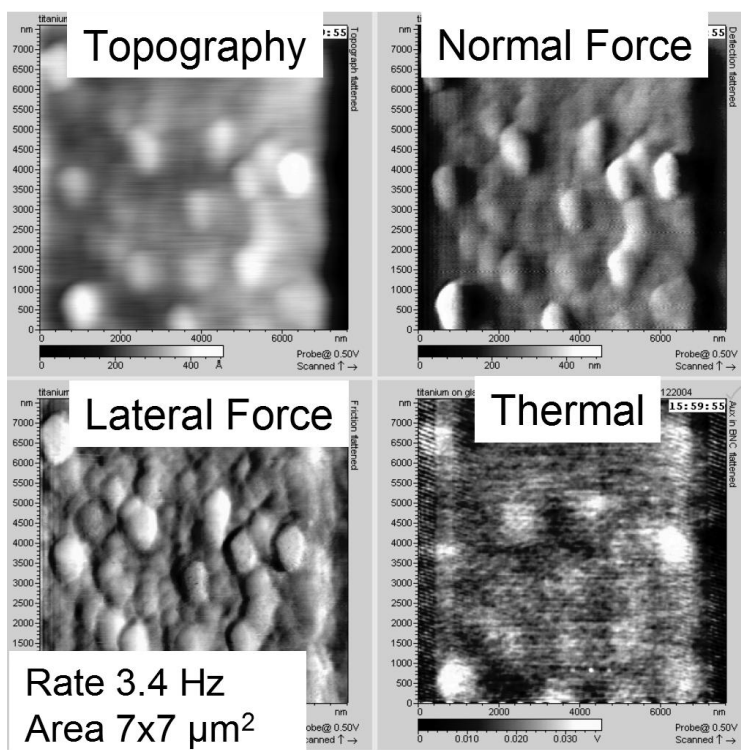


Fig. 3.4 This figure illustrates topography, lateral force, normal force, and thermal images obtained simultaneously in contact mode (static mode) [Gaitas, 2006B]. Thermal imaging was obtained using a Wheatstone bridge circuit. The sample was a 20 nm thick film Ti patterned on Pyrex glass. Thermal features smaller than 200 nm can be observed. The scans were obtained with a PicoMaps system from Agilent.

3. 4 Conclusions

This chapter provided a short review of micro-cantilevers, their use, and operation. A variety of methods for detection of cantilever movement were discussed and the two main techniques of cantilever operation were explained. There are several methods to detect the cantilever movement, namely: light-based techniques where a laser light is reflected on the back side of the cantilever, the piezo-resistive and piezo-electric deflection detection methods that entail embedding a sensing element close to the surface of the cantilever and recording the stress change of the cantilever by measuring the change in resistance of the cantilever. Cantilever use is ubiquitous beyond the application of atomic force microscopy and scanning probe microscopy and has been extensively applied to many fields.

4

Design and fabrication of devices

In order to study the properties of various thin metal films on cantilevers a number of devices were fabricated following different fabrication processes. In this chapter the design and fabrication of these devices is described in detail. First, thermal modeling and mechanical modeling are presented to give us an insight into how the devices behave. This is followed by a detailed description of the design, fabrication, and figures of silicon, silicon nitride, and polymer cantilevers.

4.1 Thermal modeling

Simulations were conducted in order to determine the optimal designs for the thermal element. Preferably the thermal element is narrower and located at the tip area and wider elsewhere in order to maximize the thermal sensitivity at the point of measurement by increasing the electrical resistance at the tip area.

In this Joule heating simulation a very simple finite element analysis (FEM) model was implemented in COMSOL Multiphysics. The model assumes an Au layer that is thermally insulated on all the surfaces except for the two anchors. The cantilever is 200 μm long and 60 μm wide. Fig. 4.1 (a) shows the current density and Fig. 4.1 (b) the temperature distribution.

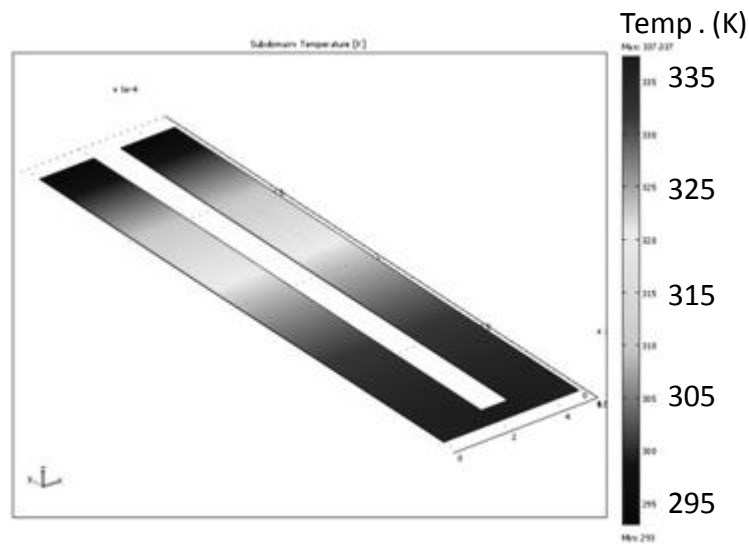
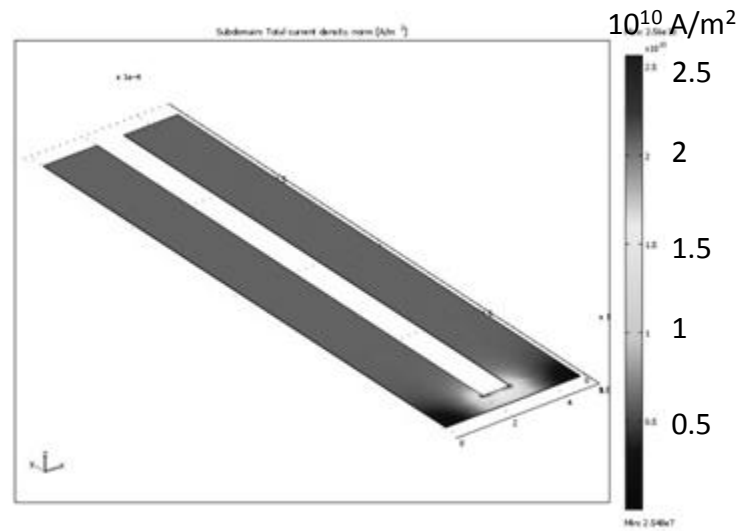


Fig. 4.1 In this simple model it is assumed the metal layer is thermally insulated except for the two anchors. The current density is shown in (a) and the temperature distribution in (b).

In addition, more elaborate models that consisted of a silicon chip and cantilever with a thin layer of metal on top were developed. Fig. 4.2 below show the different models. The models differ based on their top metal layer. One of the models (Fig. 4.2 (a)) has a single metal element of tungsten. Another model has two metal elements one made of tungsten and gold or both made of gold (Fig. 4.2 (b)), the inner metal element is not heated. The gold layers have thicknesses of 10 nm and the tungsten has a thickness of 100 nm.

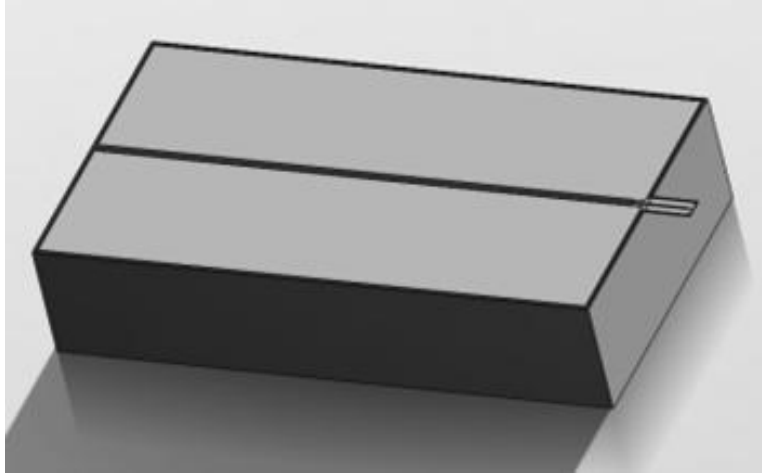
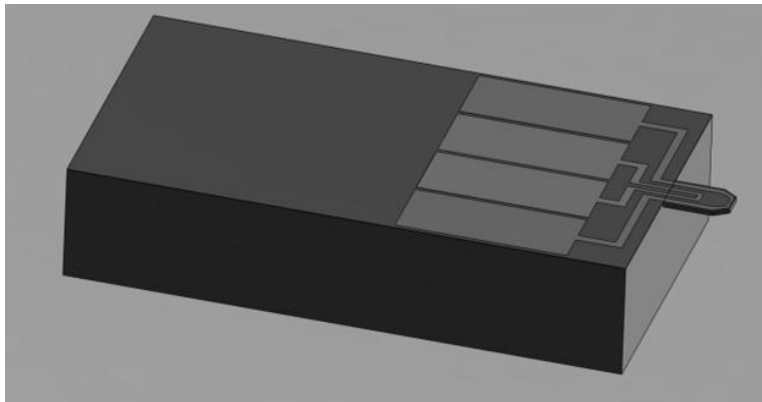
*(a)**(b)*

Fig. 4.2 (a) One metal element and (b) two metal element designs where the outer element is the heating element.

The initial model temperature and ambient temperatures for the model were both 293 K. The models in COMSOL have heat flux

boundary conditions with a heat transfer coefficient of $10 \text{ W}/(\text{m}^2 \text{ K})$. Radiation was used with an efficiency of 1. The relations between input power and temperature was studied. The heat transfer boundary conditions had a heat transfer coefficient of 5 and a T_{inf} of 293K. The back of the Si block was at a constant temperature of 293K. The resistivity of gold was $2.44 \cdot 10^{-8} \Omega\text{m}$ and the TCR was 0.0034 K^{-1} . The Si/SiO sections had a resistivity of $6.2 \cdot 10^{10} \Omega\text{m}$. The two gold elements have thickness of 10 nm. The results of the simulation showed that there was negligible stress or strain due to the applied current and resistance heating.

The temperature distributions of the various structures are simulated. All models have similar distributions. The simulations shown in Fig. 4.3 demonstrate that using the these designs the highest temperature is observed at the tip of the cantilever.

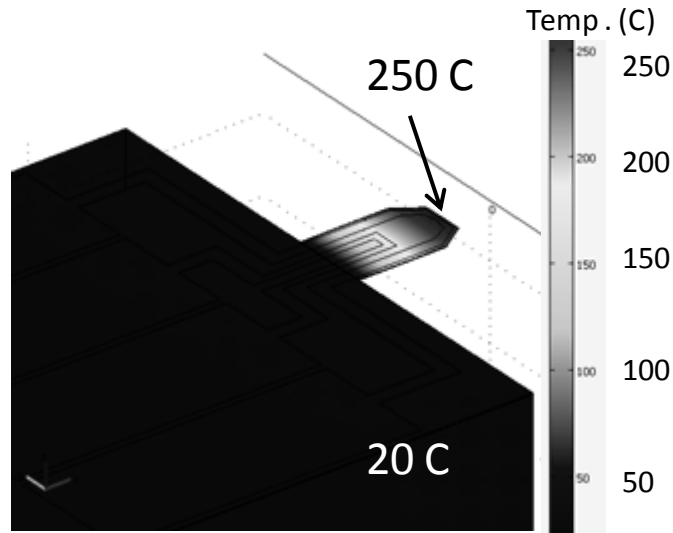


Fig. 4.3 Temperature distribution for a silicon cantilever with a 10 nm thin heating element made of Au.

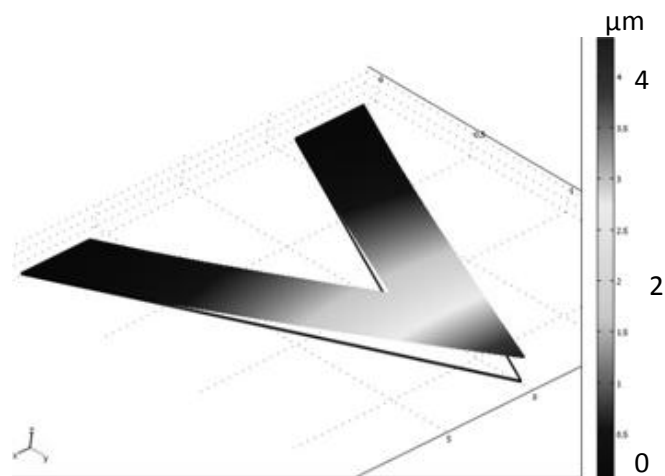
4.3 Mechanical and piezoresistive modeling

Simulations were conducted in order to determine the optimal designs for the displacement sensing element. The results presented here and the conclusions that are drawn from these simulations assist in understanding the location of the stress and strain on the cantilever in order to improve the design of the sensing element and the cantilever. For these simulations a finite element analysis (FEM) model was used in COMSOL. Various models were run for all the designs, however, polyimide devices are comprehensively presented. The conclusions relating to the location of stress and strain from these simulations are transferable to the silicon piezoresistive (elastoresistive) devices due to design similarities.

The effective spring constant was calculated for various cantilever designs. Here a selected number of these designs and materials are presented. The spring constant for a $\text{SiO}_2/\text{Si}_3\text{N}_4/\text{SiO}_2$ (ONO) cantilever $200\ \mu\text{m} \times 60\ \mu\text{m}$ beam with thickness $400\ \text{nm}/200\ \text{nm}/400\ \text{nm}$ was approximately $0.135\ \text{N/m}$. Similar simulations for a V-shaped beam with length $173\ \mu\text{m}$ and width of each leg $40\ \mu\text{m}$ and the same thickness produced a spring constant $0.228\ \text{N/m}$. These are shown in Fig. 4.4.



(a)



(b)

Fig. 4.4 The simulations for a $\text{SiO}_2/\text{Si}_3\text{N}_4/\text{SiO}_2$ cantilever of a (a) rectangular and a (b) V-shaped beam.

A number of polyimide cantilever designs were studied consisting of a silicon block with a thin layer of polyimide on top. Two most relevant designs are shown in Fig. 4.5.

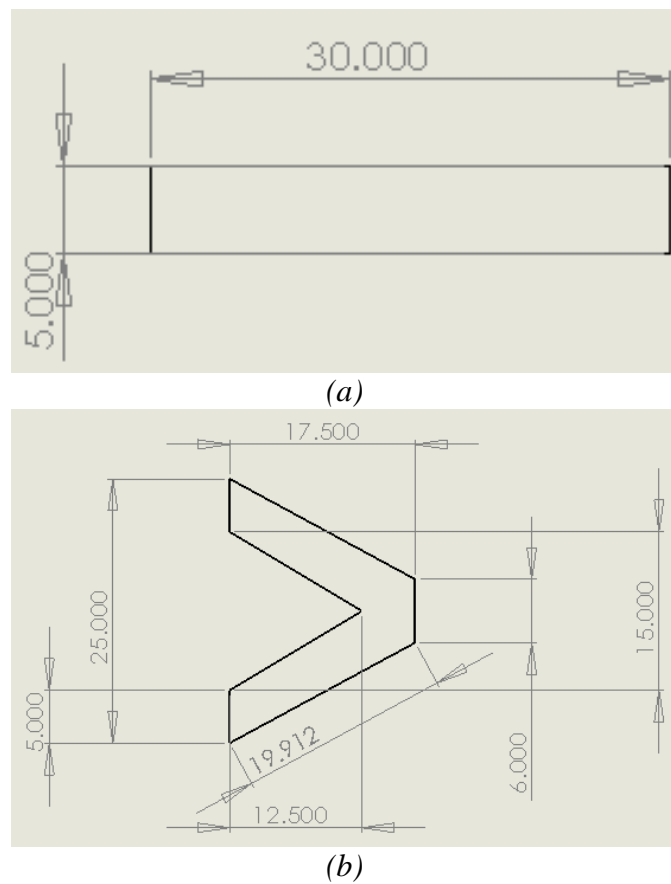


Fig. 4.5 The simulations were conducted for various thicknesses of polyimide, here $1.45 \mu\text{m}$ is shown. (a) The rectangular design shows a cantilever with dimensions $5 \mu\text{m} \times 30 \mu\text{m}$. (b) The V-shaped cantilever has a length of $17.5 \mu\text{m}$ and a width of $25 \mu\text{m}$ with each leg having a $5 \mu\text{m}$ width.

Table 4.1 Summary of spring constant, k , FEM results for a selected number of cantilever designs.

Device	$k_{\text{Theoretical}}$ (N/m)	k_{FEM} (N/m)
Rectangular 1.45 μm thick polyimide cantilever	1.20	1.22
V-shaped 1.45 μm thick polyimide cantilever	-	9.92

The spring constant, k , results were calculated by applying a load at the tip of the beam. The load was varied while the tip displacement at the edge was calculated. The effective spring constant was found by dividing the force applied by the displacement at the tip of the beam. Each design was averaged over several different load values to find an average spring constant.

In order to evaluate the various designs, the change in resistance of the film with stress or strain, as well as the areas of strain and stress on the cantilever need to be determined. These calculations were accomplished by splitting the beam into smaller sections and assuming constant stress or strain in each those section. The strain of the gold sensing element is assumed to be the same as the strain on the top edge of the cantilever. A strain or stress of the gold resistor changes its resistance. Strain is dependent on tip displacement, in these simulations the tip displacement was varied and the sensitivity of the gold resistor was estimated.

The equation below is used to find the resistance sensitivity

$$\frac{\Delta R}{R} = G \cdot e + \alpha \cdot (\Delta T) \quad 4.1$$

G is the gauge factor, e is the strain, and α is the change in resistance due to temperature change. ΔT is the temperature change. It is assumed that the temperature change is 0.

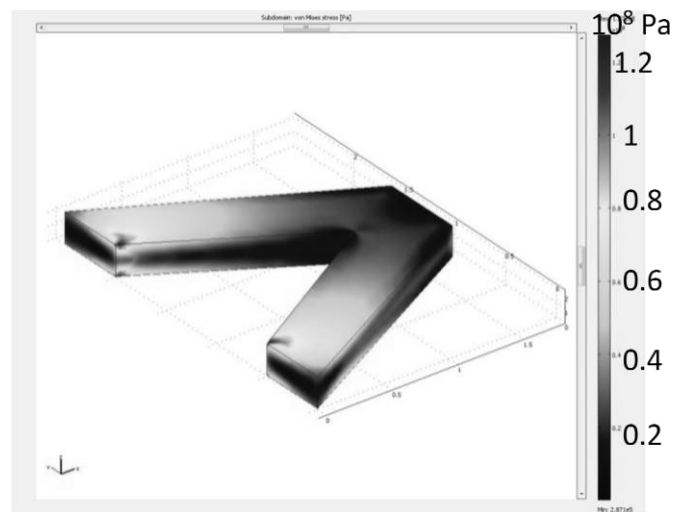
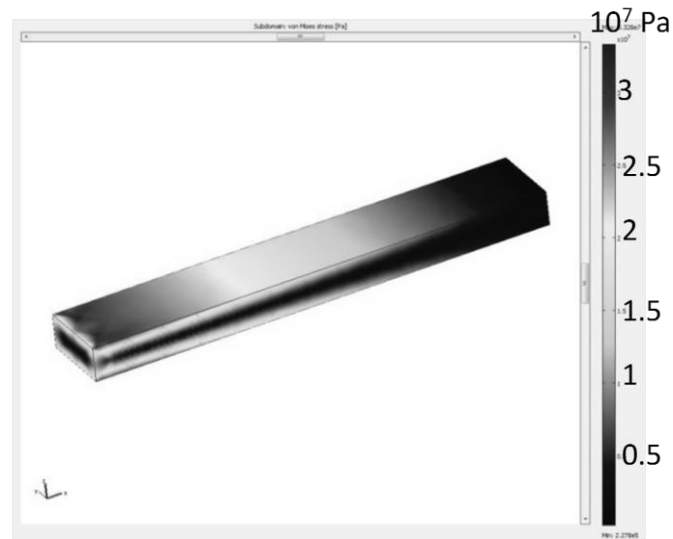


Fig. 4.6 FEM simulation of (a) the rectangular cantilever; (b) and the V-shaped cantilever.

The FEM data was exported to MatLab. Using data fitting functions, stress was related to various locations on the beam. Only the areas where the sensing element is deposited are relevant to the calculations. From Fig. 4.6 and the simulation results it is determined that the sensing element should be placed near the base of the cantilever since this is where most of the stress is.

Knowing the stress and strain, the resistance change ΔR can be calculated. From these values the sensitivity, $(\Delta R/R)/\Delta z$, can be estimated. The table below summarizes the results for a 1 μm tip displacement Δz in the different models with a gauge of 3.08. Table 4.2 summarized the sensitivity results for various designs.

Table 4.2 Sensitivity analysis of different cantilevers and thicknesses.

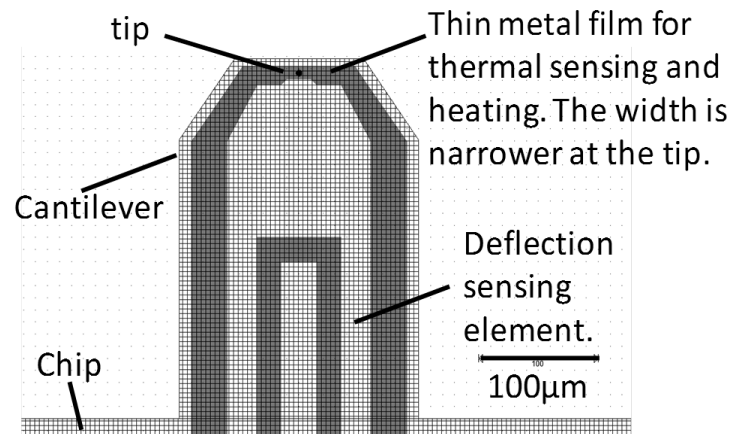
Structure	Resistance Sensitivity
Rectangular design with 1.45 μm thickness	0.00398
V-shaped design with 1.45 μm thickness	0.0642

4.4 Silicon cantilever devices

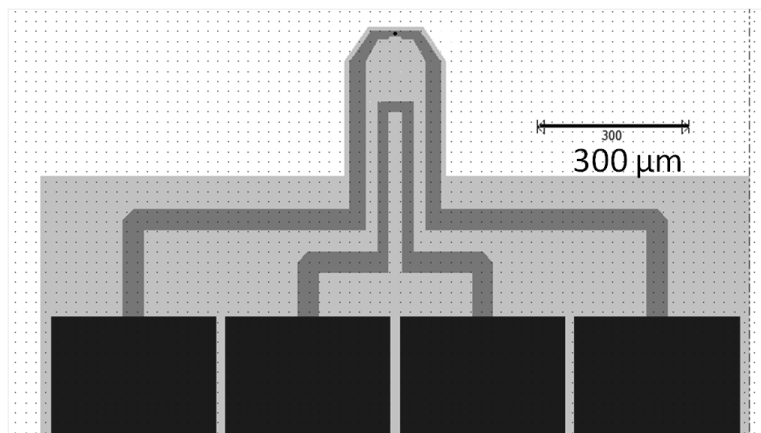
4.4.1 Designs

The design of the silicon/silicon oxide cantilever with two metal sensing elements is shown in Fig. 4.7 (a) and (b). The cantilever is 300 μm long and 200 μm wide. It includes a piezoresistive element that is 20 μm wide. It also includes a thermal element with width of 30 μm , which narrows to 10 μm near the tip. The entire design is shown in Fig. 4.7 (b) including the pads where wirebonds are placed. A cantilever that is part of a probe array is shown in Fig. 4.7 (c). The cantilever length is 215 μm and the width is 110 μm . The width of piezoresistive element is 10 μm , and the width of

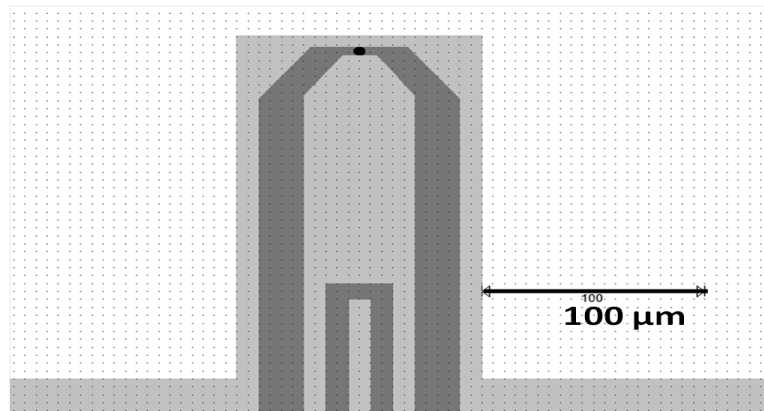
thermal element is $20\ \mu\text{m}$, and it narrows down to $5\ \mu\text{m}$ over the tip. The design of a cantilever array with seven cantilevers is shown in Fig. 4.7 (d).



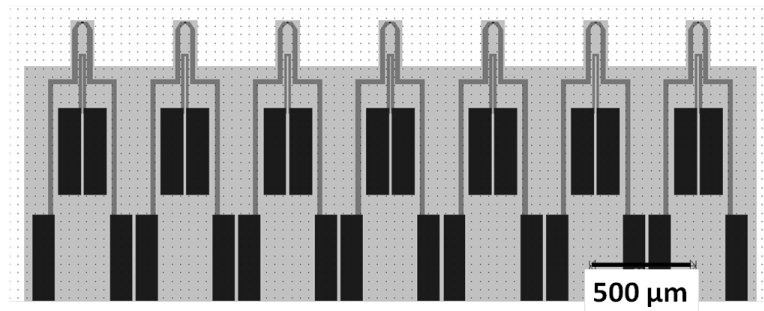
(a)



(b)



(c)



(d)

Fig. 4.7 (a) The design of the silicon/silicon oxide cantilever with two metal sensing elements. (b) The entire design includes the pads where wirebonds are placed. (c) A cantilever that is part of a probe array. (d) The design of a cantilever array with seven cantilevers.

4.4.2 Fabrication

The device is fabricated in a four-mask process described in Fig. 4.8. The process starts with a silicon oxide insulator (SOI) wafer.

A thermal oxide masking layer is grown and patterned for the probe tip on a silicon-on-insulator (SOI) wafer. The tip is formed using potassium hydroxide (KOH, 30% wt.) anisotropic etching (Fig. 4.8(1)), the oxide mask is then removed, and the tip is sharpened with several oxide sharpening steps [Akamine, 1990]. The oxide sharpening step involves at least three runs of thermal oxidation followed by hydrogen fluoride (HF) etching. A 100 nm-thick silicon oxide is thermally grown on the wafer to provide electrical insulation (Fig. 4.8(2)). The cantilever is patterned on the front side of the wafer with the Bosch deep reactive-ion etching (DRIE) process (Fig. 4.8(3)). Metal lines are evaporated and patterned on top of the cantilever structure with lift-off process to form the sensing elements (Fig. 4.8(4)). The thickness of the metal layers is measured during the evaporation and the variation was within $\pm 10\%$. The front-side is protected by spin coating a 30 μm thick photoresist. The suspended cantilever is then formed by back side DRIE with an etch rate of 3 $\mu\text{m}/\text{min}$ (Fig. 4.8(5)). The 1 μm buried oxide layer of the SOI wafer acts as an etch stop to prevent the back side DRIE from attacking the Si cantilever structures. Finally, the probes are released by removing the buried oxide layer using buffered hydrofluoric acid (HF) etchant. If the probe is used with an AFM, then a thin layer of aluminum is evaporated on the back-side to improve the laser reflection (Fig. 4.8(6)). The metal film is too thin, so the stress is dominated by the thermal oxide insulation layer and has compressive stress on the front side. Most metals used for reflection on the backside have tensile stress. In order to balance the stress and produce relatively flat cantilevers 110 nm of TiW is sputtered on the back side with a pressure of 3.5 mTorr.

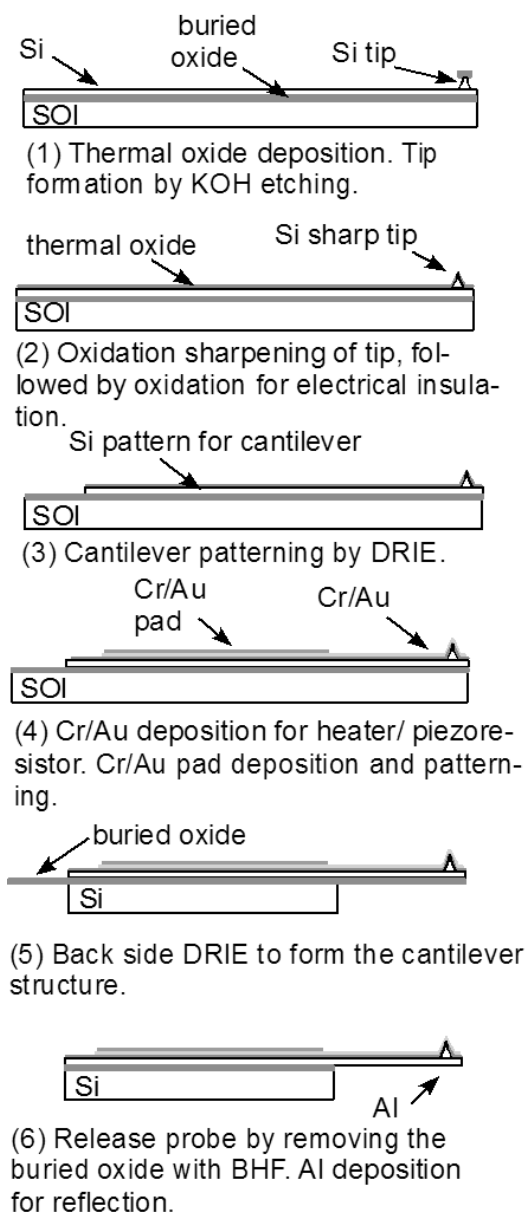


Fig. 4.8 Process flow for fabricating the silicon cantilevers.

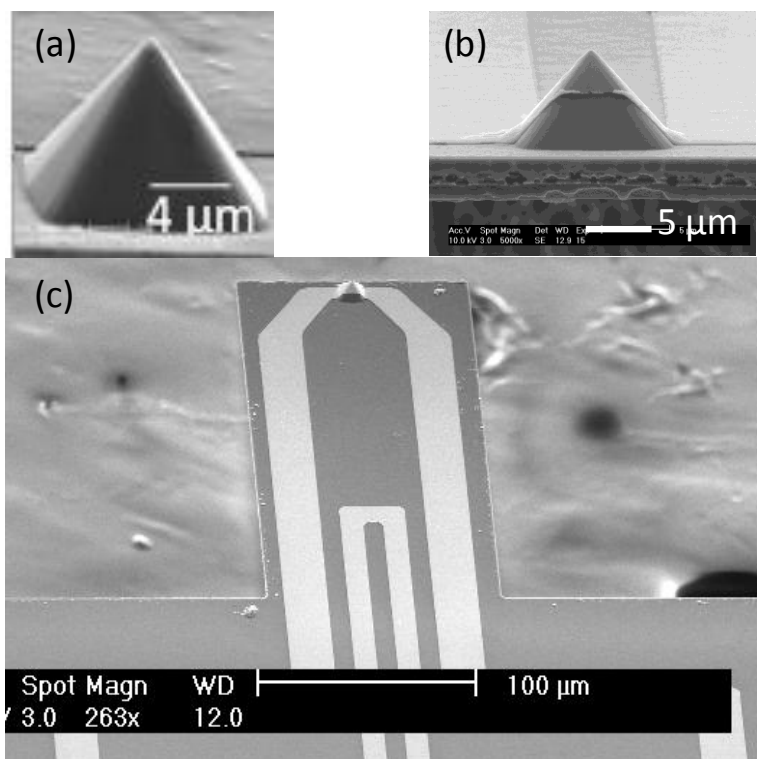


Fig. 4.9 SEM picture of fabricated piezo-thermal probe. (a) Probe tip prior to metal deposition ($<1 \mu\text{m}$). (b) Probe tip post metal deposition. This is not as sharp. However, when scanning the contact area is $<20 \text{ nm}$. (c) SEM image of a probe. The shorter element near the base is the deflection sensing element. The longer metal element that goes over the tip is a thermal element used for heating and measuring temperature related parameters.

Fig. 4.9 shows the probe design that includes two sensing elements on one cantilever, each of which consists of a 5 nm or 10 nm thin gold film. The resistor covering the tip area forms a microbolometer/microheater and the resistor near the base of the cantilever forms a deflection sensing element. The rectangular

cantilever is 200 μm wide and 300 μm long. It is a stacked structure of silicon and silicon oxide layers with a total thickness of 2 μm . A 3 x 1.4 x 0.5 mm³ chip serves as the base of the cantilever.

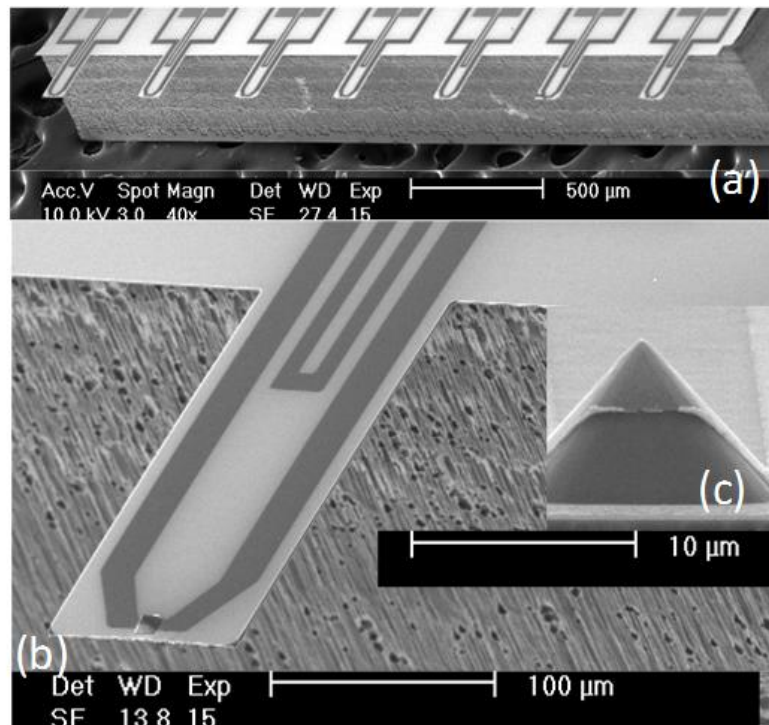


Fig. 4.10 (a) SEM of the probe array. (b) Individual cantilevers include two resistors, one over the tip serving as a localized heater/thermal sensor and a second closer to the base serving as a resistor for deflection sensing. Inset (c) SEM close-up of the tip.

Figure 4.10 shows the resulting micro-cantilever array. The design includes two sensing elements on one cantilever, each of which consists of a gold film deposited on a silicon oxide/silicon cantilever. The resistor covering the tip area forms a micro-

bolometer (heating element) and a resistor near the base of the cantilever forms a deflection sensing element. The rectangular cantilever is 100 μm wide, 200 μm long, and 2 μm thick. The resulting tip has a <100 nm diameter and a 7.5 μm height. The sensing elements are made of 5 nm or 10 nm thick gold.

4.5 $\text{SiO}_2/\text{Si}_3\text{N}_4/\text{SiO}_2$ cantilever

4.5.1 Designs

$\text{SiO}_2/\text{Si}_3\text{N}_4/\text{SiO}_2$ cantilever devices were fabricated to study thin films at the metal-insulator regime.

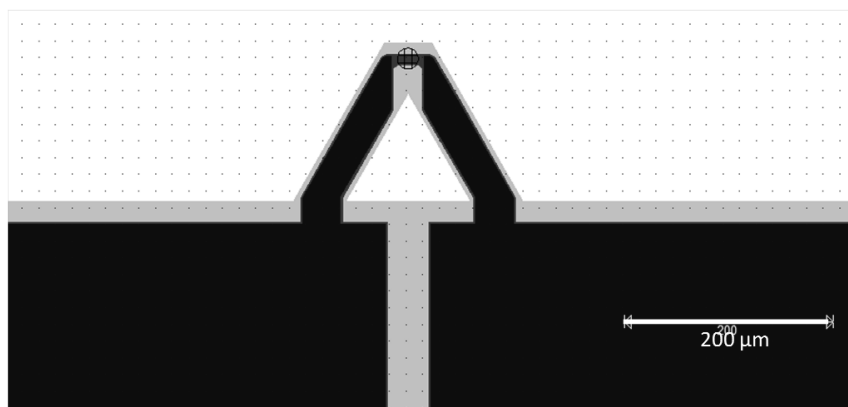


Fig. 4.11 Design of the thermal probe on a $\text{SiO}_2/\text{Si}_3\text{N}_4/\text{SiO}_2$ cantilever.

The length of the triangular shaped cantilever is 150 μm and each leg is 50 μm wide. There are two metal layers, one on top of the other to increase the thickness of the metal. The first metal layer is the sensing metal going over the tip. The second does not cover the tip. The sensing metal narrow near the tip and has a width of 10 μm . While both metals widen to 40 μm at base. The base of the tip is 20 μm .

4.5.2 Fabrication

In this process, an ultrathin film (<20 nm) titanium microbolometer was developed, which is integrated onto a $\text{SiO}_2/\text{Si}_3\text{N}_4/\text{SiO}_2$ (ONO) cantilever with a Si/SiO_2 tip. The fabrication process included: tip formation by isotropic dry etching (DRIE) with an oxide layer as etch mask; tip sharpening by growing 1 μm thermal oxide followed by a BHF oxide removal step; 1.1 μm thick LPCVD ONO layer deposition on the Si substrate; cantilever patterning by a sequence of ONO etching steps; tip area $\text{SiO}_2/\text{Si}_3\text{N}_4$ layer removal; metals patterning with a series of lift-off processes; wafer backside etching for device release; and 20 nm of aluminum backside deposition.

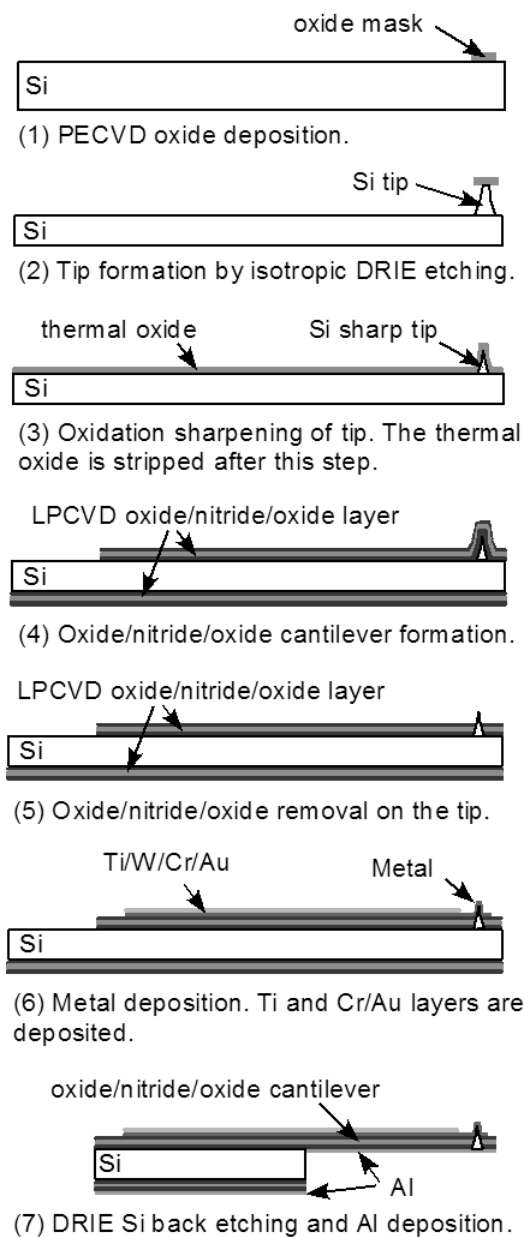


Fig. 4.12 Fabrication process for the O/N/O cantilever.

The design was triangular with 220 μm wide base and 160 μm long. The cantilevers were made from a 1.1 μm thick ONO layer with 10 μm long Si/SiO₂ tips. A metal film was deposited covering the tip area to form the microbolometer, while a gold layer was deposited on the top of the metal film, excluding the tip area for electrical contact. 3 mm x 1.4 mm x 0.5 mm chips held the cantilevers.

In addition to the cantilever, different wafers were prepared with titanium and tungsten resistors, these devices are described in greater detail in Chapter 11. As shown in Fig. 4.6 (b), a 10 μm wide titanium film was deposited on the substrate to form a resistor. The lengths of the titanium resistors vary from 14 μm to 32 μm . 150 nm thick gold film was deposited on top of the titanium or tungsten traces excluding the tip area creating leads and leaving exposed a narrow rectangular thin film at the tip area. The films were expected to form a native oxide soon after the films were exposed to the ambient environment. However, the bolometers were found not to be vulnerable to film degradation as a result of additional oxidation. The resistors have also been analyzed over a two month period and the drift in base line resistance has been consistently less than 2%.

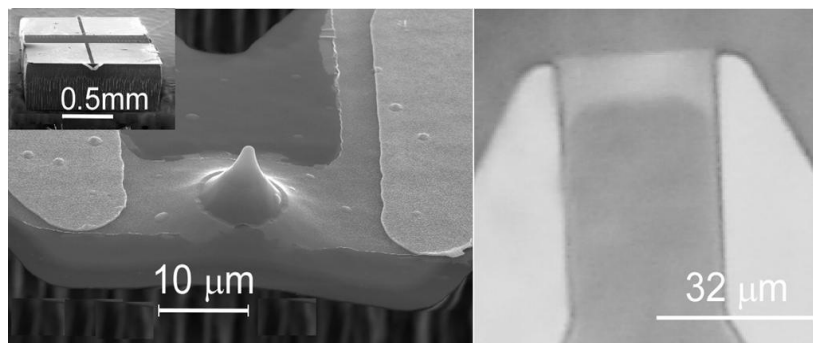


Fig. 4.13 a) SEM of microbolometer probe. Inset: SEM of the chip.
b) Picture of titanium resistors on a wafer.

4.6 Polyimide cantilevers

4.6.1 Designs

Polyimide probes are attractive due to their mechanical properties. These cantilevers are also less brittle than their silicon or silicon nitride counterparts. A simple fabrication process is used to produce cantilevers for chemical sensing. The base is 26 μm, each arm is 6 μm wide, the length is 18 μm, while the sensing element is 2 μm wide (Fig. 4.14).

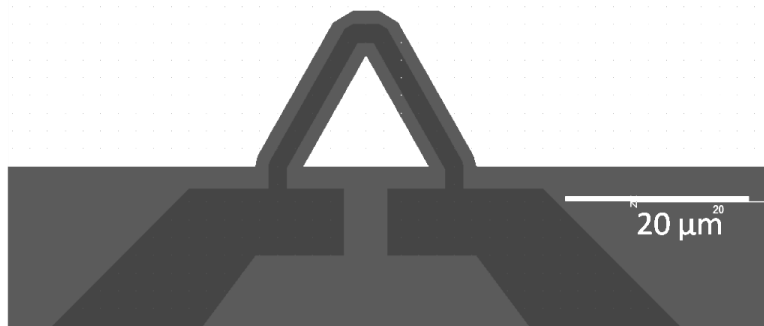


Fig. 4.14 The V-shaped polyimide cantilever.

4.6.2 Fabrication

The major fabrication steps for these cantilevers are outlined in Fig. 4.15, include: (a) A 1 μm thermal oxide layer grown on the Si substrate. (b) A polyimide thin film spin-coated and cured on the wafer. The thickness of the cantilever is about 2.2 μm . The polyimide is then patterned using reactive ion etching (RIE) process. (c) An Au thin film with 10 nm thickness evaporated and patterned on the polyimide to form the sensing element. (d) The Si wafer etched from the back side with deep reactive ion etching (DRIE) process to form the cantilever structure. (e) The thermal oxide layer is removed by BHF solution, and the cantilever is released. (f) The cantilever can be removed out from the wafer individually. A small droplet of the receptor, in this case a TTF-calix[4]pyrrole solution, is dropped onto the top surface of the cantilever, and the TTF-calix[4]pyrrole dries out on the cantilever after 1-2 min.

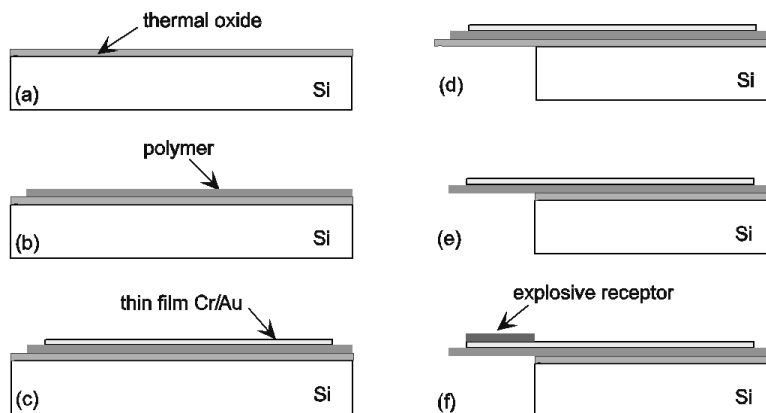


Fig. 4.15 Fabrication process of the polymeric nano-cantilever coated with explosive receptor.

The polyimide thin film has excellent adhesion, and thus survived the entire fabrication process. The resistance of the sensor is not changed before and after chemical coating. The fabrication was successfully completed and the SEM picture of the design is shown in Fig. 4.17. The yield of this process is close to 100%.

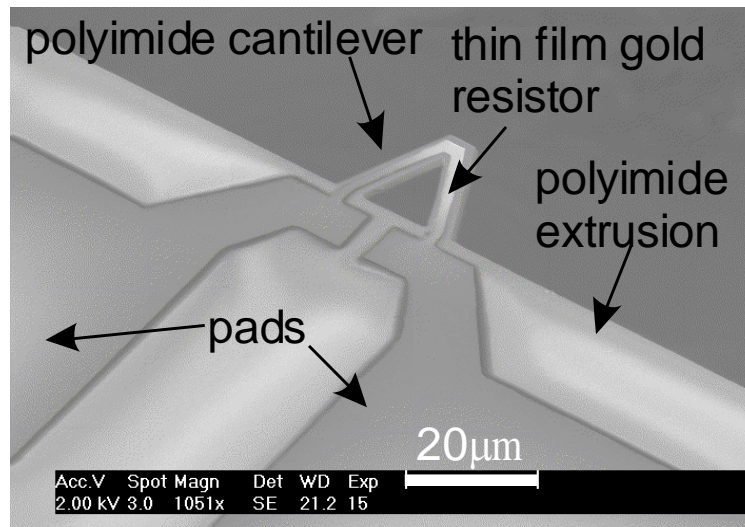


Fig. 4.16 Scanning electron microscopy image of the polyimide cantilever.

4.7 Conclusions

A number of devices were fabricated following different fabrication processes. The design and fabrication of these devices was described in detail. FEM modeling assisted in studying the thermal and mechanical properties of these devices in order to achieve optimal designs. A detailed description of the design and fabrication was presented. In the following chapters these devices will be characterized and used in various applications.

5

Temperature sensitivity of thermal probes⁶

Measuring the temperature profile of a sample using scanning thermal microscopy is challenging due to the large effect of the thermal contact resistance at the probe-sample interface, the influence of probe tip's geometry including its radius of curvature, and the probe's non-uniform heating. In order to address these challenges a calibration sample consisting of a 1 μm -wide gold wire, which can be heated electrically by a small bias current, has been developed. The Joule heating in the calibration sample wire is characterized using noise thermometry. The thermal probe is scanned in contact over the gold wire measuring temperature changes as small as 0.4 K, corresponding to 17 ppm changes in probe resistance. The non-uniformity of the probe's temperature profile during a typical scan necessitated the introduction of a temperature conversion factor, η . η is defined as the ratio of the average temperature change of the probe with respect to the temperature change of the substrate. The conversion factor was estimated at 0.035 ± 0.007 . Finite element analysis simulations indicate a strong correlation between thermal probe sensitivity and

⁶ Parts of this chapter have been published in: A. Gaitas, S. Wolgast, E. Covington, C. Kurdak, "Hot spot detection and Johnson noise thermometry calibration of a bolometer type scanning thermal probe", *Journal of Applied Physics* (2013).

probe tip curvature, suggesting that the sensitivity of the thermal probe can be improved by increasing the probe tip curvature, though at the expense of the spatial resolution provided by sharper tips. Simulations also indicated that a bow-tie metallization design could yield an additional 5- to 7-fold increase in sensitivity.

5.1 Introduction⁷

Thermal measurements at the nanometer scale are of both scientific and industrial interest, and over the past three decades, scanning thermal microscopy has been used in a variety of applications [Li, 2003; Li, 2001; Ocola, 1996; Hammiche, 1996; Luo, 1996; Lai, 1995; Hammiche, 1999; Vettiger, 2000; Lerchner, 2000; Majumdar, 1999]. Temperature calibration is required for scanning thermal microscopy, where substrate temperature changes must be measured with high accuracy. A number of ways to calibrate a scanning thermal probe have been developed [Nelson, 2007; Fischer, 2008] and include: isothermal (hotplate) calibration [Chui, 1998], melting point standard calibration (which contaminates the probe with debris from the melted material) [Lee, 2004; Fryer, 2000], use of the linearity of heater resistance with temperature [Lee, 2005], calibration methodologies using Raman thermometry [Nelson, 2007], and the use of a small thermocouple in contact with the probe [Gaitas, 2011^B].

In this chapter, a pre-calibrated 1- μm wide gold wire sample on a silicon-oxide substrate is used as a Joule heater to directly calibrate a scanning thermal probe. This calibration wire is a Johnson noise thermometer, i.e. a primary thermometer; therefore, the wire does not require calibration by another external device.

A specially-developed micro-machined scanning thermal probe (described in chapter 4) that includes two embedded sensors—one

⁷ Chapter 5 is based on joint effort between the author and Prof. Kurdak of the University of Michigan-Ann Arbor.

for measuring deflection and another for measuring localized heating—was used. The temperature sensor is a narrow thin-film gold resistor that covers the tip. In a typical application the temperature profile of the sample is obtained by monitoring the sensor resistance during a probe scan.

In order to calibrate the scanning thermal probe the aforementioned pre-calibrated 1- μm wide gold wire sample was used. The calibration wire is heated by passing current through it. At each temperature, the probe is scanned over the wire. The change in resistance of the probe with temperature is used as a calibration of the thermal probe, which is quantified by introducing a temperature conversion factor, η . This technique offers several advantages. For example, the scanning thermal probe can be calibrated directly from temperature changes on the sample, thereby obtaining a direct correlation of resistance changes of the probe with temperature changes of the sample. The probe and the calibration wire do not get contaminated, and thus they can be re-used. The calibration wire has a very long shelf-life because it is made of gold, which does not oxidize.

Previous calibration techniques measure the temperature changes of the probe. However, when measuring temperature changes of a sample, the probe temperature change is only a small fraction of the actual sample temperature change due to the thermal contact resistance between the probe and the sample, the probe's curvature, as well as the small contact area between them. The thermal contact resistance cannot be accounted using previously reported calibration techniques. Furthermore, many of these techniques, for example calibration based on melting points, rely on heating the probe and measuring its change in resistance with temperature. These techniques are suitable when the thermal probe is used as a heater. However, the thermal losses from a hot probe to a substrate are different from the thermal loss of a hot substrate to a probe, which is the case when the thermal probe is used as a thermometer.

Therefore it is difficult to estimate the real temperature of a hot sample using previously reported calibration techniques that operate the probe as a heater. The technique proposed here allows the user to estimate the temperature change of the thermal probe on a hot sample, accounting for the thermal contact resistance at the probe-sample interface, so that the user can use this calibration data for hot-spot detection scans.

In addition, due to probe-to-probe variations resulting from micro-fabrication, the thermal probes are not identical. It is therefore good practice to calibrate each probe separately. Thus, a simple calibration process like the one presented in this work is very useful. The challenges associated with the non-uniformity of probes result from tip curvature variations and film thickness variations that cannot be avoided in batch micromachining.

Finite element analysis (FEA) simulations indicate a strong correlation between thermal probe sensitivity and probe tip curvature. The simulations and experimental results suggest that thermal sensitivity of the probes can be improved by increasing the probe tip curvature, by using materials other than gold as sensing elements, and by changing the geometry of the sensing element over the tip. Specifically, a bow-tie metallization design that increases the sensitivity 5- to 7-fold in the simulations was investigated.

5.2 Scanning thermal probe

For this study, a scanning thermal probe with a metal sensing element on a Si/SiO₂ cantilever was used. The scanning thermal probe is micro-machined in a four-mask fabrication process (chapter 4). The design of the cantilever with two metal sensing elements is shown in Fig. 5.1 (a). The cantilever is 300 μm long and 200- μm wide. It is a stacked structure of Si and SiO₂ layers with a total thickness of 2 μm . It includes an elastoresistive

element that is 20 μm wide and a thermal element that is 30 μm wide, which narrows to 10 μm over the tip. The two sensing elements consist of a 10 nm gold film located on a the cantilever. The resistor covering the tip area forms a microbolometer/microheater, and the resistor near the base of the cantilever forms a deflection-sensing element. The tip, shown in an SEM picture in Fig. 5.1 (b), is 6-7 μm high and has a radius of curvature that ranges between 50-nm and 500-nm. By using a thin and narrow metal as a sensing element, the current is forced through a narrow area on the surface of tip, increasing its sensitivity to temperature changes localized at the tip. A $3 \times 1.4 \times 0.5 \text{ mm}^3$ chip serves as the base of the cantilever.

The temperature coefficient of resistance (TCR) of the scanning thermal probe is given by

$$\alpha_p = \frac{R_p(T) - R_p(T_0)}{R_p(T_0)(T - T_0)} \quad (5.1)$$

where α_p is the TCR of the probe at temperature T_0 , and $R_p(T)$ is the resistance of the probe at temperature T . The TCR of these probes is approximately 0.001 K^{-1} . The TCR was measured by enclosing the probe and a calibrated thermistor in an aluminum chamber that rested on a hot plate (shown in *Fig. 11.1*), allowing the probe temperature to be varied uniformly while the resistance of the probe and temperature were recorded simultaneously. Because the sensing element is made of gold, the TCR of the probe is not very high; however, gold is advantageous because it does not oxidize, and therefore has a long shelf life.

The TCR calibration alone is not sufficient to estimate the real temperature change of the sample in SPM applications, since the temperature of the probe is highly non-uniform. Each probe must be calibrated individually, since the curvature of the tip can influence the heat exchange with the sample. Therefore, there is a

need for a calibration sample to simplify individual probe calibration.

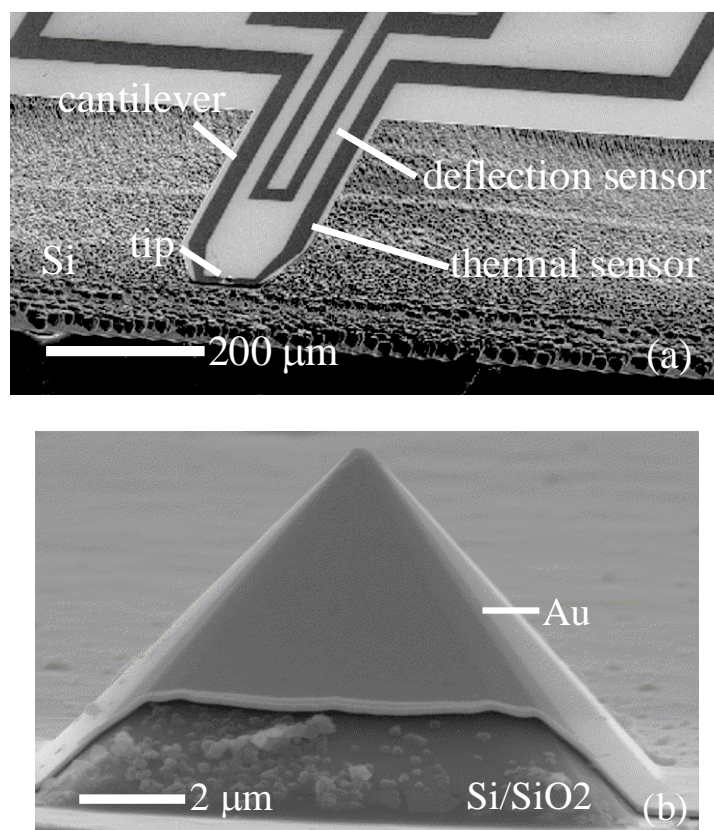


Fig. 5.1 (a) SEM image of the thermal scanning probe. (b) SEM image of the active region of the tip. The Au layer does not cover the entire tip, but is mostly concentrated in the active area. The tip has a radius of curvature between 50-nm and 500-nm.

5.3 Gold wire calibration

5.3.1 Device & fabrication

A four-terminal linear gold resistor is used as a calibration device to distinguish the thermal noise generated in the lead wires from that generated in the resistor. Scanning electron microscopy (SEM) images of the wires are shown in Fig. 5.2. The device rests on 300 nm SiO₂, and a 500 μm -thick Si wafer. The sample pattern includes two parallel wires that are 400 μm long, 1 μm wide and 15 nm thick. There is a 1 μm gap between the two wires. Each wire is connected to four leads and contact pads: one on each end of the wire, and one positioned 50 μm from each end. The wire had a resistance of 993 Ω .

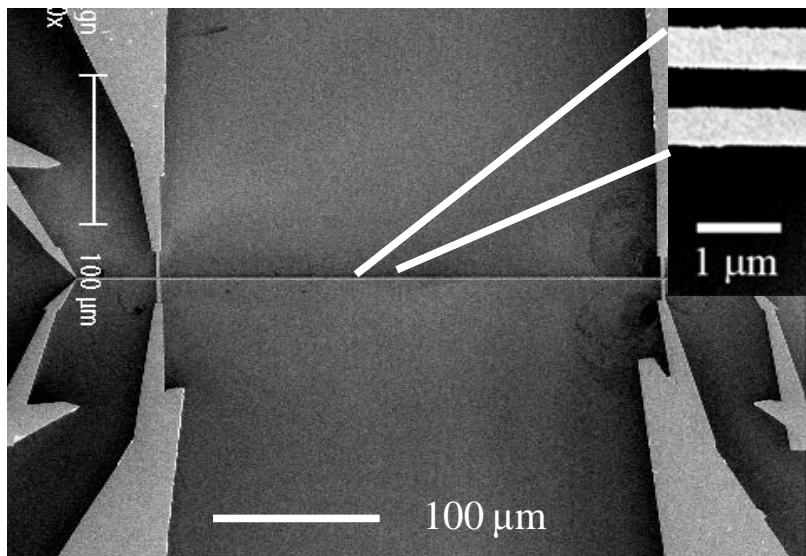


Fig.5.2 SEM image of the calibration sample, which consists of 2 parallel gold wires that are 400 μm long, 1 μm wide and 15 nm thick.

5.3.2 Noise thermometry⁸

The noise power spectral density of a resistor in thermal equilibrium at a temperature T is given by

$$S_V^{Johnson}(f) = 4k_BTR \quad (5.2)$$

where k_B is Boltzmann's constant and R is the resistance of the device. Since the thermal noise is directly proportional to temperature, it is an attractive means of measuring temperature. A noise thermometer is only dependent on the resistance of the sensor, which is easily measured. It is a primary thermometer, i.e., it does not need to be calibrated using other thermometers or standard references.

In this work, $S_V(f)$ of the gold wire sample is measured using a low-noise preamplifier (Stanford Research Systems, model SR560) and a spectrum analyzer (Stanford Research Systems, model SR780).

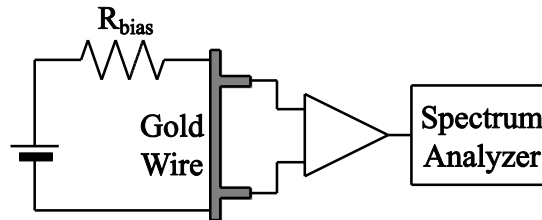


Fig. 5.3 Schematic of the experimental set-up for noise thermometry measurements. A low-noise battery is used to apply a voltage across the outer contact pads. The inner contact pads are used to measure the noise power spectral density function with a spectrum analyzer. The bias resistor was $3\text{ k}\Omega$.

⁸ Section 3.3 is based upon interaction with Prof. Kurdak and his team of the University of Michigan-Ann Arbor.

The circuit in Fig. 5.3 was used to measure the noise power spectrum of the gold wire sample. Three sources of noise are considered: amplifier noise, Johnson noise, and 1/f noise. The noise due to the input of the amplifier is thus given by

$$S_V(f) = S_V^{Amp}(f) + S_V^{Johnson}(f) + S_V^{1/f}(f) \quad (5.3)$$

where

$$S_V^{1/f}(f) = \frac{AI^2}{f} \quad (5.4)$$

and I is the current through the resistor and gold wire sample, and A is a constant. The Johnson noise for the resistor and the gold wire sample each is given by (5.2).

The DC bias has very low noise, so it is neglected in the AC circuit analysis. To calculate the Johnson noise referred to the input of the amplifier, first the AC input voltage is calculated by

$$V_{input} = V_B \left(1 - \frac{R_B}{R_H + R_B}\right) - V_H \frac{R_B}{R_H + R_B} \quad (5.5)$$

where V_B and V_H are the voltage noise of the bias resistor and gold wire sample, respectively, and R_B and R_H are the resistances of the bias resistor and gold wire sample, respectively. Then the following is obtained

$$S_V^{Johnson} = S_{VB} \left(1 - \frac{R_B}{R_H + R_B}\right)^2 + S_{VH} \left(\frac{R_B}{R_H + R_B}\right)^2 \quad (5.6)$$

where S_{VB} and S_{VH} are the individual values of the Johnson noise from the bias resistor and gold wire sample, respectively. Thus

$$S_V^{Johnson} = 4k_B T_0 R_B \left(1 - \frac{R_B}{R_H + R_B}\right)^2 + 4k_B T_H R_H \left(\frac{R_B}{R_H + R_B}\right)^2 \quad (5.7)$$

where T_0 is the absolute ambient temperature, and $T_H = T_0 + \Delta T$ where ΔT is the excess temperature of the gold wire sample above the ambient temperature. It should be noted that R_H is dependent on temperature linearly to a good approximation over a short temperature range, and is expressed as

$$R_H = (1 + \alpha_w \Delta T) R_{H0} \quad (5.8)$$

where α_w is the experimentally determined TCR of the gold wire, and R_{H0} is R_H measured at ambient temperature. The TCR α_w is 1711 ppm/K. For the temperature range of interest, the contribution from the TCR is negligible in the denominators of the expression for Johnson noise.

Thus, to a good approximation, $S_V^{Johnson}$ can be rewritten as

$$S_V^{Johnson} = 4k_B T_0 R_{eq} + 4k_B \Delta T \frac{R_{eq}^2}{R_{H0}} (1 + \alpha_w T_0 + \alpha_w \Delta T) \quad (5.9)$$

where R_{eq} is the Thevenin equivalent resistance of the circuit at the input of the amplifier and is independent of temperature. The entire noise due to the input of the amplifier is then given by

$$S_V(f) = S_V^{Amp}(f) + 4k_B T_0 R_{eq} + 4k_B \Delta T \frac{R_{eq}^2}{R_{H0}} (1 + \alpha_w T_0 + \alpha_w \Delta T) + \frac{AI^2}{f} \quad (5.10)$$

The first two terms are independent of current. Thus, by measuring the total noise as a function of current, then subtracting the $1/f$ term, ΔT may be determined. The second two terms are both zero when $I = 0$, so the excess noise can be defined as:

$$\begin{aligned} S_v^{Excess}(f, I) &\equiv S_v(f, I) - S_v(f, I = 0) - \frac{AI^2}{f} \\ &= 4k_B\Delta T \frac{R_{eq}^2}{R_{H0}} (1 + \alpha_w T_0 + \alpha_w \Delta T) \end{aligned} \quad (5.11)$$

The average excess noise power density can be plotted against I^2 (Fig. 5.4) to obtain the dependence of ΔT as a function of I^2 . The maximum DC current applied (4.5 mA) corresponds to an excess temperature of 16.3 K. Since the excess temperature scales quadratically with the applied current, the temperature change corresponding to other values of the applied current can be estimated using the following equation:

$$T = \frac{T_{max} I^2}{I_{max}^2} \quad (5.12)$$

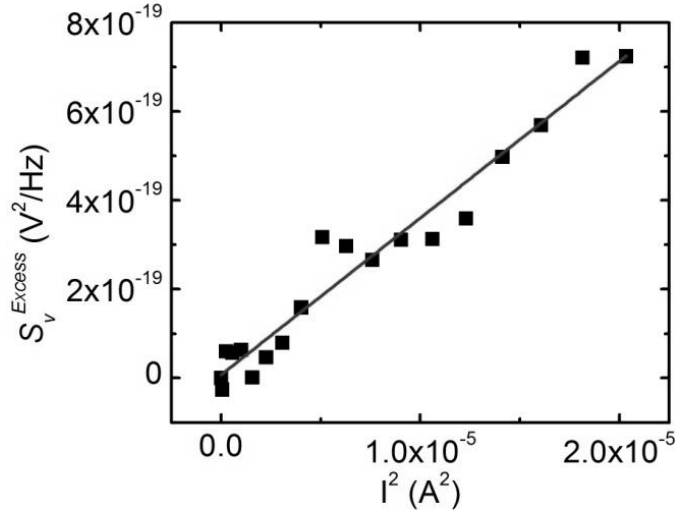


Fig. 5.4 Average excess white noise power density vs. I^2 . The experimental data (points) are linear, and a fit (line) gives a slope of $3.53 \cdot 10^{-14} \text{ V}^2/\text{A}^2 \text{ Hz}^{1/2}$. At 4.5 mA the increase in temperature is 16.3 K.

5.4 Experimental results and discussion

5.4.1 Thermal probe calibration and hot-spot scans

For these measurements a scanning system was developed. The system includes a closed-loop piezoelectric XYZ stage with a 100 μm range on each axis and nanometer resolution (PiezoJena, Tritor 100), and an XYZ motorized stage with a motion range of 28 mm on each axis and 0.05 μm microstep resolution (Zaber, model KT-LS28-MV). The system included a holder for the scanning thermal probe. A microscope was used to view the probe. The sample was brought into contact with the probe as the probe was monitored optically via the microscope and electrically via the response of the deflection-sensing element. The resistive change of the sensing element was directly measured using a micro-Ohm meter (Agilent, model 34420A), without a pre-amplifying circuit. The data were acquired with a LabView program.

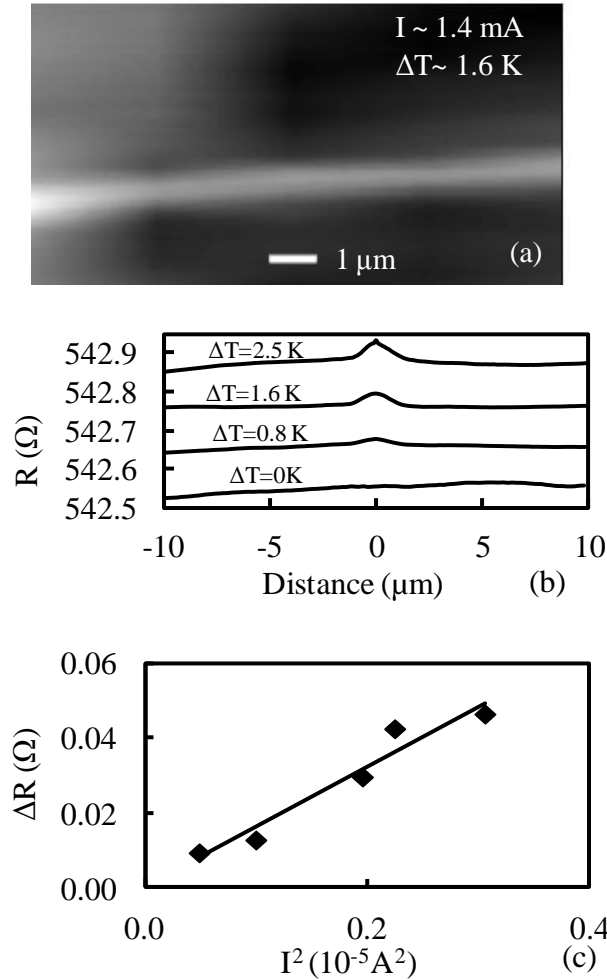


Fig. 5.5 (a) A two-dimensional XY plot of the scanning thermal probe's resistance change over the heated wire with ΔT of 1.6 K. (b) Line scans of the scanning thermal probe over the heated pre-calibrated wire at various temperatures of the wire, where the probe was scanned perpendicular to the wire. (c) The plot of the measured peak height, ΔR , as a function of bias currents squared applied at the heated wire shows that the probe signal is due to the excess temperature of the heated wire.

Fig. 5.5 (a) shows a two-dimensional XY plot of the scanning thermal probe's resistance over the heated wire with $\Delta T = 1.6$ K. It is important to note that the thermal image is not polluted by the topography since there is an identical un-heated wire next to the heated wire that is not observed in the thermal scan. The line scans in Fig. 5.5 (b) indicate that a larger temperature change results in a larger probe resistance change. The minimum detectable change in temperature of the sample is 0.4 K, corresponding to a change in resistance of the probe 17 ppm (the probe has a nominal resistance of 542.6 Ω). There is a small but detectable upward drift in the resistance of the probe, which is due to environmental temperature fluctuations during the scans. Fig. 5.5 (c) shows the measured peak ΔR as a function of bias currents squared applied, demonstrating that the probe signal is due to the excess temperature of the heated wire.

The temperature distribution of the probe is non-uniform because the hot-spot area is much smaller than the tip area. As a result, the average temperature of the probe is much less than the temperature of the hot-spot on the substrate. This motivated the introduction of a temperature conversion factor η such that:

$$\Delta T_{probe} = \eta \Delta T_{wire} \quad (5.13)$$

where ΔT_{probe} is the average change of the probe's temperature. Experimentally, η can be determined from the temperature coefficient of resistance of the scanning thermal probe and the ΔR_{probe} and ΔT_{sample} (which are obtained during the calibration scan). The temperature conversion factor, η , can then be used in future scans to calculate the real temperature change of any sample from the measured changes in ΔR_{probe} of the scanning thermal probe. Using equations (5.1) and (5.13) the average value of the temperature conversion factor η is 0.035 ± 0.007 . An FEA model

based on heat transfer theory is developed to determine what influences the value of η and how it can be improved.

5.4.2 FEA simulations

The mechanisms of heat transfer from the substrate to the tip [Rohsenow, 1998; Shi, 2002] are: solid-solid conduction, solid-gas conduction through the air gap, convection through the air gap, radiation from the heated substrate, and conduction through the liquid meniscus that forms between the tip and the substrate. Of these, solid-solid conduction is the dominant mode of heat transfer. The effects of sample heating on the probe's sensing element were simulated with a 2-D Comsol Multiphysics FEA model. These results were then used to derive a theoretical value for η . This model neglects heat transfer by radiation.

In the model, the 7- μm tip is composed of a 10-nm thick gold outer layer, a 100-nm SiO_2 intermediate layer, and the inner silicon layer. The top of the Si of the tip is set at room temperature (293 K). The tip rests on a 1- μm wide and 25-nm thick heated gold wire that is set at 294 K. Although a constant power boundary condition, rather than constant temperature is more appropriate, this and following FEA model have a linear behavior and any increase in power would result in a linear increase in the temperature field. In the end, the conclusions would be the similar. The gold wire rests on a 600- μm long, 300-nm thick SiO_2 insulating layer and on a 600- μm long, 300- μm thick silicon chip. A 240-nm wide liquid meniscus surrounds the probe tip at the contact point. The probe and gold wire are surrounded by air, which is set to have an open boundary and is convectively cooled. The wall boundaries of surfaces of the solid materials that are exposed to fluids (water and air) are defined in the model to account for convection. Seven cases with and without the presence of the liquid meniscus were considered, and these included tips with radii of curvature ranging from 100 nm to 700 nm.

A close-up of the temperature profile of the metal sensing element on a tip with a 300 nm radius of curvature is shown in Fig. 5.6. The contact area is < 10 nm. The hot spot size of the probe extends a few nanometers around the point of contact. However, the temperature of the entire probe is only slightly elevated above the ambient temperature. As the probe tip radius increases the probe sensitivity to substrate temperature also increases.

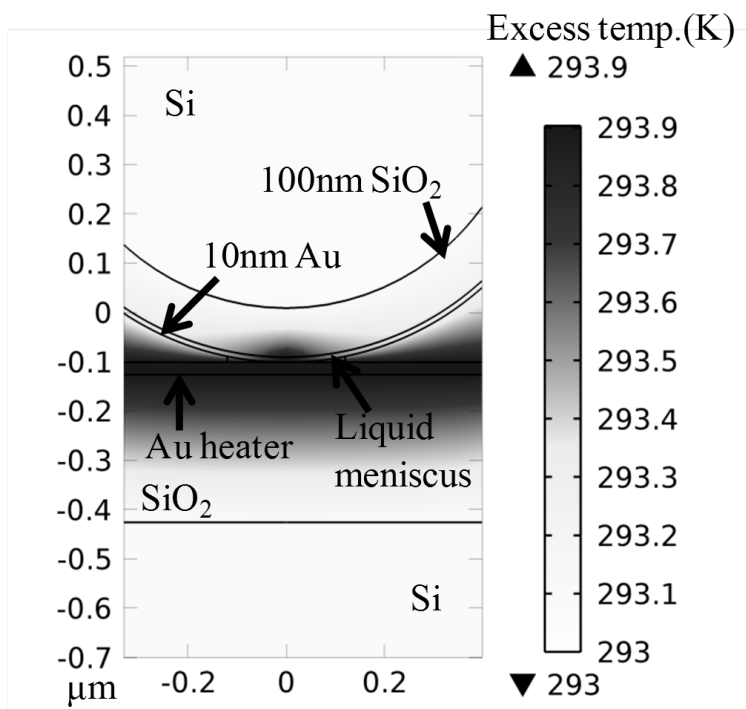


Fig. 5.6 Cross-sectional temperature distribution of a 600 nm radius tip.

Plots of the surface temperature of probe tip's metal element with varying radii vs. distance along the horizontal X-axis from the contact point is shown in Fig. 5.7. The simulations indicate that the probe tip's temperature distribution is highly non-uniform and

depends on its curvature. The tip with 700 nm radius exhibits the highest average temperature among the curvatures studied. The temperature of the sensing element sharply drops to room temperature at a distance of about 1 μm from the contact point. The hot-spot area is very small compared to the entire probe tip area.

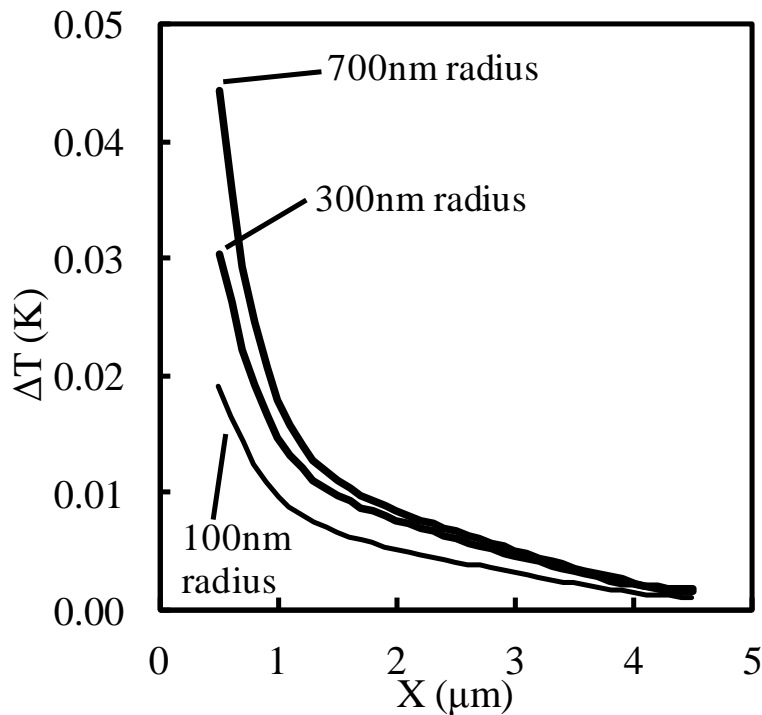


Fig. 5.7 A plot of the surface temperature of the metal element versus distance along the horizontal X-axis from the contact point for the three values of tip radii: 100 nm, 300 nm, and 700 nm.

The average change in the temperature of the 10 nm gold sensing element can be estimated from the simulation results. In this calculation the measured resistance is assumed to be dominated by the tip region. The lead and contact resistances were not included

in the calculations. The following equation is used, assuming a conical tip, to estimate the spatially-averaged temperature:

$$\langle T \rangle = \frac{1}{\pi r_0^2} \int_0^{r_0} 2 \pi r T(r) dr \quad (5.17)$$

The temperature conversion factor, η , is then calculated and ranges from 0.006 to 0.012, increasing with the radius of curvature of the tip (Fig. 5.8). These results indicate that there is a compromise between spatial resolution and temperature sensitivity in the probe design. Sharper probe tips lead to higher spatial resolution but lower temperature sensitivity.

The η value obtained from the experimental measurements is larger than the values obtained from the FEA model. This discrepancy could be due to one or more of the following reasons: a) a larger contact area between the tip and the sample, b) a larger liquid meniscus formed around the tip, or c) a larger probe tip radius.

Using FEA alternative probe geometries that lead to higher values of η were studied. The simplest way to enhance probe performance is to use a bow-tie metallization design, shown in Fig. 5.8, which focuses the current density at the area in contact with the sample. Calculations indicate that compared to the previous design, the bow-tie design leads to a 5- to 7-fold increase in the values of the conversion factor. Sensitivity can be further increased by depositing a thinner metal film over the tip, which often enhances the film's TCR, and by using different metals with higher TCR's.

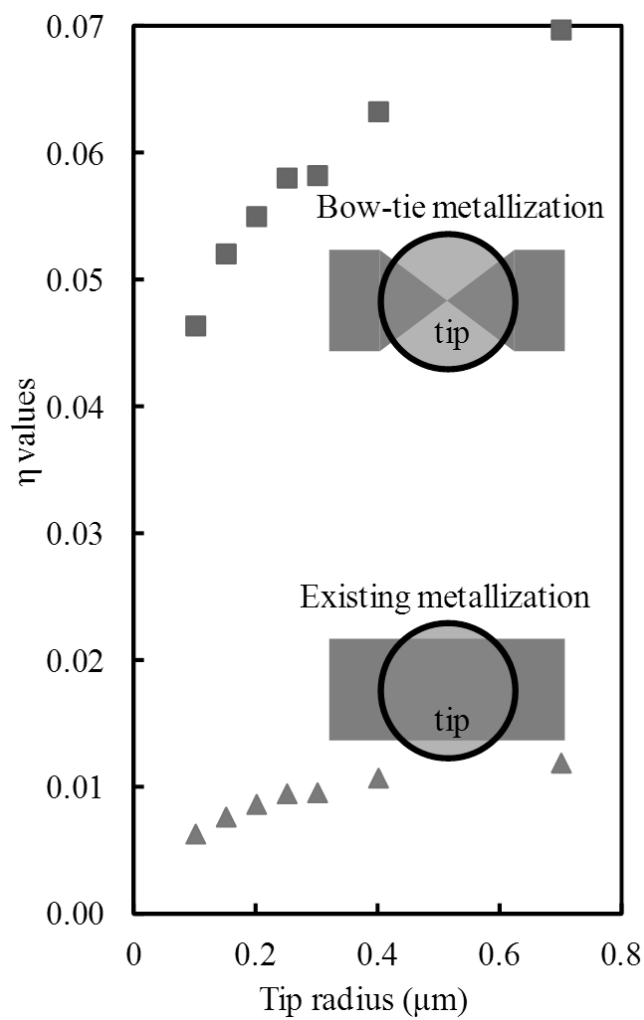


Fig. 5.8 The η values of various tip radii increase 5- to 7-fold compared to values obtained with the existing design.

5.5 Conclusions

In this chapter a key challenge of scanning thermal microscopy temperature profiling to accurately calibrate scanning thermal

probes by developing a 1 μm wide gold wire calibration sample has been addressed. The gold wire was pre-calibrated using noise thermometry. It was then used to obtain a direct correlation of resistance change of the probe with temperature changes of the gold wire. This technique allows users to account for the contributions of: the thermal contact resistance between the hot spot and the probe tip, the probe tip geometry including the radius of curvature, and the non-uniform heating of the probe, without contaminating the probe. Sample temperature changes as small as 0.4 K were detected, corresponding to 17 ppm changes in probe resistance.

A temperature conversion factor, η , was introduced to help compare the average change in temperature of the probe to the temperature of the heated wire. Both experimental and simulation results are in agreement indicating that η is < 0.035 . Thus, temperature changes on a substrate would increase the average probe temperature by $< 3.5\%$. Simulations and measurements reveal probe-to-probe variations in sensitivity due to probe geometrical non-uniformities. FEA of the probe-sample interface indicate that temperature sensitivity increases with increasing probe tip curvature. Therefore, there is a need for individual thermal probe calibration, that is addressed using the gold wire to calibrate each probe. In addition, these results indicate a compromise that has to be made in the probe design between a focus on increasing spatial resolution by decreasing the tip curvature or on increasing temperature sensitivity by increasing the curvature. FEA indicates that sensitivity can be improved by using a narrower metallization design on the sharp end of the tip like the bow-tie shape explored in the simulations.

6

Thin film deflection sensor for material characterization⁹

This chapter presents a silicon microcantilever probe with a 5 nm gold deflection sensor for the study of local mechanical properties such as adhesion and elasticity on a sample. The fabrication of these devices is described in Chapter 4.4. The probe has a dynamic range of tens of microns, which allows for a deeper insight into the mechanical properties of materials. The gauge factor of the 5 nm gold piezoresistive sensor is 4.1 compared to 3.24, which is the gauge factor for a 10 nm gold piezoresistive sensor with the same design, and the deflection sensitivity is 0.1 ppm/nm. The gauge factor shows a significant improvement compared to a 10 nm thickness gold deflection sensor. Noise analysis indicates a minimum detectable deflection of ≈ 0.7 nm. Topographical scans are demonstrated. Studies of adhesion and stiffness of two different samples demonstrate the usefulness of the probe in the investigation of local mechanical properties.

⁹ Parts of this chapter have been published in: A. Gaitas, T. Li, W. Zhu, "A Probe With Ultrathin Metal Piezoresistive Sensor for Scanning Probe Microscopy and Material Characterization", *Sensors and Actuators* (2011)

6.1 Introduction

Microcantilevers are used in a number of applications including atomic-force microscopy (AFM) [Albrecht, 1990], nanolithography [Majumdar, 1992], high-density data storage [Mamin, 1992], biological sensing [Florin, 1995], cell elastography [Costa, 2004], measurement of material properties such as adhesion, stiffness, elasticity and viscosity [Bhushan, 1999], and explosives detection [Fair, 1999]. Piezoresistive deflection-sensing elements are integrated onto micromachined cantilevers to increase sensitivity, and reduce complexity and cost. These sensing elements are made by selectively doping silicon [Tortonesi, 1993], by depositing and patterning metal or metal oxide films, such as gold [Calleja, 2003], indium tin oxide [Gregory, 2003], and nichrome [Allen, 2009], or by depositing and patterning other materials such as amorphous carbon [Peiner, 2006].

Compared with doped-silicon sensing elements, metal thin film elements have important advantages including simplified fabrication and the capability to scale down to smaller dimensions while maintaining sensitivities [Li, 2007]. Metallic sensing elements also enable the use of alternative substrate materials (such as polymers), that tend to exhibit higher compliance properties and improved thermal isolation [Johansson, 2005; Li², 2001]. Metal film sensing elements with thickness larger than 10 nm typically have gauge factors of about 2 or smaller [Calleja, 2003]. Ultrathin metal film sensing elements with thickness less than 10 nm have demonstrated increased piezoresistive sensitivity [Li, 1994].

In this chapter probes with metal ultrathin film sensors on silicon substrates for scanning probe microscopy and material characterization are developed. The probes operate without the need of a complicated optical lever required by AFM systems. In addition, the probes have a very large dynamic range of tens of

microns. This feature enables monitoring movement of tens of microns in the out-of-plane axis (Z-axis), which allows for a deeper insight into the mechanical properties of materials. For example, the adhesive forces on a surface can be studied in greater detail in order to characterize materials by monitoring the full range of the rupture force which is required to break the adhesion from the surface. These probes are also suitable for biological scanning in liquid environments by adding a thin insulating layer over the exposed metal film, overcoming the limitations of the optical lever on AFM caused by the laser refraction at the non-static liquid-air interface during scanning in liquids. Finally, compared with other approaches such as optical lever detection and piezoelectric pick-up, piezoresistive sensing is relatively simple to expand to a one or two dimensional probe array for higher throughput multi-location measurements.

6.2 Cantilever mechanics, the gauge factor, and noise

6.2.1 Cantilever mechanics and the gauge factor

The spring constant of a rectangular cantilever is given by

$$k = \frac{F}{\Delta z} = \frac{2 E I}{L^3} = \frac{E W t^3}{4 L^3} \quad (6.1)$$

where F is the force applied, Δz is the displacement of the cantilever at the tip, W , L , and t are the width, length, and thickness respectively, E is the modulus of elasticity, and I is the moment of inertia of a rectangular cantilever.

The resonance frequency f_0 can be expressed as:

$$f_o = 0.162 \frac{t}{L^2} \sqrt{\frac{E}{\rho}} \quad (6.2)$$

where ρ is the density of the cantilever material.

The change in resistance, ΔR , can be converted into corresponding force values using the gauge factor. The gauge factor of the metal piezoresistive sensor is given by the following equation

$$\frac{\Delta R}{R} = K e = \frac{K}{E} \sigma \quad (6.3)$$

where K is the gauge factor, E is the Young's modulus of the cantilever material, e is the strain, σ is the average stress in the metal sensor.

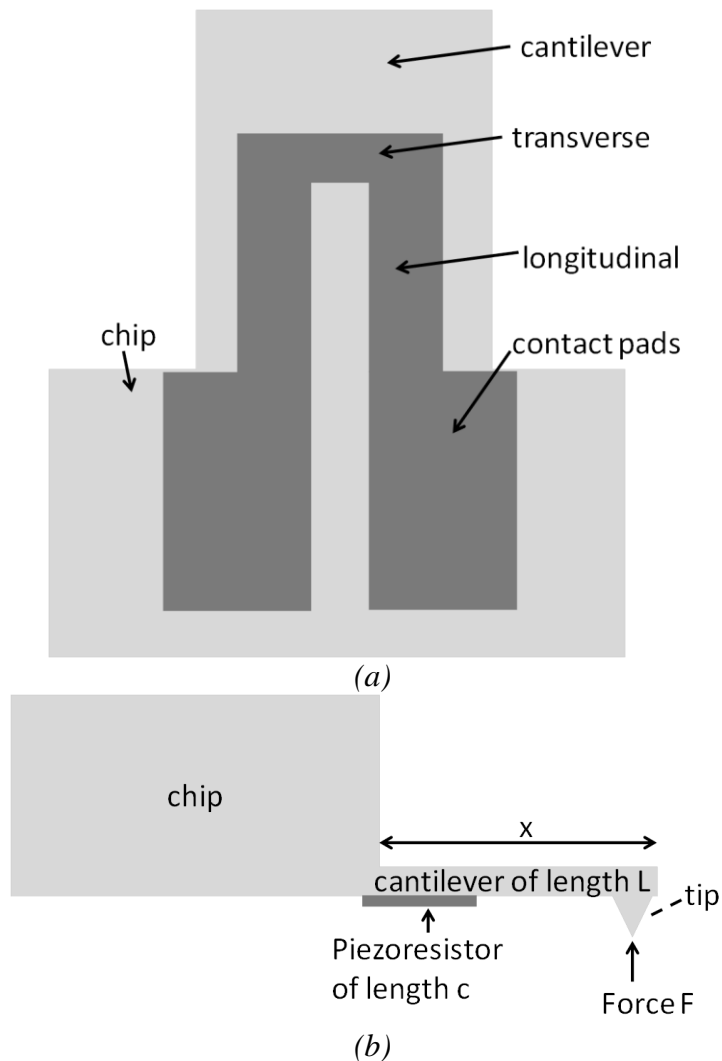


Fig. 6.1 (a) Diagram of a typical rectangular cantilever with a resistor for piezoresistive sensing. (b) Schematic of a cantilever with a metal sensing element that serves as a piezoresistor with longitudinal length c .

The change in resistance can be written as a function of longitudinal, l, and transverse, t, gauge factor and strain

$$\frac{\Delta R}{R} = K_l e_l + K_t e_t \quad (6.4)$$

In these designs longitudinal resistance is maximized, while transverse resistance of the resistor is minimized in order to maximize the change in resistance with strain.

The average stress of the sensor and the stress are estimated using cantilever analysis [Thaysen, 2001; Sarid, 1991] and are given by

$$\langle \sigma \rangle = \frac{1}{c} \int_0^c \sigma(x) dx \quad (6.5)$$

$$\sigma(x) = \frac{F (c - x) y}{I} \quad (6.6)$$

where x is the distance from the root of the cantilever, c is the length of the piezoresistor, y is the distance from the neutral plane of the cantilever to the metal sensor in the thickness direction, L , W and t are the length, width and thickness of the cantilever, respectively, and F is the equivalent force that can be applied at the cantilever tip to reach the same displacement. The force can be replaced with $F = k \Delta z$, where k is the spring constant and Δz is the displacement of the cantilever at the tip. Using the spring constant, k , for a rectangular cantilever and solving the above equations the overall equation becomes

$$\frac{\Delta R}{R} = \frac{3}{2} K \frac{(L - c/2)t}{L^3} \Delta z \quad (6.7)$$

The deflection sensitivity is defined by solving equation (6.7) for $(\Delta R/R)/\Delta z$, and its value can be experimentally calculated from the slope of $(\Delta R/R)$ vs. Δz .

6.2.2 Noise

There are a number of different sources of noise that are worth describing here since these will be mentioned in this and in future chapters. Thermal noise is a thermodynamic noise that is only dependent on the resistance of the sensor. For frequencies < 1 MHz, and temperatures, $T > 25$ K, the noise voltage power spectral density across a resistor in thermal equilibrium can be approximated to better than 0.0001% according to Nyquist's theorem by

$$\overline{V_T^2} = 4k_B T R \Delta f \quad (6.8)$$

where k is Boltzmann's constant, f is the frequency, Δf is the noise measurement's bandwidth, and R is the sensor's resistance. Johnson noise is experimentally measured using a spectrum analyzer to capture the power spectral density function, $S_V(f)$:

$$S_V(f) = (V_{\text{rms}}^2) / \Delta f = 4 k_B R T \quad (6.9)$$

The $1/f$ noise is frequency dependent. The noise power spectral density function is given by

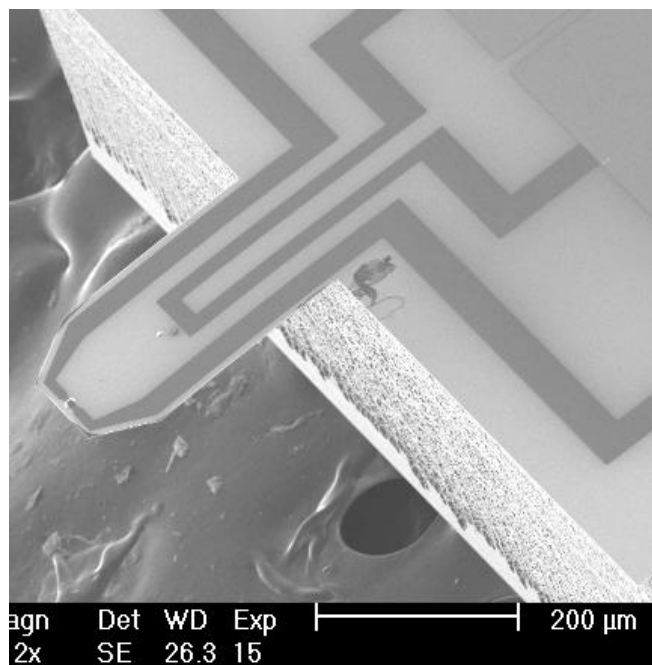
$$S_I(f) = \frac{K I^2}{\nu f} \quad (6.10)$$

where $S_I(f)$ is the noise power spectral density function, K is the noise prefactor, I is the bias current, ν is the volume of the device, and f is frequency. The noise prefactor, K , can be estimated from

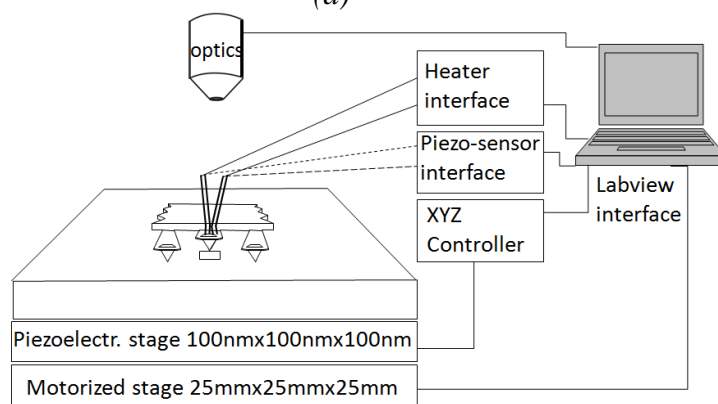
the data obtained from the spectrum analyzer. K is independent of the dimensions of the device.

6. 3 Experimental set-up

The cantilever is shown in Fig. 6.2 (a) and the experimental set-up is shown in Fig. 6.2. (b). The change in resistance of the deflection sensing element of the cantilever is directly measured using a micro-Ohm meter (Agilent, HP-34420A), without the need of an interface amplifying circuit. Optionally there is a variable power supply (Keithley 2400) for heating the thermal element of the device. The data are acquired with a LabView program. A piezoelectric XYZ stage with 100 μm range and nanometer resolution on each axis (PiezoJena, Tritor 100) is used to move the sample underneath the probe array. A Zaber motorized stage is used for larger movements in the XYZ direction.



(a)



(b)

Fig. 6.2 (a) The cantilever probe used in this chapter and chapter 5. (b) The experimental set-up used to conduct these studies.

6.4 Experimental results and discussion

The overall resistance of the sensing element is $\approx 1,773 \Omega$. The parasitic resistance of the inactive portions of the metal-line resistor can be calculated using the geometry and the measured sheet resistance. Additional resistances from the cabling and the wirebonding are less than 1Ω and therefore do not have a significant contribution to the overall resistance. Thus, the active piezoresistive sensing part of the sensing element has a resistance of $\approx 516 \Omega$.

The noise performance of the sensor is evaluated by biasing the metal-film resistor with the built-in battery-based power source in a low-noise current preamplifier (Stanford Research Systems SR570). The output voltage of the current preamplifier is then fed into a spectrum analyzer (Agilent 4395A) for noise measurement.

No $1/f$ noise was observed between the frequency range from 10 Hz (equipment limitation) to 1 KHz, and the white noise floor was found to be $\approx 22 \text{ nV}/\sqrt{\text{Hz}}$. This is ≈ 3 times higher than the calculated Johnson noise spectrum based on the nominal overall resistance of the sensing element, and may be related to the thermal vibration noise of the cantilever. The minimum detectable deflection is given by

$$\Delta z_{min} = \frac{\bar{V}_n}{I_{Bias}} \cdot \frac{1}{R} \cdot \frac{1}{S_Z} \quad (6.11)$$

where \bar{V}_n is the total noise voltage over the measurement bandwidth ($\approx 30 \text{ Hz}$ from the micro-ohm meter), I_{Bias} is the bias current used in the resistance measurement (1mA or less), R is the nominal resistance of the sensing element, and S_Z is the sensitivity of the piezoresistive sensor defined as $\Delta R/R/\Delta z$ and obtained by experiments as discussed below. The total noise of the micro-ohm meter is a lot less than the noise from the device and it is been

ignored in the calculation. Thus the minimum detectable deflection from equation (6.11) is ≈ 0.7 nm.

Fig. 6.3 (b) shows a $20\mu\text{m}$ line scan over the top surface of a $10\mu\text{m}$ pitch square grating with $1\mu\text{m}$ height shown in Fig. 6.3 (a). The curve in Fig. 6.3 (b) is the plot of the change in resistance, ($\Delta R/R$) vs. the in-plane (XY plane) movement, and shows the scanned surface profile of the grating. A $1\mu\text{m}$ change in the deflection of the cantilever tip corresponds to an approximately 0.1Ω change in resistance.

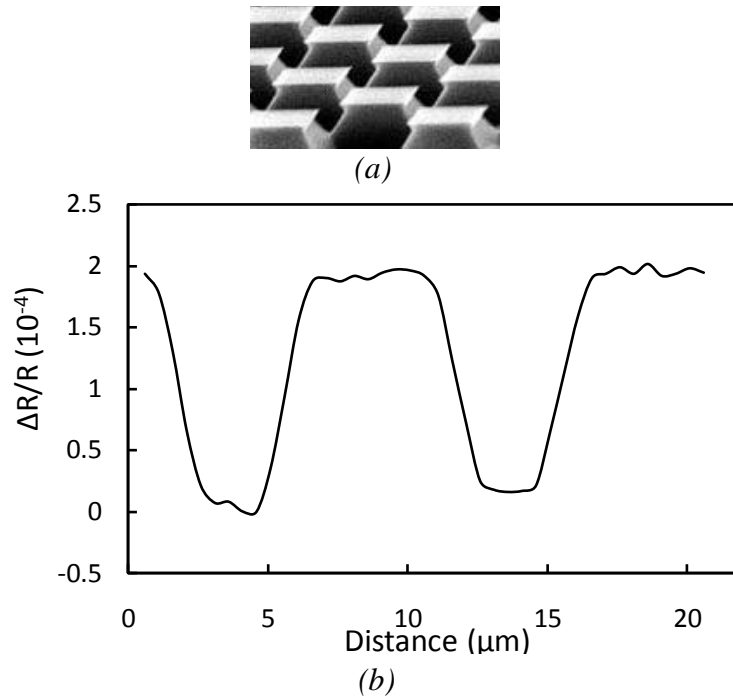


Fig. 6.3 (a) The $10\mu\text{m}$ -pitch square grating with $1\mu\text{m}$ height. (b) Measured $\Delta R/R$ vs. in-plane scanning displacement in a $20\mu\text{m}$ line scan over a $10\mu\text{m}$ -pitch square grating with $1\mu\text{m}$ height.

The attractive and repulsive forces between a probe tip and sample surface are of interest as they can provide information about mechanical properties of the probe and of the sample (such as adhesion and elasticity). Typically, with an AFM, the cantilever is moved in Z axis towards the sample (trace) and then away from the sample (re-trace). The deflection of the cantilever is detected by a photodiode plotted against the Z-axis scanner movement, and then analyzed.

The same capability can be realized by this probe, without the need of the complicated optical pickup used in the AFM. Resistance vs. displacement curves are produced using the probe and samples on the XYZ piezoelectric stage. The change in resistance can then be translated into the change in force as described in [Calleja, 2003], which can be further used to extract the attractive and repulsive forces, as well as corresponding material properties. Besides the benefit of simplified signal readout, the closed-loop piezoelectric XYZ stage also provides larger measurement and interaction range ($>40\ \mu\text{m}$), while in a typical AFM this range is typically limited by the piezoelectric tube scanner to $\approx 5\ \mu\text{m}$.

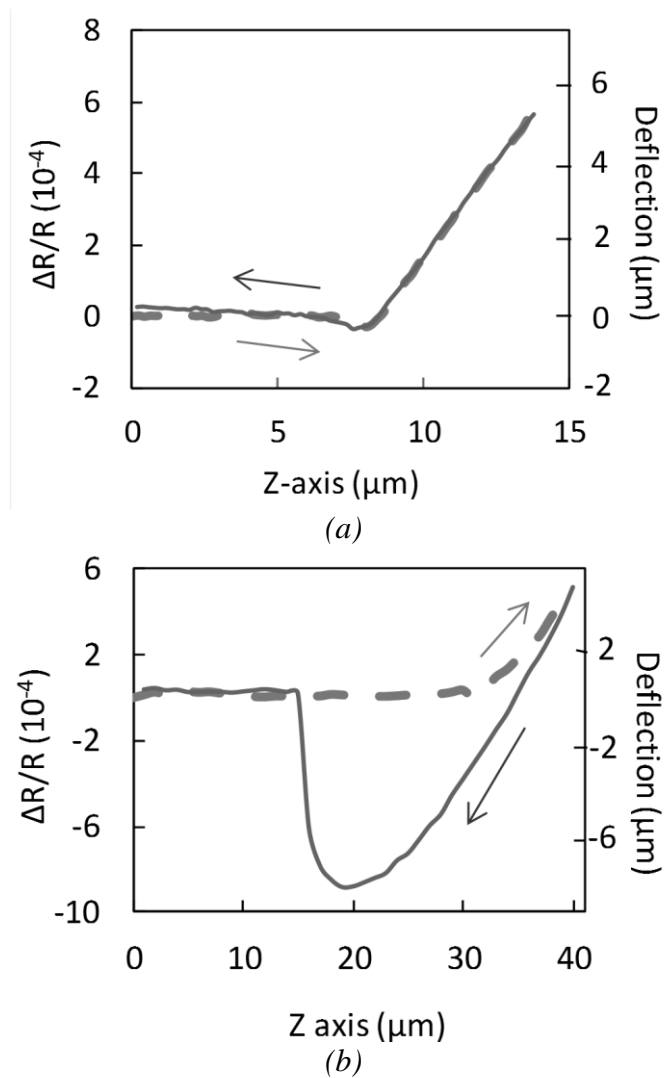


Fig. 6.4 Measured $\Delta R/R$ vs. out-of-plane probe movement (similar to an AFM force-curve) on two different materials. Force-curves on: (a) a glass substrate; (b) an elastomer (C6-235).

Curves of the change in the probe resistance with displacement in Z-axis on two different materials are shown in Fig. 6.4. Fig. 6 (a) is a curve on a glass substrate and Fig. 6.4 (b) is on an elastomer (Dow Corning, C6-235). The arrows indicate the direction of the movement. The blue thick line represents the trace (probe and sample moving toward each other) and the red thin line represents the re-trace (probe and sample moving away from each other). The vertical axes are $\Delta R/R$ on the left and corresponding calculated cantilever deflection on the right, and the horizontal axis is the Z-axis movement of the sensing element toward and away from the sample. At a Z-axis value of 0 μm the probe tip is not touching the sample. As the value on the Z-axis increases, the sample is brought closer to the tip. An attractive force deflects the probe toward the sample and thus there will be a decrease in the resistance of the element. A repulsive force deflects the probe away from the sample and there will be an increase in resistance.

As can be seen in Fig. 6.4 (a) and Fig. 6.4 (b), when the probe gets very close to the sample, it jumps into contact when it feels a sufficiently strong attractive force from the sample. As soon as the tip is in contact with the sample, the probe starts being pushed into the sample and the deflection will increase. This is translated into an increase in the slope of the curves in Fig. 6.4, which indicates that contact occurs around a value of 8.2 μm on the Z-axis for Fig. 6.4 (a) and 31 μm for Fig. 6.4 (b). These values are arbitrary because the initial probe-sample distance is randomly chosen for this experiment. The slope and shape of the line is a measure of the elasticity of both the sample and the probe. The slope of the line on hard glass is 0.0553 $\Omega/\mu\text{m}$ (Fig. 6.4 (a)), while the slope on the elastomer is 0.0304 $\Omega/\mu\text{m}$ (Fig. 6.4 (b)), demonstrating, as expected, that the elastomer is more elastic than glass. The deflection sensitivity of the probe ($(\Delta R/R)/\Delta Z$) can be extracted from the slope of the curve on glass and is ≈ 0.1 ppm/nm. Using equation (6.7) and the experimental data shown in Fig. 6.4 (a), the gauge factor of the metal piezoresistive sensor is calculated at 4.1

± 0.1 . A device with the same design but with a 10 nm thick sensing element has a gauge factor of 3.24 (Chapter 7). Thus a thinner device has improved sensitivity.

After reaching a certain predetermined Z-axis value the sample is moved away from the probe (re-trace). Initially, the curve is similar to the trace curve (approach), because the adhesive forces cause the probe to remain adherent to the sample even after passing the initial contact point. It can be seen that adhesive forces between the probe and the glass sample (Fig. 6.4 (a)) are weaker than the forces on the elastomer (Fig. 6.4 (b)). After moving a further distance away from the sample the adhesion is broken, and this value corresponds to the rupture force to break the adhesion from the surface. For Fig. 6.4 (a) this value represents a change in resistance of $\Delta R=0.0106 \Omega$ or a $\Delta Z \approx 190$ nm and for Fig. 6.3 (b) represents a change in resistance of $\Delta R=0.4654 \Omega$ or a $\Delta Z \approx 8.37 \mu\text{m}$. As expected, the greater the adhesion the greater the value of ΔR as evidenced from the comparison between the two graphs.

Knowing the probe elasticity enables to extract the sample elasticity from the measurement curve. The Young's modulus of the elastomer can be derived from: the measured piezoelectric stage Z-axis movement, the cantilever's deflection (by converting the change in resistance to the change in distance based on the calibration data), the probe radius, and the cantilever's spring constant. From the equation provided by Soofi et al. [Soofi, 2009] by solving for the Young's modulus, E, the equation becomes:

$$E = \frac{0.75 k (d - d_o)(1 - \nu^2)}{\sqrt{r} [(z - z_o) (d - d_o)]^{3/2}} \quad (6.12)$$

where z is the measured piezoelectric stage Z-axis movement, z_o is the value of z at the probe contact point, d is the cantilever's deflection, d_o is the value of d at the probe contact point, k is the cantilever spring constant, ν is Poisson's ratio (assumed to be 0.5

for a soft and incompressible material such as the elastomer sample [Soofi, 2009]), and r is the probe radius (100 nm). The cantilever spring constant is derived from the equation (6.1):

$$k = E_{Si} w t^3 / (4L^3) \quad (6.13)$$

where E_{Si} is the Young's modulus of silicon (185 GPa), w is the width of the cantilever \approx (200 μm), t is the thickness of the cantilever (2 μm), L is the length of the cantilever (300 μm). The effect of the metal and oxide layers is ignored considering their much smaller thicknesses compared with that of the silicon layer. The spring constant is calculated to be ≈ 2.74 N/m. From equations 6.12 and 6.13 and from the measured data presented in Fig. 6.4 (b), the Young's modulus of the elastomer is 2.6 ± 1.0 MPa, which is close to the manufacturer's published value of ≈ 1.4 MPa [Dow]. The discrepancy may be caused by the uncertainty in the spring constant, tip diameter, and the Poisson's ratio. Calibration can be performed to further improve the accuracy of the measurement.

6.5 Conclusions

A cantilever probe with an ultrathin film metal sensor is investigated for scanning probe microscopy and material characterization. The probe has a very large dynamic range, enabling monitoring movement of tens of microns in the out-of-plane axis. The rectangular cantilever is 200 μm wide and 300 μm long. It is made from silicon and silicon oxide with a total thickness of 2 μm and a 5 nm gold deflection sensing element. The gauge factor of the probe is 4.1 ± 0.1 . Topographical scans capabilities were demonstrated. Plots of the change in resistance and cantilever deflection with the displacement of the sensing element on different materials demonstrate that the probe can be used to distinguish between materials with different mechanical properties. Furthermore, the probe was used to estimate the Young's modulus of the elastomer studied.

7

A Piezo-thermal probe for thermomechanical analysis¹⁰

Thermomechanical analysis (TMA) is widely used to characterize materials and determine transition temperatures and thermal expansion coefficients. Atomic-force microscopy (AFM) microcantilevers have been used for thermomechanical analysis (TMA). The micromachined probe, that was described in Chapter 4.4, includes two embedded gold sensors with 10 nm thickness: one for measuring the mechanical movement of the probe (deflection) and another for providing localized heating. The probe reduces costs and complexity and allow for portability thereby eliminating the need for an AFM. The sensitivity of the 10 nm gold deflection element ($(\Delta R/R)/\text{deflection}$) is 0.1 ppm/nm and its gauge factor is 3.24. The melting temperature of naphthalene is measured near 78.5 °C.

¹⁰ Parts of this chapter were published in: A. Gaitas, S. Gianchandani, W. Zhu, "A Piezo-Thermal Probe for Thermomechanical Analysis", Review of Scientific Instruments (2011)

7.1 Introduction

Thermomechanical analysis (TMA) is widely used to characterize materials such as polymers and determine transition temperatures and thermal expansion coefficients. Typically a probe is placed on a sample with a known force. As temperature is increased changes in the mechanical properties are recorded [Riga 1991]. Atomic-force microscopy (AFM) micro-cantilevers have been used for TMA to reduce analysis times, analyze small samples, and provide spatial information [Hammiche, 2001; Price, 1999; Hammiche, 2000]. This is done using a miniature heater probe with an AFM. The miniature cantilever probe is locally heated while the AFM photo-detector is used to monitor the deflection of the cantilever. Any changes such as transition temperatures can be identified from the probe movement [Price, 1999; Hammiche, 2000].

In this chapter the micromachined probe that was developed and described in Chapter 4.4 includes two embedded sensors: one for measuring deflection and another for providing localized heating. This probe reduces the cost and complexity associated with TMA by eliminating the need for an AFM or other TMA systems, while at the same time enhancing portability. Furthermore, this probe is better suited for high throughput melting point measurements.

Heating and deflection-sensing cantilevers have been independently developed in the past. These sensing elements are made by doping silicon [Chui, 1996; Chui, 1998; Tortonesi, 1993] or by depositing metal films on cantilevers [Li, 2007]. Cantilever metal sensing elements typically range in thickness from 100 nm to 30 nm [Li, 2007]. Metallic thin film sensing elements can have high gauge factors [Li, 1994]. Thin film elements have other important advantages, including simplified fabrication and a lower manufacturing cost. Metallic sensing elements also enable the use of alternative substrate materials (such as polymers), that tend to

exhibit higher compliance properties and improved thermal isolation.

The probes described in this chapter include a monolithic integration of a heating element (which can also be used for temperature sensing) and a deflection (or displacement) sensing element. Gold films of 10 nm thickness were deposited on a silicon cantilever to form both sensing elements. Integration of these functions within a single cantilever is expected to increase sensitivity, reduce the overall complexity of the set-up, and reduce cost.

7.2 Heat transfer between cantilever tip and substrate

In this section the heat transfer mechanism between the tip and the substrate are studied. This study will assist in optimizing the cantilever design and estimate how heat is distributed on a sample. Localization of heating and temperature measurement is crucial in achieving controlled measurement of heat, in melting of materials, and in a number of applications such as localized CVD, patterning, and nanofabrication using thermal probes. The main mechanisms of heat transfer from the tip to the substrate are described in Chapter 5.4 [Nelson¹, 2007; Nelson³, 2007; King, 2002; Li 2, 2001; Lefèvre, 2006]. In this case the tip is covered with a thin film of gold, which has a thermal conductivity of 318 W/(mK). The thermal conductivity of the sample, naphthalene, is 0.12 W/(mK). The temperature of the tip, as derived from the thermal circuit, is very close to the temperature at the interface given that the thermal conductivity of naphthalene is very small compared to the thermal conductivity of gold. Thermal conduction (and contact resistance) at the interface depend on the contact area and the contact pressure [Fischer, 2008; Nikiforov, 2011]. The force vs. displacement curve was used to control the contact pressure. Based on the thermal calibration method, as described below, the melting point of naphthalene was experimentally

measured with 3.6% deviation from the standard value provided by the manufacturer.

Finite element analysis with Comsol Multiphysics was used to simulate the effects of probe tip heating on the sample surface. These results were then used to determine the temperature at the surface of the melted material. In this model heat transfer by solid-solid conduction, solid-liquid conduction, solid-air conduction, and heat transfer by convection are accounted for. The model does not take into account for heat transfer by radiation. Due to the axial symmetry of the tip-substrate structure, a 2-D model is sufficient to capture the details of the process.

Cross sectional temperature distribution are shown in Fig. 7.1. The tip is composed of a 10 nm gold heating/sensing element that surrounds its outer layer, a 100 nm SiO₂ intermediate layer, and the inner silicon layer. The silicon chip extends about 2 μm beyond the tip in order to simulate the SOI wafer. The tip rests on a 10 μm wide and 1 μm thick silicone block (to simulate the organic materials used to study melting point temperatures). The silicone block rests on a 600 μm x 300 μm silicon chip. The bottom of the Si chip (300 μm away from silicone) and the top silicon part of the cantilever is set at room temperature at 293 K. The 10 nm thick heating element surrounding the tip is set at 294 K. A liquid meniscus 240 nm wide surrounding the tip at the contact area is also included. The tip and the silicone sample are surrounded by 600 μm x 300 μm of air. Conductive and convective heating has been accounted for. The air is set to have an open boundary and is convectively cooled beyond the 600 μm x 300 μm area. The wall boundaries of surfaces of the solid materials that are exposed to fluids (water and air) are defined in the model to account for convection. In this model the tip has a radius of curvature of 100 nm (which result in 200 nm tip diameter).

In Fig. 7.2 a close up of the temperature distribution is shown with contact area < 10 nm. The spot size extends few nanometers around the point of contact. A plot of the surface temperature of silicone with distance from the contact is shown in Fig. 7.3. The liquid meniscus is also included in the simulations. The temperature of the sample is close to the temperature of the heated tip at contact and sharply drops to an average temperature that is still higher than the ambient at a distance of about $1 \mu\text{m}$ from the contact point. The simulation results suggest that there is a small area of the sample that is heated at the temperature of the heater tip.

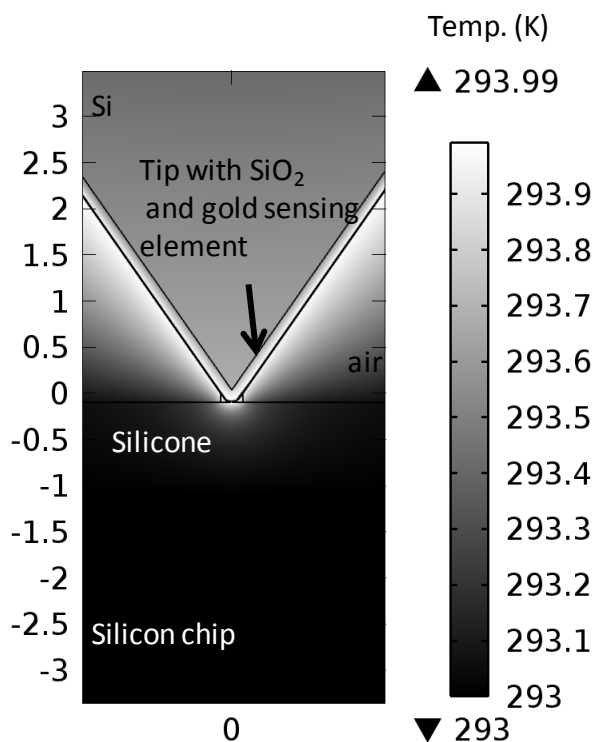


Fig. 7.1 The cross sectional temperature distribution of a tip with 100 nm radius of curvature is shown.

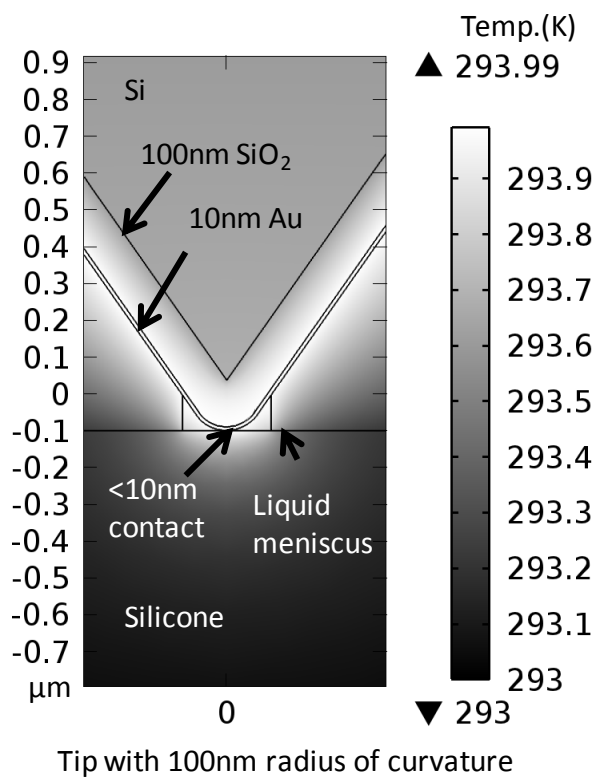


Fig. 7.2 A close up of the temperature distribution of a 100 nm radius of curvature tip. The contact area is < 10 nm.

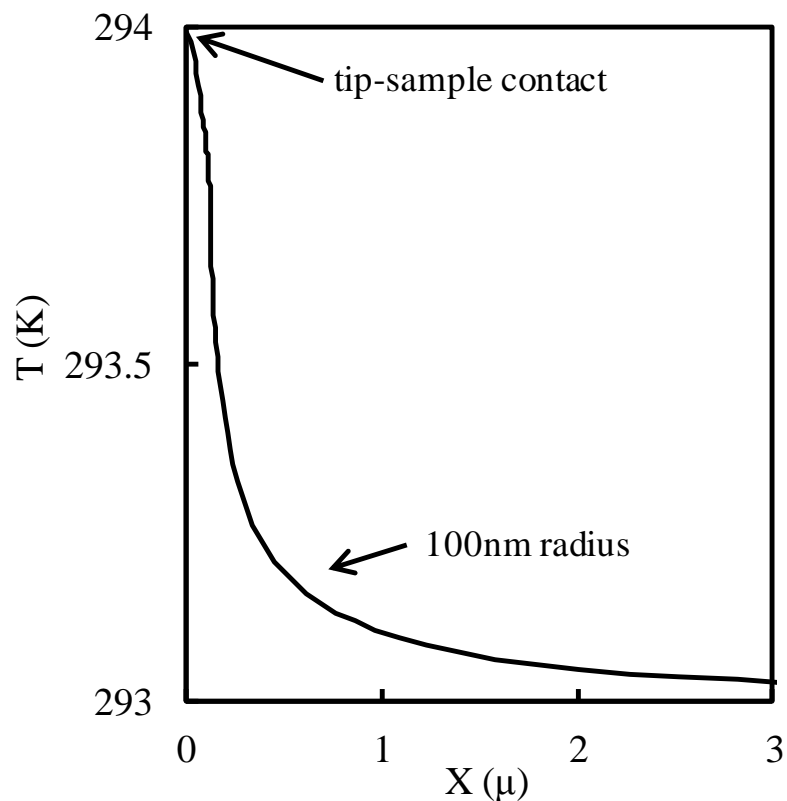


Fig. 7.3 A plot of the surface temperature of the silicone sample is shown. The temperature of the Silicone surface reaches the probe tip temperature at the point of contact.

7.3 Scanning system

For these measurements a scanning system is developed as described in chapter 5. The system includes a closed loop piezoelectric XYZ stage with 100 μm range on each axis and nanometer resolution (Tritor 100 PiezoJena) and an XYZ motorized stage with motion range of 28 mm on each axis and 0.05 μm microstep resolution (Zaber, model KT-LS28-MV). The

system includes a holder for the piezo-thermal probe. A microscope is used to focus on the probe. The sample is brought in contact with the probe while monitoring the probe optically and electrically via the response of the deflection sensing element. All measurements were conducted in room temperature and atmospheric pressure.

The resistive change with distance of the deflection sensing element was directly measured using a micro-Ohm meter (Agilent, model 34420A), without the need of an interface amplifying circuit. The data are acquired with a LabView program. A piezoelectric XYZ stage, described previously, is used to move the sample underneath the probe.

7.4 Experimental results and analysis

7.4.1. Displacement sensing

After removing the parasitic resistance, the resistance of the displacement sensing element is 105.4Ω . Additional resistances from cabling and wirebonding are less than 1Ω and therefore do not have a significant contribution to the overall resistance. The noise spectrum of the deflection sensing element is measured and found to be dominated by Johnson noise.

The change in resistance of the deflection sensing element with displacement (resistance vs. distance curve) of the probe on a glass slide generated a figure similar to Fig. 6.4 (a). The slope of the line was $0.01 \Omega/\mu\text{m}$. Therefore a $1 \mu\text{m}$ movement corresponds to approximately 0.01Ω change in resistance. The deflection sensitivity of the probe ($(\Delta R/R)/\text{deflection}$) was 0.1 ppm/nm . Using equation (6.7) and the experimental data, the gauge factor of the sensor is calculated at 3.24.

7.4.2. Thermomechanical analysis

Precise temperature calibration is required for melting point measurements where temperature must be controlled with accuracy. A number of ways used to calibrate a thermal probe have been comprehensively reviewed [Nelson¹, 2007; Nelson², 2007; Fischer, 2008] and include: isothermal (hotplate) calibration [Fischer, 2008], melting point standard calibration [Lee, 2004; Fryer, 2000; Blaine, 1999; Hammiche, 1996], using the linearity of heater resistance with temperature [Lee, 2005], and calibration methodology using Raman thermometry [Nelson², 2007]. Here a small thermocouple of the same size as the tip was used to calibrate the probe. The difficulty in determining the temperature at the interface of the probe-sample has been identified by others [Fischer, 2008; Nelson³, 2007]. Since the relation between power or resistance and temperature is dependent on substrate heat losses, all of the existing calibration methods will be somewhat affected by different samples. In order to estimate the temperature at the interface, thermal resistance circuits of the probe and sample have been developed [Nelson³, 2007; Yue, 2010].

The heater is independently calibrated using a 12 μm size thermocouple (Omega, CHAL-0005) that is brought into contact with the heating element. The cantilever is placed on a motorized stage. A variable power supply (Keithley 2400) is used to increase the power through the heating element while monitoring the temperature with the thermocouple. Fig. 7.4 shows the near linear relationship of the power through the heating element with temperature. Fig. 7.4 is used to derive the temperature from a known value of power through the heating element.

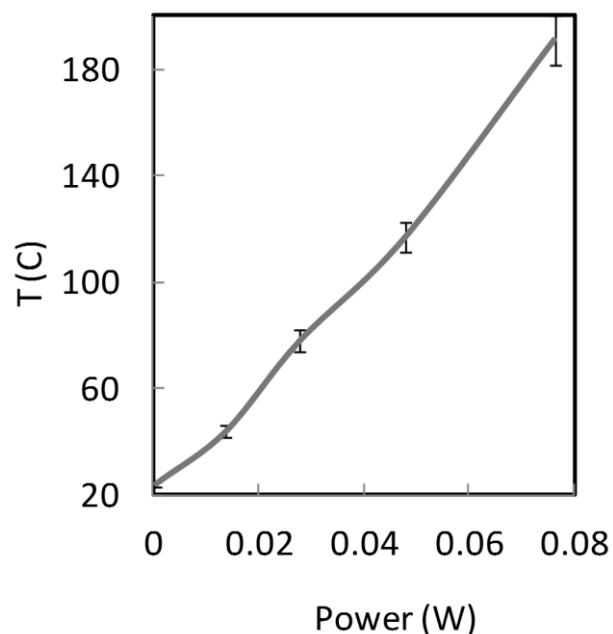


Fig. 7.4 A near linear relationship of power with temperature is observed. A variable power supply (Keithley 2400) was used to increase the power through the heating element while monitoring the temperature with an external thermocouple brought in contact with the tip.

The melting temperature of naphthalene $C_{10}H_8$ (Sigma-Aldrich, Inc., 01422-250MG, Melting Point Standard) with a melting point between 79-81 °C (± 0.3 °C) is measured with the piezo-thermal probe. First, the sample and probe are brought in contact. A variable power supply is used to increase the power through the heating element in small increments (with heating rates up to 25°C/sec), while the change in resistance of the deflection sensing element is directly measured using a micro-Ohm meter. The calibration curve of Fig. 7.4 is used to convert power to the corresponding temperature. Figures 7.5 and 7.6 show the change in resistance (Fig. 7.5) and the change in the first order derivative (dR_{piezo}/dT) (Fig. 7.6) of the deflection sensing element on the

vertical axis with temperature increase of the heating element on the horizontal axis. As expected the increase in temperature caused by incremental increase in power through the heating element also increases the resistance of the nearby deflection sensing element. However, near the reported melting temperature a local decrease in resistance is observed in Fig. 7.5 at 78.5 °C. In Fig. 7.6 a local minimum is observed at 78.5 °C. The local decrease in resistance is interpreted as a movement of the probe toward the sample, an indent, caused from the melting.

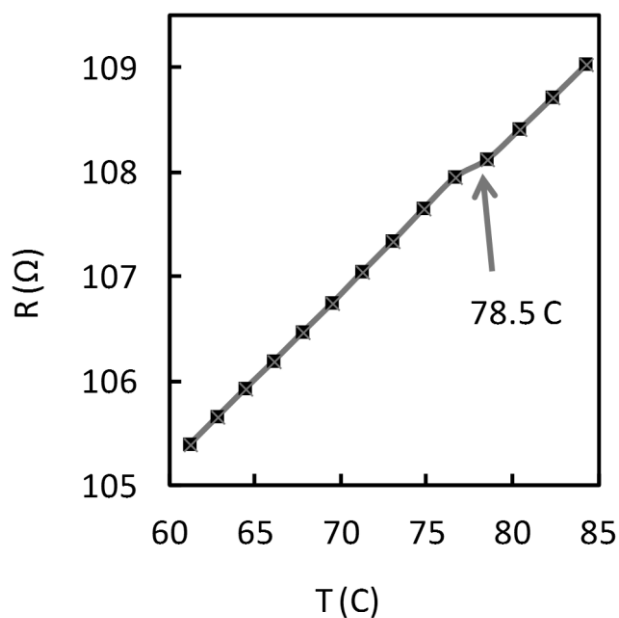


Fig 7.5 The melting temperature of naphthalene was measured with the probe. The change in resistance of the deflection sensing element on the vertical axis with temperature increase of the heating element on the horizontal axis is shown.

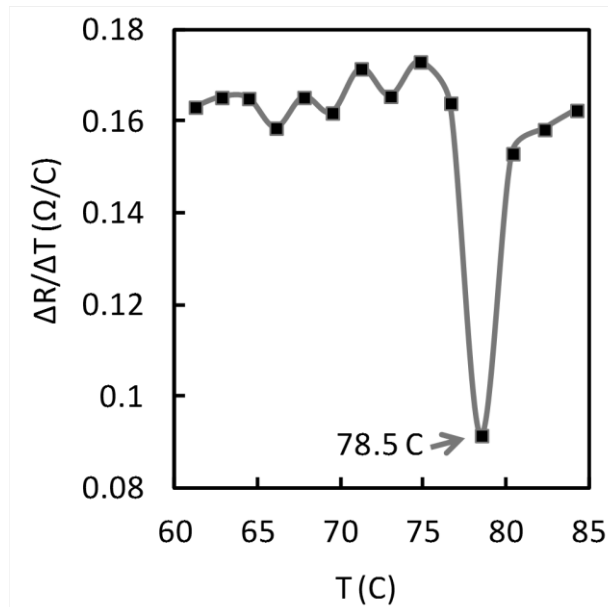


Fig. 7.6 shows the first order derivative (dR_{piezo}/dT) of the deflection sensing element on the vertical axis with temperature increase of the heating element on the horizontal axis. Near the reported melting temperature a local decrease in resistance is observed in both Fig. 7.5 and 7.6 at 78.5 °C indicating a glass transition.

7.4 Conclusions

A micromachined piezo-thermal probe that includes two monolithically integrated sensors, one for measuring the mechanical movement of the probe and another for providing localized heating, has been used eliminating the need for an AFM. An ultrathin gold film with 10 nm thickness was deposited on a silicon cantilever to form both sensing and heating elements. The change in resistance of the deflection sensing element with displacement is used to estimate the point of contact. The sensitivity of the deflection sensing element ($(\Delta R/R)/\text{deflection}$) is

0.1 ppm/ nm and its gauge factor is 3.24. The melting temperature of naphthalene is measured (with heating rates up to 25°C/sec) near 78.5 °C, which is close to the reported melting point (79-81 °C ±0.3 °C).

8

Probe array for high throughput applications¹¹

In this chapter, an array of probes with 5-10 nm gold ultrathin film sensors on silicon substrates for high throughput SPM is developed. The deflection sensitivity is 0.2 ppm/nm. Plots of the change in resistance of the sensing element with displacement are used to calibrate the probes and determine probe contact with the substrate. Topographical scans demonstrate high throughput and nanometer resolution. The heating elements are calibrated and the thermal coefficient of resistance (TCR) is 655 ppm/K. The melting temperature of a material is measured by locally heating the material with the heating element of the cantilever while monitoring the bending with the deflection sensing element. The melting point value measured with this method is in close agreement with the reported value in literature.

¹¹ Parts of this chapter were published in: A. Gaitas, P. French, "Piezo-thermal probe array for high throughput applications", *Sensors and Actuators. A: Physical* (2012)

8.1 Introduction

Using metal sensors is relatively simple to expand to a one or two dimensional probe array for higher throughput multi-location measurements overcoming AFMs throughput limitations. Higher throughput is very important in many applications ranging from semiconductor failure analysis and production applications (where entire wafers or large areas need to be examined in relatively short time), to biological applications such as cell elastography [Favre, 2011] and high throughput patch clamping. Nanofabrication and nanotechnology applications that would benefit from a higher throughput multi-probe system include nanoscale imaging, thermo-chemical patterning [Basu, 2004], and nano-CVD [Gaitas², 2013], nano-indentation, nano-patterning, and dip pen nanolithography [Zhang, 2002]. Finally, material characterization techniques that rely on AFM would benefit from faster analysis rates, simultaneous multiple location measurements, and lower costs, some examples include thermo-mechanical and mechanical analysis.

The probe arrays described in this chapter were fabricated as described in Chapter 4.4 and include a monolithic integration on each cantilever of a heating element (which can also be used for temperature sensing) and a deflection (or displacement) sensing element. Gold films of 5 nm to 10 nm thicknesses were deposited on a silicon cantilever to form both sensing elements. The probes operate without the need of an optical lever required by AFM systems to detect cantilever deflection. In addition, the probes have a very large dynamic range of tens of micron. This chapter is an expansion of chapters 5, 6 and 7.

8.2 Element characterization and probe-sample contact

The resistances of the active elements used for these measurements vary between 409Ω and 433Ω . Typically, the probe array is positioned near the sample area. The sample used for these tests is a glass slide. The sample is gradually brought closer to the array, while the probes are optically and electrically monitored to determine contact. Fig. 8.1 shows a method to determine contact by monitoring the probes optically through a high resolution microscope. As soon as the probes come in contact with the sample their reflection changes. Optical monitoring can determine contact with better than $0.5\mu\text{m}$ accuracy.

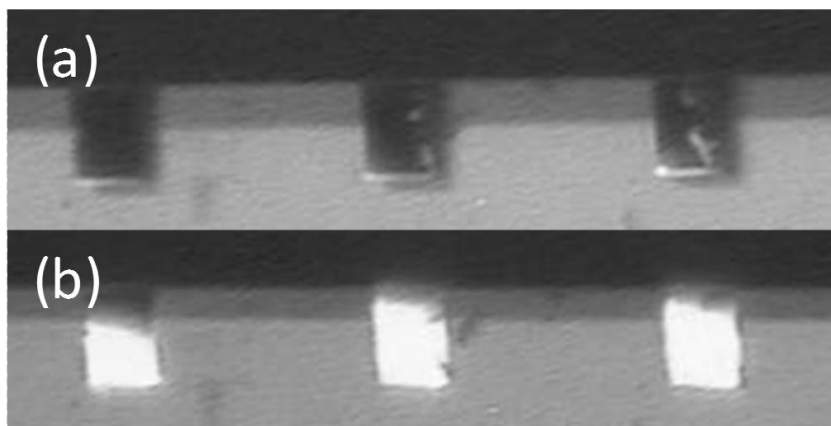


Fig. 8.1 Probes are monitored using an optical microscope to determine contact, which occurs when the reflection changes. Here, three probes are shown (a) before contact and (b) after contact.

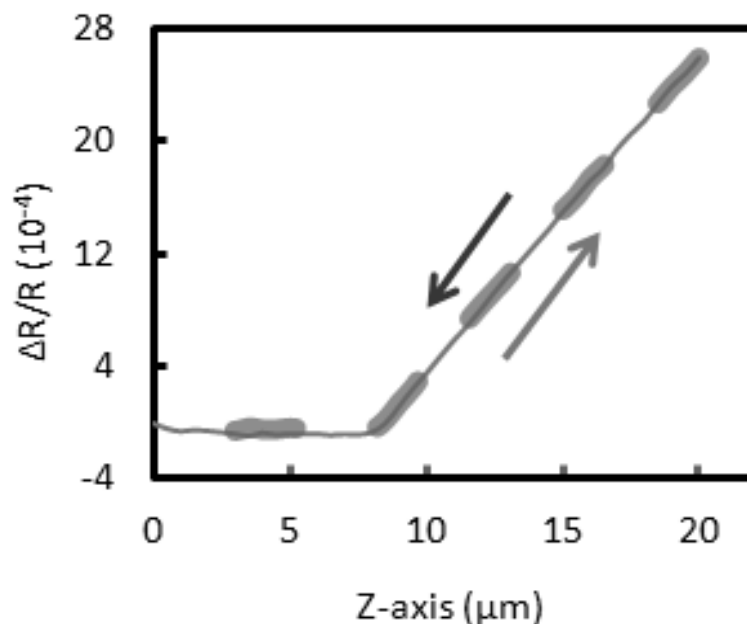


Fig. 8.2 *Electrical monitoring of probe-sample contact and cantilever characterization is done using “force-curves” of a probe on a hard substrate such as glass.*

Alternatively, each cantilever can be monitored electrically by measuring the change in the resistance of the deflection sensing element similarly to the “force-curves” generated using AFM systems. These “force-curves” can be used to determine probe-sample contact and to calibrate the probes. In Fig. 8.2 the arrows indicate the direction of the movement. The thin line represents the trace (probe and sample moving toward each other) and the thick dashed line represents the re-trace (probe and sample moving away from each other). The vertical axis is the change of the resistance of the resistor measured with a micro-ohm meter (Agilent, HP-34420A) and the horizontal axis is the Z-axis movement toward and away from the sample measured with the piezoelectric stage. From the curves, the deflection sensitivity of the probes

$((\Delta R/R)/\text{deflection})$ is calculated to be 0.2 ppm/nm. From equation 6.7 of Chapter 6 and the experimental data, the average gauge factor is calculated to be 3.16 ± 0.05 . Probes in the same array exhibit high consistency in the measured sensitivity and measurement repeatability. There is less than 2% variation in the values of the gauge factors in cantilevers of the same array.

8.3 Topographical scanning

Figure 8.3 (b) show a $10\mu\text{m}$ line scan over the top surface of a $10\mu\text{m}$ pitch square grating with $1\mu\text{m}$ height (Fig. 8.3 (a)). The line scan in Fig. 8.3 (b) is a plot of the change in deflection in μm , after converting the resistance data using the deflection sensitivity calculated above, vs. the in-plane (XY plane) movement. In Fig. 8.3 (b) the probe moved in $0.2\mu\text{m}$ steps in the X direction.

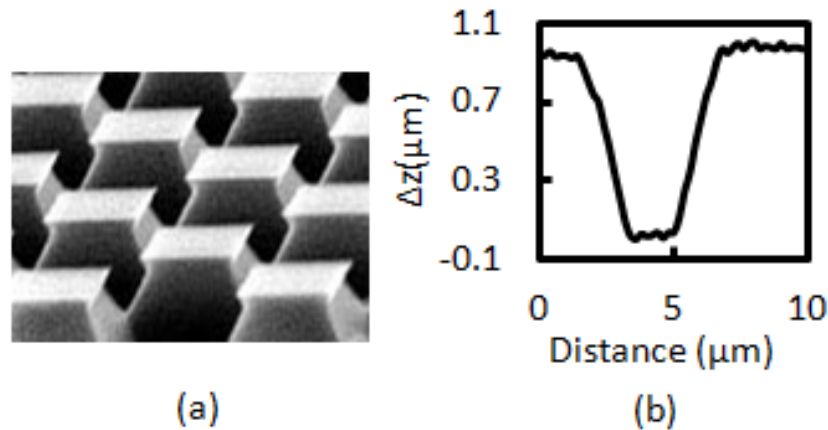


Fig. 8.3 (a) SEM of $10\mu\text{m}$ pitch square grating with $1\mu\text{m}$ height. (b) A high resolution $10\mu\text{m}$ line scan. The probe moved in $0.2\mu\text{m}$ steps in the X direction.

Eliminating the need for an optical lever is particularly useful when an array of probes is used to increase throughput. In Fig. 8.4 unprocessed data of $40\mu\text{m} \times 40\mu\text{m}$ area scans acquired by 3

different cantilever probes scanned over the 10 μm pitch square grating (Fig. 8.3 (a)) are shown. The probes moved in 1 μm steps in the X direction and 1 μm steps in the Y direction. Indicative line scans for each probe are shown. The scanning speed was 5 $\mu\text{m/s}$. The data were acquired with a multimeter.

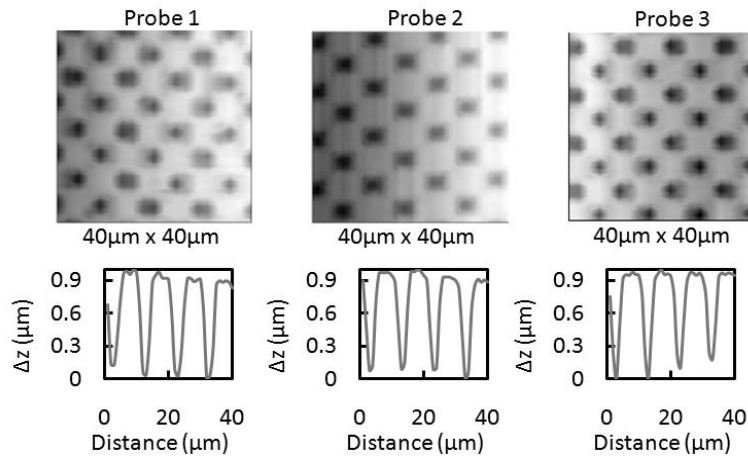
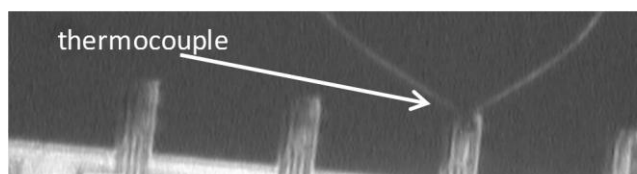


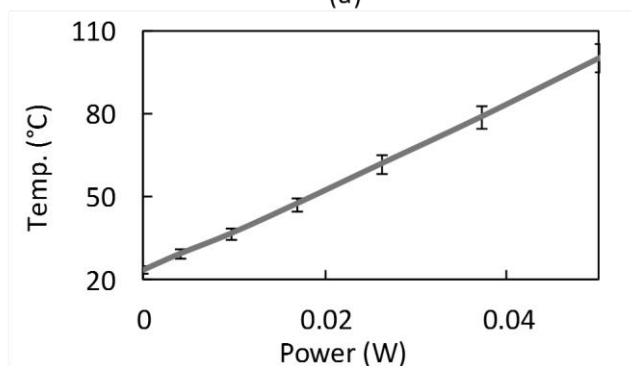
Fig. 8.4 A 40 μm x 40 μm area scan acquired by 3 different probes scanned over the 10 μm pitch square grating.

8.4 Thermo-mechanical applications

The heater is independently calibrated using a 12 μm size thermocouple (Omega, CHAL-0005) that is brought into contact with the heating element as shown in 8.5 (a). A variable power supply (Keithley 2400) is used to increase the power through the heating element while monitoring the temperature with the thermocouple. Fig. 8.5 (b) shows the near linear relationship of the power through the heating element with temperature. Fig. 8.5 (b) is used to derive the temperature from a known value of power through the heating element. From this measurement the TCR of the heater was calculated to be approximately 655ppm/K.



(a)



(b)

Fig. 8.5 (a) An optical image of a $12\ \mu\text{m}$ thermocouple in contact with one of the probe tips of an array. The thermocouple is used to calibrate each heater. Each heater is heated gradually, while the current through the probe (I), the voltage (V) and the temperature at the tip are recorded. (b) The calibration curve of power vs. temperature from the measured data is linear. From the resistance and temperature data the TCR is estimated to be approximately $655\ \text{ppm/K}$.

The melting temperature of naphthalene C_{10}H_8 (Sigma-Aldrich, Inc., 01422-250MG, Melting Point Standard) with a melting point between $79\text{-}81\ \text{°C}$ ($\pm 0.3\ \text{°C}$) is measured with the piezo-thermal probe in a similar way to chapter 7. A variable power supply is used to increase the power through the heating element of each probe, while the change in resistance of the deflection sensing element of each probe is directly measured using a micro-ohm meter. The calibration curve of Fig. 8.5 (b) is used to convert

power to the corresponding temperature. Fig. 8.6 shows the first order derivative ($\Delta R/\Delta T$) of the deflection sensing element on the vertical axis with temperature increase of the heating element on the horizontal axis. Near the reported melting temperature a local decrease in resistance is observed at 79.7 °C. The local decrease in resistance is interpreted as a movement of the probe toward the sample, an indent toward the sample, caused from the melting.

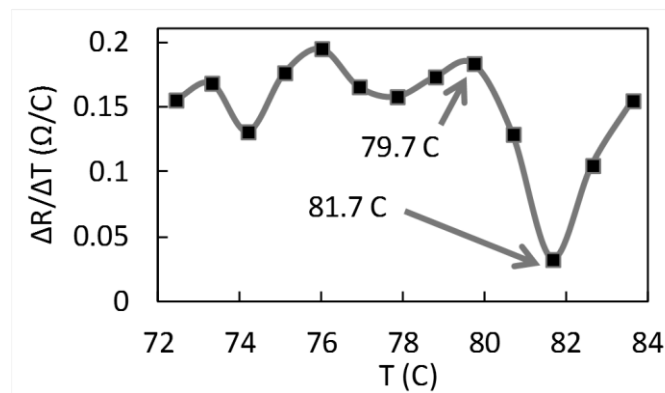


Fig. 8.6 The first order derivative of change in resistance with respect to temperature vs. temperature is shown with knee point at 79.7 C. The X-axis represents the temperature of the heater and the Y-axis the change in resistance with temperature of the deflection sensing element.

8.5 Conclusions

An array of probes with 5 nm-10 nm gold ultrathin film sensors on silicon substrates for high throughput scanning probe microscopy has been successfully fabricated continuing the previous work. The deflection sensitivity is 0.2 ppm/nm. Plots of the change in resistance with displacement are used to calibrate the probes' deflection element, while plots of change in power and resistance with temperature are used to calibrate the heating element. Topographical scans demonstrate high throughput and nanometer resolution. Melting point measurements demonstrate the ability to conduct high throughput material characterization measuring two parameters of each individual cantilever in an array simultaneously, namely temperature and deflection. Sensitivity and compliance can be further improved with the use of polymer, instead of silicon, as a structural material for the cantilevers. Sensitivity and gauge factors can be further improved using alternative sensing elements instead of gold such as thin films of other metals and metal oxides. These innovations would allow for a wealth of new nanoscale high throughput applications including integrated circuit hot spot detection, material characterization, nano-indentation, dip pen nanolithography, cellular imaging, multiple single cell elastography, and patch clamping.

9

Tip-based chemical vapor deposition¹²

Manufacturing of individual nanostructures and devices with ability to manipulate their location and shape is a central goal in nanofabrication. In this chapter a moving nano-heater directs a chemical vapor deposition reaction (nano-CVD) demonstrating a tip-based nanofabrication (TBN) method. Localized nano-CVD of copper (Cu) and copper oxide (CuO) on a silicon (Si) and silicon oxide (SiO₂) substrate from gasses is demonstrated. The gasses used are sublimated copper acetylacetonate (Cu(acac)₂), argon (Ar), and oxygen (O₂). This technique is applicable to other materials.

¹² Parts of this chapter were published in: A. Gaitas, "Tip-based chemical vapor deposition with a scanning nano-heater", Applied Physics Letters (2013)

9.1 Introduction

Scanning thermal probes [Williams, 1986], developed for atomic force microscopy (AFM) [Binnig, 1986], can be used as nano-heaters to create localized manufacturing environments. Existing nanomanufacturing technologies have several limitations such as inability to control the manufacturing process in real time and uniformly grow a material [Schofield, 2012; Malshe, 2010]. AFM tips may provide a nanomanufacturing solution, as a result TBN has become a viable alternative for the next generation nanofabrication [Schofield, 2012]. There are a number of TBN platforms, ever since IBM's Millipede [Vettiger, 2000] that utilized nano-heater AFM arrays. These platforms include dip pen nanolithography [Piner, 1999], nanoembossing [Kalpakjian, 2006], tip-based nano-electromachining [Kunieda, 2005], nano-electrochemical machining, deposition and transformation [Wu, 2007], and tip-based laser assisted nanomanufacturing [Gorbunov, 1994]. There have been efforts to thermo-chemically pattern organic materials [Basu, 2004; Fenwick, 2009] and to thermally reduce graphene oxide [Wei, 2010] using nano-heaters. Other efforts have concentrated on 2-dimensional precision patterning on Si [Randall, 2010]. However, TBN has mainly concentrated on chemically, mechanically, or thermally altering substrates in 2-dimensions or depositing liquid chemical reagents [Malshe, 2010].

In this chapter a moving nano-heater locally heats specific areas on a substrate to induce a chemical reaction from precursor and reaction gasses for the deposition of materials. More specifically $\text{Cu}(\text{acac})_2$ and O_2 were used resulting in the deposition of Cu and CuO at desired locations. The tip-contact area has a diameter of sub-micron lengths, heating the substrate over a diameter that is similar to the tip. The tip is heated resistively and the nano-heaters

are designed so that most of the heating occurs at the contact area [Gaitas, 2011^B; Gaitas, 2011^c; Gaitas, 2012].

9.2 Device and experimental set-up

The nano-heater includes a metal resistor that acts as a heating element, made of 10 nm Ti and 100 nm Ir film, with nominal resistance of 8.15 Ω , deposited on a Si and SiO₂ cantilever. The fabrication of the nano-heater is described in Chapter 4 [Gaitas, 2011^B; Gaitas, 2011^c; Gaitas, 2012]. The nano-heater comprises of a 20 μm tall tip with a <500 nm tip diameter and a passivation layer covering the cantilever and the tip made of a 100 nm Si₃N₄ layer. The device is annealed at 900 °C for two hours. It is operated at 288 mW by passing current through the resistor, which corresponds to a temperature of approximately 298.8 °C at the tip. The nano-heater is calibrated using a thermocouple as described in Chapters 7 and 8 [Gaitas, 2011^B].

A custom made scanning system, illustrated in Fig. 9.1 (a), resides inside a glass chamber. The tip is scanned using an XYZ piezo-electric stage (Tritor 100 XYZ piezo-positioner from Piezosystem Jena) with 0.2 nm resolution and motion range of 100 μm in each direction. A motorized stage (KT-LS28-MV from Zaber) is used to align the probe tip to the desirable scanning region on the sample. An optical microscope is used to monitor the probe tip and the sample movement. Four connectors are fitted on the sidewall of the chamber, one for gas inlet, one for gas outlet, one for electrical connection feed-through, and one for pressure monitoring. The inlet is connected to tubes that connect to flow-meters that in turn connect to gas cylinders. The outlet is connected to a pump. The sample holder rests on top of the piezo-positioner and includes a flat heater (Omega) attached on one side and a substrate on the other. The thermal probes are heated with a sourcemeter (Keithley

2400). Contact is determined by monitoring the tip optically through a high resolution microscope as described in Chapters 6, 7, and 8 [Gaitas, 2012].

9.3 Experimental results and discussion

A low-pressure metal oxide CVD process is used to grow Cu and CuO from Cu(acac)₂ (C₁₀H₁₄CuO₄). The chemical reaction and conditions such as pressure and temperature are described in Condorelli, 1994 [Condorelli, 1994] and Condorelli, 1995 [Condorelli, 1995]. Ar and O₂ are introduced under constant flow rates of 200 sccm for O₂ and 30 sccm for Ar, respectively. The total pressure is held between 4 Torr and 5 Torr. Cu(acac)₂ was obtained in powder form (Copper(II) acetylacetonate with product number 514365 (CAS Number 13395-16-9) was purchased from Sigma Aldrich) and placed on the flat heater inside the chamber in close proximity to a Si/SiO₂ diced wafer substrate. Cu(acac)₂ is then heated to a sublimation temperature of 130 °C. The nano-heater is brought in contact with the substrate and heated to approximately 298.8 °C. The piezo-electric stage is programmed to move a total area of 70 μm by 70 μm. The X-axis is set to stop every 5 μm for 10 seconds and the Y-axis is programmed to move by 5 μm following a full 70 μm X-axis movement.

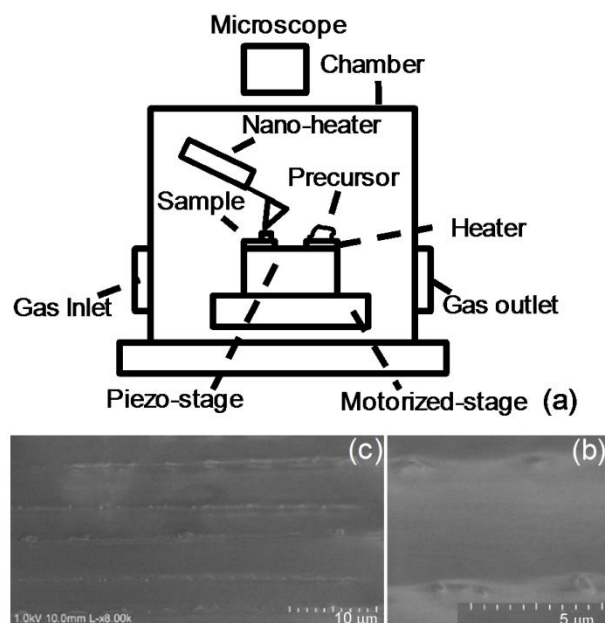


Fig. 9.1. Nano-CVD using a nano-heater. (a) Schematic of the setup. (b) SEM image of the fabricated lines is in agreement with the tip's movement. The tip was stopped for 10 seconds every 5 μm in the X-direction and moved by 5 μm in the Y-direction. The Cu and CuO lines can be clearly seen. (c) A higher magnification SEM image showing sub-micron structures repeated every 5 μm .

Scanning electron microscope (SEM) (Hitachi SU8000) images and energy-dispersive X-ray spectroscopy (EDS) (QUANTAX by Bruker) chemical analysis demonstrate that Cu and CuO features are consistently obtained by scanning the nano-heater over the substrate (Fig. 9.1 and Fig. 9.2). The SEM images (Fig. 9.1 (b) and 9.1 (c)) demonstrate that CVD growth occurred at the areas where the probe tip was programmed to stop for 10 seconds. There is some growth on the line of movement because the tip is kept at an elevated temperature even while in motion. Chemical analysis in Fig. 9.2 (b) and 9.2 (c), over the area shown in Fig. 9.2 (a),

confirms the presence of copper and carbon in selected regions where the heated tip is scanned and mostly accumulated at the spots that the tip stopped for 10 seconds.

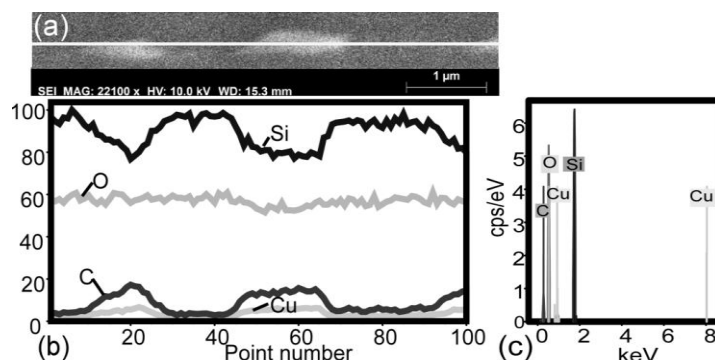


Fig. 9.2. Chemical analysis of nano-CVD. (a) Prior to performing the EDS line scan, an SEM image of the sample is acquired. A line marks the part to be analyzed. (b) Line scans of one dimensional normalized concentration profiles to determine the chemical elements demonstrate that C and Cu concentrate in the regions that the features are observed, while Si is mostly concentrated in the areas where Cu and C are not present. (c) The average quantitative spectrum analysis for the whole scan line identifies and measures the individual elements' concentrations over the range of the scan line. The elements that are present include Cu, C, Si, and O₂.

9.4 Conclusions

In this preliminary study heated scanning tips were used to fabricate nanostructures. Several materials can also be grown on the substrate eliminating the need for multiple fabrication steps. Localization and control of heat allows the user to change conditions at the level of individual nanostructures enabling

research in the thermodynamics and kinetics of growth. Applications are found in semiconductor and nano-device manufacturing, functionalizing surfaces and electrically connecting nanotubes and other nanostructures by growing electrically conductive lines. Future experiments will include controlling growth by intermittent heating and cooling, vertical growth, applying of an electric field between the tip and the substrate, exploration of additional chemistries, and high throughput growth using multi-probe arrays.

10

A Polymer micro-cantilever for explosive detection¹³

In this chapter polyimide microcantilevers with metal sensors are used for explosive vapor detection in an attempt to transfer many of the concepts of the previous chapter to polyimide cantilevers. These cantilevers are studied and used in applications of industrial interest. The fabrication of this cantilever has been described in detail in chapter 4.6. Tetrathiafulvalene-functionalized calix[4]pyrrole¹⁴, a colorimetric receptor, was combined with a polyimide micro-cantilever, that includes a 10 nm gold mechanical stress sensing element. The resulting system is capable of detecting 10 ppb trinitrobenzene vapor. This represents a 30-fold improvement relative to the receptor in halogenated solvents, suggesting that this approach can provide a solution to translating the chemical response of colorimetric chemosensors into practical devices.

¹³ Parts of this chapter were published in: W. Zhu, J. S. Park, J. L. Sessler, A. Gaitas, "A Colorimetric Receptor Combined With A Microcantilever Sensor For Explosive Vapor Detection", Applied Physics Letters (2011)

¹⁴ This coating material and its description were provided by Prof. Sessler's group from the University of Texas- Austin. This research was conducted in collaboration with Prof. Sessler and Dr. Weibin Zhu.

10.1 Introduction

In the past decade, there has been considerable work in the area of microfabricated chemical sensors and systems for trace explosives detection [Moore 2004]. These microsystems can potentially be used in low-cost and handheld explosive detection devices. Several MEMS technologies that are suitable for a portable trace explosive systems have emerged: (1) Micro gas chromatography (μ GC) systems provide comprehensive analysis of sample mixtures by separating materials in a micro column and then detecting their concentrations separately. But the cost of fabricating a μ GC is relatively high as the components of the μ GC and integrated circuits are complicated and the fabrication process may not be fully CMOS-compatible. The packaging of the system is also a challenge because there are many microfabricated components and fluid channels need to be connected together. Furthermore, the detection time of the μ GC is limited by the separation time (several minutes). Finally, the separation column is constructed with a long micromachined channel. Explosives such as TNT with a very low concentration and good adhesion to many materials can attach to the wall in the column, and thus affect the detection of the transducer in the downstream. (2) A chemiresistor changes resistance when exposed to a gas or vapor but suffers from many issues such as interference from ambient (e.g. temperature, humidity, etc.) and selectivity. (3) An explosive detector that can detect the deflagration of tiny amounts of explosive adsorbed on a cantilever surface was recently developed [Pinnaduwa, 2004]. A cantilever coated with a transition metal is heated to 570°C and reacts with trinitrotoluene (TNT). The selectivity and high power consumption could be potential challenges for this device. (4) Film based sensor arrays are commonly microfabricated cantilevers that are coated with different receptor materials. When the receptor materials selectively adsorb the target chemicals, the mechanical characteristics of the cantilevers such as bending stress

mass and resonant frequency will change and can be detected with various methods. This technique can provide simultaneous rapid detection for various explosives at the fraction of the cost. Si and Si₃N₄ are the most common materials for cantilevers. The sensitivity and selectivity partially rely on the properties of the cantilever material (Young's modulus) and highly depends on the chemical properties of the coated materials (such as sensitivity and selectivity). In addition, cantilever based detection is very promising due to its inherently high sensitivity and ease of fabrication and integration. The sensors are simple enough to be fabricated in a low-cost process and consequently have great potential to be implemented to a wireless explosive sensing network for explosive monitoring.

In cantilever based sensing, two different readout methods can be applied: static (bending) and dynamic (resonant) methods. In static method, the deflection and the surface strain of the cantilever are measured when the cantilever is bent. The most commonly employed method to measure the deflection is based on the optical leverage principle. This method is accurate to a few angstroms, but it is bulky and laser alignment is cumbersome. For this reason, the optical method is unsuitable for use with multi-sensor arrays and handheld systems. Capacitive detection of bending is another popular method, but has the disadvantages of a small dynamic range and cross-talk between different devices. Piezoresistive readout mechanism is a prevalent method to detect the surface strain on the cantilever by measuring the resistance change of the piezoresistive sensors due to surface stress generated by the interaction between a chemical or biochemical analyte and the cantilever surface. This method has several advantages including high sensitivity, good linearity, ease of fabrication and calibration, and good scalability to a multi-sensor array. Additionally, the piezoresistive measurement can be applied in different environments including in air and liquids, at low and high temperatures (-35° C – 200 °C) [Wu, 2008; Li, 2000], and does not

require an ultraclean environment. All these features make piezoresistive microcantilevers an excellent platform for inexpensive and portable trace detection of explosives. SU-8 cantilevers for chemical and biochemical detection were reported in prior art [Johansson, 2005]. These polymer cantilevers showed detection limits in the ppb range with self assembled monolayer films. Conventional silicon cantilevers using dynamic readout were previously reported [Pinnaduwege, 2005]. These devices showed detection limits in the tens of ppt.

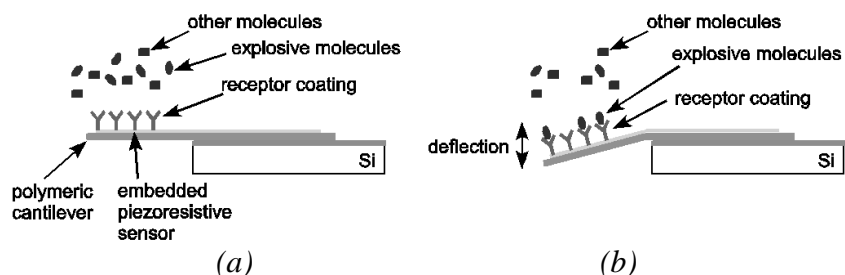


Fig. 10.1 Schematic diagram of the polymeric nano-cantilever coated with explosive receptor: (a) before absorption of explosive molecules; (b) after absorption of explosive molecules.

In this chapter an inexpensive microcantilever sensor array for explosives detection will be discussed. This sensor can identify an analyte by changes in resistance of the cantilever because of analyte absorption or binding to the receptor materials (Fig. 10.1). The sensitivities and detection limits of the microcantilever array are significantly improved by using ultracompliant polymers coated with TTF-calix[4]pyrrole that shows high degree of sensitivity and selectivity to different explosives. Ultrathin metallic (gold) piezoresistive sensors are embedded into the cantilevers to enable both static and dynamic measurements. Compared to μ GC systems [Zellers, 2007] and film based sensor arrays [Pearce, 2006; Guntherodt, 2000], the polymeric cantilever sensor has several advantages: a) The cantilever structure is simple

enough to be fabricated in a low-cost process and is particularly suitable for a multiple probe array for portable applications. b) The cantilever has high sensitivity and high linearity. d) The coating materials of the cantilever (supramolecular receptors) [Nielsen, 2004; Park, 2010] are designed to be selective for highly electron deficient nitro-based explosives, including those found in improvised explosive devices (IEDs). Therefore, this supramolecular-based approach involves targeting the explosives as a molecular whole.

10.2 Coating for explosive adsorption

One of the rationales for pursuing cantilever-based explosive monitoring systems comes from the recognized difficulties associated with detecting IEDs. IEDs generally consist of mixtures of chemical oxidants and reductants, often in the same molecule that undergoes highly exothermic decomposition to generate gaseous products. Explosives are notoriously difficult to detect because of their chemical and physical properties including low vapor pressure and susceptibility to thermal degradation. Among the various explosive materials, nitro-aromatic, aliphatic, and cyclic compounds represent critical targets for detection because they are common constituents in military and industrial explosives, such as TNT, PA, Tetryl, RDX, HMX, PETN, and NG. Combinations of TNT, RDX, PETN, and HMX with various organic compounds are often found in IEDs as well as in military explosives. These explosives contain multiple nitro groups, embedded within an aromatic, aliphatic, or cyclic organic framework. As a result, this functional group has been heavily exploited and targeted by most chemosensors reported to date. As described below, different from these strategies, the supramolecular-based approach targets the explosive as a molecular whole.

Recently, considerable effort has been dedicated to the production of molecular receptors that can function as so-called chemosensors for nitroaromatic explosives [Stepien, 2007; Jiang, 2008; Ercag, 2009; Lee, 2010]. Within this context, colorimetric systems, agents that signal the presence of a nitroaromatic analyte via a color change, have a certain appeal [Jiang, 2008; Ercag, 2009; Lee, 2010; Park, 2010]. Their ease of use and their ability to function in the absence of any supporting instrumentation could make them applicable in certain situations where a qualitative yes/no indication involving the presence or absence of a targeted explosive is required. However, in spite of their potential advantages, the colorimetric sensors for nitroaromatic explosives reported to date suffer from disadvantages. Prime among these is low sensitivity and difficulties with translating the colorimetric response seen in solution (where most function well) into the gas phase. This has made them less than ideal for stand-off detection of nitroaromatic explosive vapors. To address this deficiency, a well-studied colorimetric sensor that responds to trinitrobenzene (TNB) in organic media, namely the thieno-fused, tetrathiafulvalene-functionalized calix[4]pyrrole (TTF-C4P; cf. scheme shown in Fig.10.2), was combined with the polyimide cantilever sensor. This receptor has previously been demonstrated to bind TNB in organic solution [Park, 2010]. However, although superior to earlier TTF-functionalized calixpyrrole receptors, is capable of detecting TNB in solution with a limit of detection (LOD) of ca. 0.3 ppm in halogenated solvents. This receptor was incorporated on a cantilever sensor in the hopes of improving the sensitivity and creating a device capable detecting TNB vapors. The resulting sensor system is capable of detecting TNB in commercially available gas mixtures containing TNB vapor at the 10 ppb level; this represents considerable operational improvement in the sensitivity compared to what is seen in bulk organic media and leads to suggest that the present approach could provide a general solution to the long-standing problem of translating the chemical response of colorimetric chemosensors into practical devices.

Supramolecular receptors are designed to be selective for highly electron deficient nitro-based explosives, including those found in IEDs. A TTF-substituted calixpyrrole, is used as a receptor to affect the selective binding of a specific substrate (e.g., TNT, RDX, etc.).

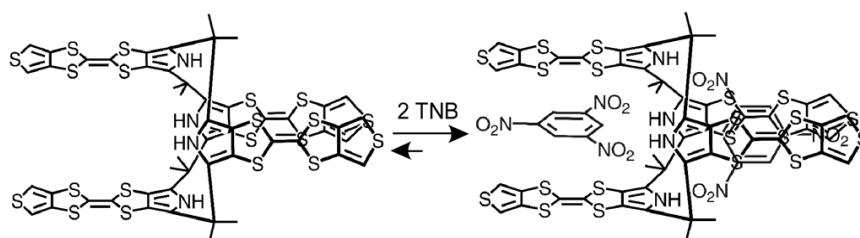


Fig. 10.2 Molecular structure of thieno-TTF-calix[4]pyrrole (TTF-C4P) and its TNB binding mode observed in organic solutions¹⁵.

Tetrathiafulvalene functionalized calix[4]pyrrole (TTF-calix[4]pyrrole), **4** (Receptor **4**) [Park, 2010], is supplied by Prof. Sessler. Receptor **4**, a second generation prototype, possesses a number of features that make it attractive for explosive detection. First, it displays a high level of sensitivity, one that is especially remarkable given the neutral nature of the receptor-substrate recognition events involved. Second, a high degree of specificity for electron deficient species is observed as expected. Little evidence of “false positives” has been seen when TNB or TNT is replaced by toluene or mono-nitrotoluene. Third, strong binding is perceived even in the presence of water and other polar solvents.

¹⁵ Figure and section provided by Prof. Sessler.

10.3 Characterization of the cantilever sensor

The displacement sensitivity ($\Delta R/R/\text{displacement}$) of the cantilever was calibrated by measuring the response of the sensing element when the cantilever is deflected by a piezoelectric stage (PiezoJena, Tritor 100). A multimeter (Agilent, 34401A) was used to determine the resistance via the four point measurement method. Here, the free end of the cantilever was in contact with the piezoelectric stage. The stage is used to generate a displacement at the tip of the cantilever and measure the response of the gold sensor. The minimum displacement the piezoactuator is 1 nm. In this experiment, the stage contacted with the tip of the cantilever during the measurement. A microscope is used to observe the contact between the tip and the stage as well as the deflection during the experiment. The measured displacement sensitivity proved to be $1.1 \times 10^{-6}/\text{nm}$ ($0.11 \text{ } \%/ \mu\text{m}$), and the minimum detectable displacement is 1 nm, while the corresponding gauge factor for the 10 nm thin film gold was found to be about 3, which is higher than the gauge factor of bulk gold.

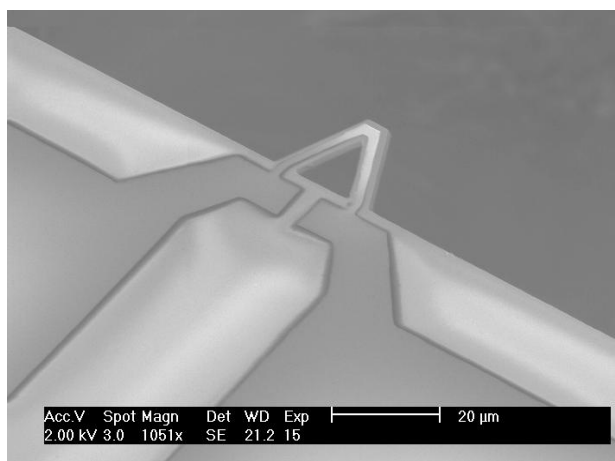


Fig. 10.3 SEM photos of the polymeric nano-cantilever without coating.

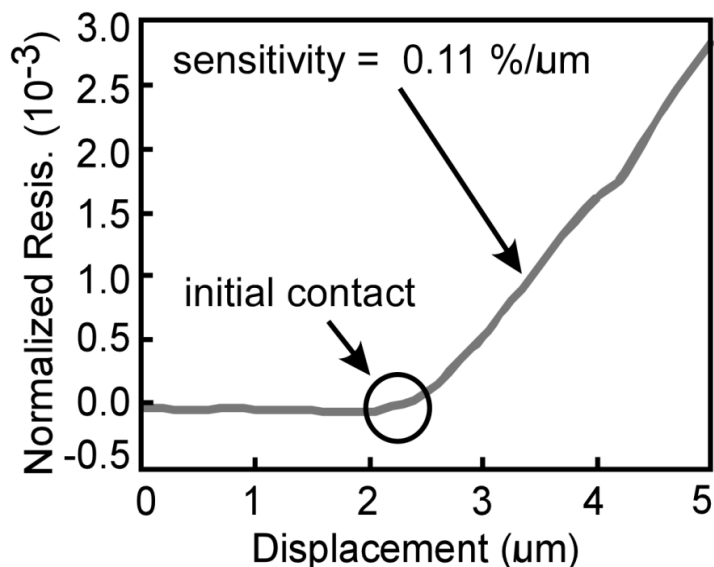


Fig. 10.4. Response of the V-shape polyimide cantilever with displacement.

To provide a basis for analyzing the systems, a simplified FEM model (modified from a model developed by Ricci et al. [Ricci, 2006]) for surface stress was developed, this has been described in detail in chapter 4. The change of surface strain due to the adsorption of the molecules on the cantilever is attributed to various interactions including Coulomb repulsion between adsorbed molecules [Godin, 2010]. The specific correlation between the average surface strain and the absorbed TNB vapor is unclear and requires further characterization.

10.4 Explosive detection

TTF-C4P was used as a receptor for the cantilevers of this study. It has been demonstrated previously that TTF-C4P binds to nitroaromatic TNB [Park, 2010]. This receptor also displays a high

inherent specificity for flat, electron deficient species, such as TNB. In fact, little evidence of “false positives” has been seen when less highly substituted nitroaromatic compounds were used instead of TNB. Further, TNB binding is seen even in the presence of water and other polar solvents. Therefore, this particular receptor is useful in developing a working sensor device. Driven in part by the fact that while, TTF-C4P will respond to TNB in solution, the actual response is not that strong; incorporating the sensor into a device product leads to enhanced sensitivity.

To conduct measurements in the presence of vapor TNB two identical cantilevers are used to form a Wheatstone bridge circuit, shown in Fig. 10.5 (a). One side of the sensing cantilever is coated with a TTF-C4P, while the reference cantilever is left uncoated. The supply voltage of the bridge circuit is set to 0.05 V to ensure low current values through the cantilever and reduce Joule heating effects. The data is recorded with a data acquisition system in real time without amplification. The noise of the readout is about 2 μV . A data acquisition system is used to record the voltage output from an Agilent 34401A multimeter. Small temperature drifts after the Wheatstone bridge is balanced (Fig. 10.5 (a)) are attributed to ambient temperature fluctuations and differences in the nominal resistance between the reference and the sensing cantilevers.

TNB solid is placed in a Tedlar® bag and 99% nitrogen is blown into the bag. The TNB solid can evaporate to the nitrogen gas and eventually saturates. The saturated vapor employed contains TNB at 6.44×10^{-6} Torr and 25 °C. The equivalent concentration of TNB in the gas mixture is 10 ppb. When the Wheatstone bridge is balanced and the system is stable, the TNB gas mixture is slowly injected into the chamber which originally filled with air. Fig. 10.5 (b) shows the response of the V-shape polyimide cantilever when a 20 mL TNB gas mixture is slowly injected in the chamber, which contains the cantilever. An initial readout response occurs within 5 seconds following TNB injection. The differential voltage

output peaks at $13 \mu\text{V}$ after several minutes. The corresponding surface stress calculated from the FEM model is approximately 1.4 N/m (tensile). The response to peak value can be further improved by reducing the dead volume. Additional experiments reveal that the cantilever does not respond to air or acetone-saturated vapors.

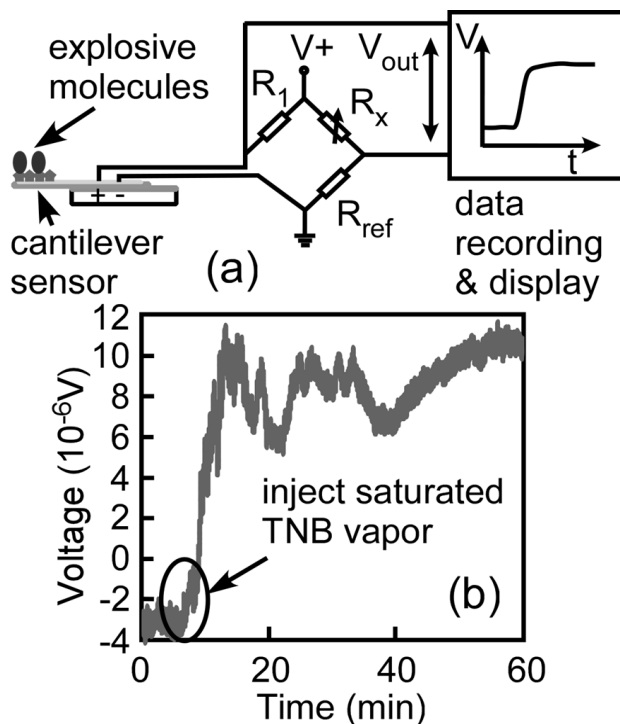


Fig.10.5 (a) Schematic diagram of the experimental setup. (b) Graph of the response of the V-shape polyimide cantilever when exposed to TNB. The vertical axis corresponds to the change in voltage output and the horizontal axis represents time in minutes.

The response is relatively slow because TNB molecules take a long time to diffuse to the cantilever, which has a length of $20 \mu\text{m}$ and width of $5 \mu\text{m}$ and is about 1 cm away from the inlet, and fully react with the receptor on the cantilever. The preliminary

experimental results shown in this section clearly demonstrate the capability of the polymer cantilever to detect explosive vapor at low concentrations. Although the response time is relatively slow (in 10 min. range), this can be further improved by a better packaging of the device to allow for a much smaller dead volume, and thus much smaller diffusion time for the gas to reach the device. Amplifiers and filters can be used in the readout circuit to increase the magnitude of the signal and improve the signal to noise ratio.

A TNB gas vapor at a concentration of 10 ppb represents an improvement in the detection limit of at least 30-fold compared to the ca. 0.3 ppm level achievable when TTF-C4P is used as a bulk receptor in organic solution.

10.5 Conclusions

A polyimide microcantilever with a thin film gold sensing element for the stress-based sensing of molecular analytes has been developed. The displacement sensitivity of this device is 1.1×10^{-6} /nm. The potential utility of the device for explosive detection was explored further by coating the cantilever with TTF-C4P, a colorimetric receptor, to detect TNB vapor at 10 ppb level. It is important to note that this concentration is set by the vapor pressure of TNB, and is not the actual detection limit of the device, which is expected to be much lower. Nevertheless, even at this concentration, this new setup provides a marked improvement on the detection limit (low ppm level) seen for organic solutions containing TTF-C4P. The system can be used for the detection of other nitroaromatic explosives, including 2,4,6-trinitrotoluene (TNT), by using a modified TTF-C4P receptor with improved sensitivity. The present results leads to suggest that the present approach can provide a solution to the problem of translating the chemical response of colorimetric chemosensors into practical devices.

11

Thin metal microbolometers for SThM¹⁶

Metal microbolometers, used in scanning thermal microscopy, were microfabricated from <20 nm titanium and tungsten thin films on SiO₂/Si₃N₄/SiO₂ cantilevers and on SiO₂/Si wafers. These thin films are near the metal-insulator transition regime such that as the film thickness decreases – the resistance increases and the current-voltage characteristics cross over from sublinear to superlinear. In addition, the temperature coefficient of resistance transitions from positive to negative before it plateaus at a negative value. Thin titanium and tungsten films exhibit negative temperature coefficient of resistance as high as - 0.0067/K and - 0.0095/K respectively, which is higher than that of bulk titanium and tungsten films.

¹⁶ Parts of this chapter were published in: A. Gaitas, W. Zhu, N. Gulari, E. Covington, C. Kurdak, “Characterization of Room Temperature Metal Microbolometers near the Metal-Insulator Transition Regime for Scanning Thermal Microscopy,” Applied Physics Letters (2009)

11.1 Introduction

Uncooled microbolometers are currently used in the manufacture of highly specialized thermal imaging applications such as night vision and scanning thermal microscopy (S_{Th}M) [Williams, 1986; Li, 2003; Majumdar, 1999]. In order to operate effectively, microbolometers must have a high temperature coefficient of resistance (TCR) and low noise characteristics. In addition, the materials used to manufacture microbolometers must be inexpensive and compatible with current CMOS processes. These are the primary conditions that have to be met as part of the continuing effort to develop even smaller, better performing microbolometers that weigh less and consume less power.

To date, various materials have been used to fabricate microbolometers. Polycrystalline and amorphous silicon have a high temperature coefficient of resistance (up to 0.05/K) but exhibit adverse noise characteristics [Hull, 1999; Eminoglu, 2003; Henini, 2002]. Vanadium oxide, on the other hand, has a TCR of approximately 0.05 /K and a superior noise equivalent temperature difference (NETD). However, vanadium oxide introduces a significant number of deposition problems [Henini, 2002; Ryu, 2008; Wood, 1993]. Thin film metallic microbolometers, in contrast, have very low noise characteristics in addition to a low TCR (0.005/K) [Henini, 2002; Block, 1973].

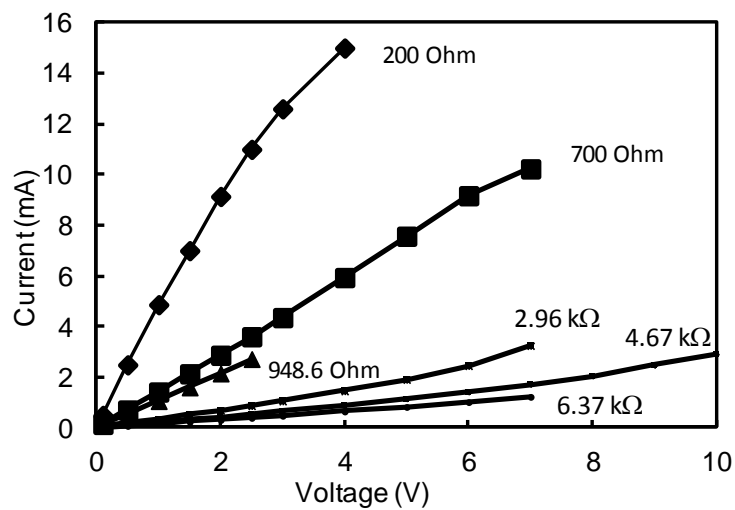
Two types of S_{Th}M microbolometers have shown considerable promise: Doped silicon microbolometers that are integrated into single-crystal silicon cantilevers [Chui, 1998; Lee, 2006], and metallic microbolometers with a TCR of around 0.0029/K [Li, 2000]. Metallic microbolometers enable the use of alternative substrate materials (such as polymers), that tend to exhibit higher compliance properties and improved thermal isolation for better temperature resolution.

The electrical properties of granular metals vary as the composition of a metal and non-metal mixture changes [Adkins, 1987]. Metal deposition goes through four phases before it starts behaving like a bulk film: nucleation, island formation, formation of island networks, and formation of continuous (but porous) film [Nowroozi-Esfahani, 1990; Chopra, 1979; Matthews, 1983; Neugebauer, 1962]. The first three phases are considered discontinuous. Typically, island films have negative TCRs while porous films have a positive TCR [Nowroozi-Esfahani, 1990; Chopra, 1979; Esfahani, 1992; Morris, 1977; Wetzig, 2006]. However, the TCR for porous films is lower than that of a thick, bulk film. It is well established that there exists a metal-insulator or a superconductor-insulator transition as a function of film thickness for metal films at cryogenic temperatures. It is interesting to note that this transition typically occurs for films with a resistance on the order of quantum resistance. Titanium films and tungsten films that are close to the metal-insulator transition (MIT) regime have been evaluated. However, instead of evaluating their cryogenic transport properties, the focus has been on their operation as thin film microbolometers (at room temperature) and on quantifying the relationship between TCR, resistance, and film thickness.

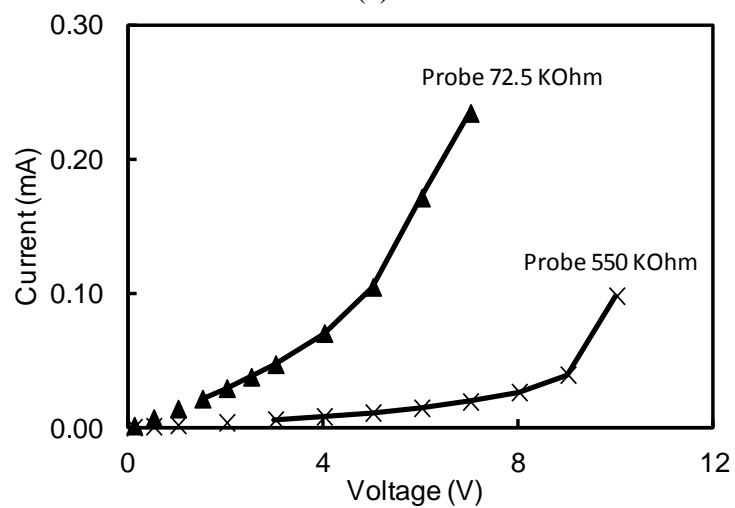
An ultrathin film (< 20 nm) titanium microbolometer which is integrated onto a $\text{SiO}_2/\text{Si}_3\text{N}_4/\text{SiO}_2$ (ONO) cantilever with a Si/SiO_2 tip intended for scanning thermal microscopy has been developed as described in chapter 4.5. Wafers with different thicknesses of titanium and tungsten were also prepared and tested. The morphology of these metal thin films (discontinuous form versus continuous form) [Esfahani, 1992] is revealed by measuring their electrical properties. I-V and TCR measurements, and a scan using these microbolometers are presented.

11.2 Measurements and results of titanium thin films

I-V measurements were performed on a probe station. The I-V characteristics of resistors on SiO₂/Si wafers with two terminal Ohmic resistances between 200 Ω to 6.37 k Ω and bolometer probes with two terminal Ohmic resistances between 72.5 k Ω and 550 k Ω are illustrated in Fig. 11.1. The I-V curves exhibit a sub-linear behavior at two-terminal Ohmic resistance values below 1 k Ω . As the two-terminal Ohmic resistance increases above 1 k Ω , the I-V curves exhibit superlinear characteristics. At values close to 1 k Ω , the I-V curves begin to approximate a linear behavior.



(a)



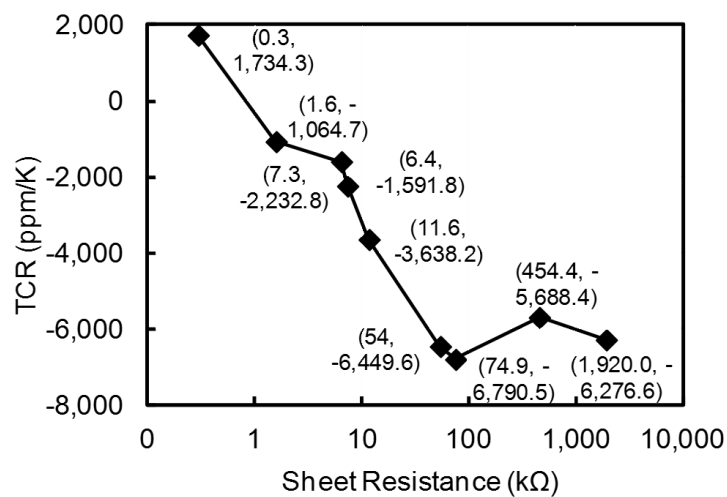
(b)

Fig. 11.1 (a) This figure illustrates the I-V characteristics of resistors on SiO₂/Si wafers with two terminal Ohmic resistances between 200 Ω to 6.37 kΩ and (b) of bolometer probes with two terminal Ohmic resistances between 72.5 kΩ and 550 kΩ.

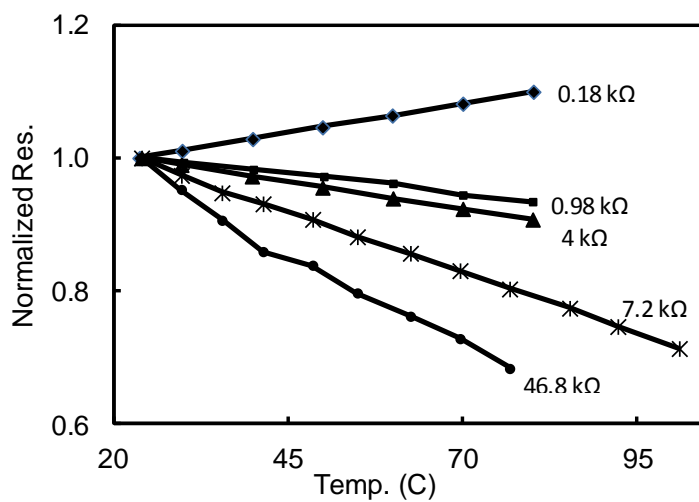
The TCR was then measured using a calibrated micro-heater plate with an atomic force microscope (AFM). The bolometer probe tips were brought in contact with the micro-heater plate. Temperatures were varied from 20 ± 0.1 °C to 101 ± 0.1 °C. Sheet resistance values were calculated using the two-terminal Ohmic resistance from the equation:

$$R_{\square} = W R_{2t} / L \quad (11.1)$$

where R_{\square} is the sheet resistance, R_{2t} is the two-terminal Ohmic resistance, W is the width, and L is the length of the device. A number of bolometer probes with sheet resistances between 7.3 k Ω/\square and 1920 k Ω/\square were tested and the results are shown in Fig. 11.2. TCR measurements of the resistors on a substrate were also performed using a micro-heater plate under a probe station. A number of resistors on a wafer with sheet resistances between 0.29 k Ω/\square and 6.4 k Ω are shown in Fig. 11.2.



(a)



(b)

FIG. 11.2 (a) This figure is a plot of the TCR as a function of sheet resistance for different devices. In the parenthesis: the first value represents the sheet resistance of the device and the second the TCR. (b) Normalized sheet resistance versus temperature.

In Fig. 11.2 (b) five plots of normalized sheet resistance, $R_{\square}(T) / R_{\square}(300K)$ versus temperature are shown. The normalized sheet resistances in Fig. 11.2 correspond to resistors on a wafer with sheet resistances of 0.29 k Ω/\square , 1.57 k Ω/\square , and 6.4 k Ω/\square , and microbolometers with sheet resistances of 11.6 k Ω/\square and 74.9 k Ω/\square . From Fig. 11.2 (b), it can be observed that as the resistance increases, the slope of the sheet resistance vs. temperature changes from positive to negative. The TCR values obtained from such measurements are plotted as a function of sheet resistance in Fig. 11.2 (a). With increasing sheet resistance, the TCR values first shift from positive to negative and then continue to decrease until they plateau (after a specific resistance value). There is an optimal sheet resistance beyond which there is no improvement in bolometric sensitivity. For the titanium films studied, this value was measured at approximately 74.9 k Ω/\square with a minimum TCR value of around -6,790 ppm/K.

Noise measurements on three bolometers with resistance values ranging from 14 k Ω/\square to 410 k Ω/\square were also performed. The bolometers were found to exhibit 1/f noise. The goal of the 1/f measurements is to determine the noise prefactor $K_{1/f}$, which is independent of the dimensions of the device and allows to compare various materials with varying thicknesses. Using equation:

$$S_i/I^2 = A/f \quad (11.2)$$

where S_i is the noise power spectral density function, I is the bias current, A is given by $A = K/V$ where $K_{1/f}$ is the bolometer noise prefactor and V is the volume. By plotting a linear fit and finding the value of $\log(S_i/I^2)$ at $f=1$ Hz, the value of $\log(S_i/I^2)$ is found. From $\log(S_i/I^2)$ the value of S_i/I^2 can be calculated, which can then be used to estimate the noise prefactor, $K_{1/f}$. K values for the three bolometers ranged from 10^{-22} cm³ to 5×10^{-21} cm³. Like the vanadium oxide films, K increases with increasing film resistance.

However, the level of noise was lower than that of vanadium oxide films [Bosman, 2001].

Another sheet resistance value of interest is near $1 \text{ k}\Omega/\square$ where the TCR is close to zero. This is useful for applications that require resistors that are not influenced by temperature fluctuations. These two results may be combined in order to develop microbolometers where the sensing area would be of a thickness that would provide the highest TCR in absolute values, while the electrodes would be of a thickness with near zero TCR.

Similar to the crossover from sublinear to superlinear I-V characteristics, the transition from positive to negative TCR also occurs at around $1 \text{ k}\Omega/\square$.

11.3 Measurements and results of tungsten thin films

Wafers with tungsten bolometers were also prepared to study their properties near the metal-insulator transition regime at 30 nm, 10 nm, 5 nm, and 2 nm thicknesses. The bolometer noise prefactor $K_{1/f}$ increased with decreasing thicknesses of tungsten, W. $K_{1/f}$ was measured to be $1.81 \cdot 10^{-21} \text{ cm}^3$ for a 30 nm thick device, $5.5 \cdot 10^{-21} \text{ cm}^3$ for a 10 nm thick device, and $9.7 \cdot 10^{-21} \text{ cm}^3$ for a 2 nm thick device. These results indicate that 1/f noise does increase with decreasing thicknesses acting to counter the sensitivity gains from increasing TCR.

Bolometer thermal properties were measured by applying heat via hot plate while the bolometer were enclosed in an aluminum sample holder mounted on an aluminum block. The temperature was ramped up and down while being measured with a thermistor. Both the bolometer and thermistor are in the same chamber. The bolometer's resistance was simultaneously monitored.

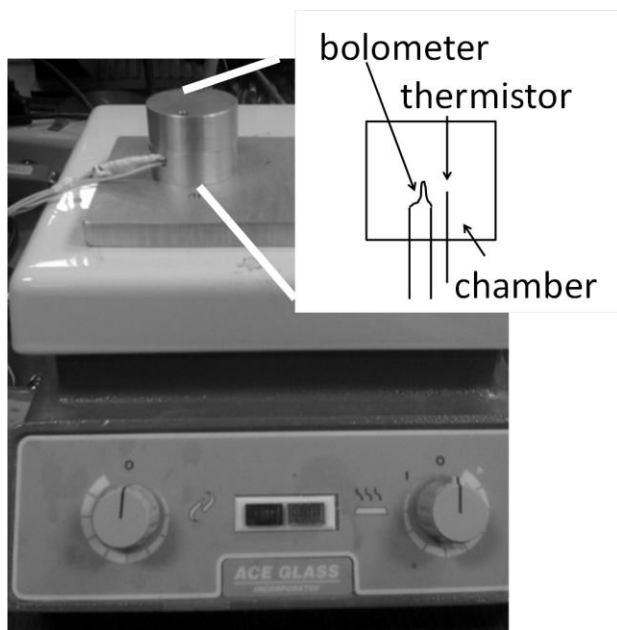


Fig. 11.3 Aluminum sample holder on a hot plate for characterizing thermal properties of the bolometers. Inset: schematic diagram of the setup.

Using the set-up described above the TCR of each of these bolometers was measured (Fig. 11.3). The highest values were obtained for a 2 nm thickness W film near 0.95%/K.

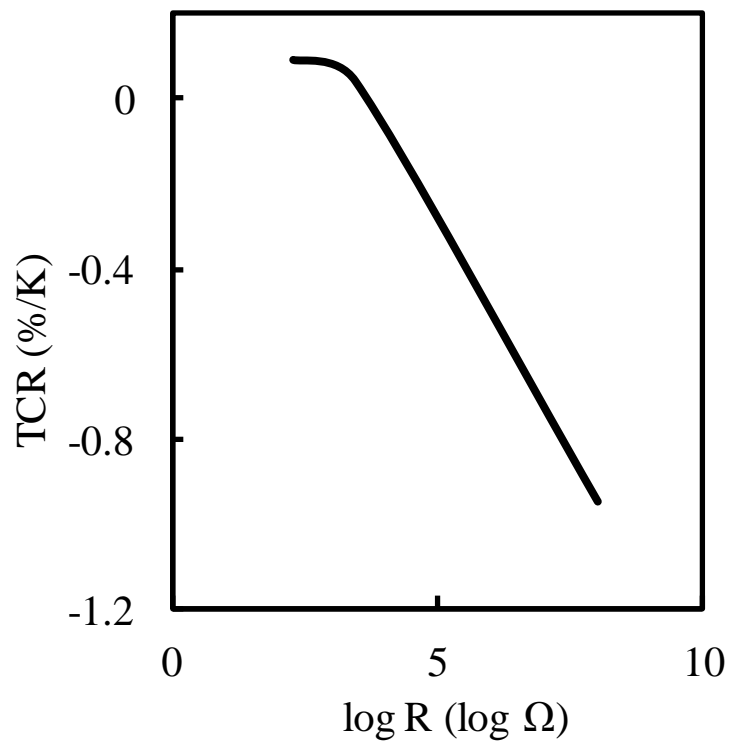


Fig. 11.4 The plot of TCR vs. $\log R$ plot shows a drop in TCR to very large negative values with increasing resistance.

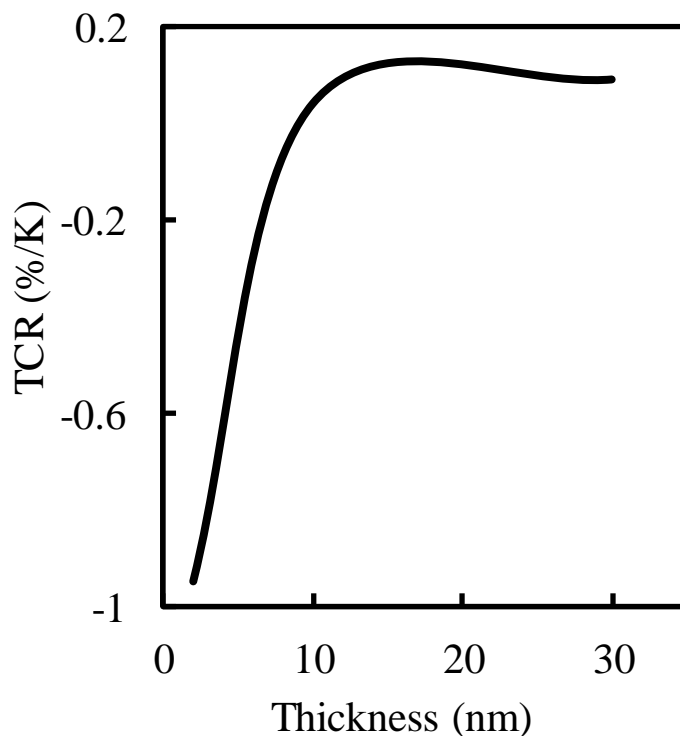


Fig. 11.5 TCR vs. film thickness plot shown the increase in negative TCR with decreasing thickness.

Thus, the findings obtained with Ti are also verified with W. As the bolometer thickness decreases and crosses over to the insulating regime, the resistance increases, and the TCR also increases in absolute values. TCR initially decreases from a positive value to a smaller positive value and ultimately to a very large negative value. For example a 30 nm thick W film has a resistance of 200 Ω and a measured TCR of 0.09%/K, a 10 nm W film has a resistance of 3 K Ω and a measured TCR of 0.04 %/K, while a 2 nm thick W film has a 116 M Ω resistance and a measured TCR of -0.95%/K.

11.4 Scanning thermal microscopy

These titanium thin film bolometers can be utilized in scanning thermal microscopy. Using an AFM, a thermal signal from the thermal probes is fed into an interface circuit [Gaitas, 2006]. Several interface circuits have been used for SThM including feedback circuits. Here a simple open loop interface circuit is used to demonstrate probe functionality. The circuit operates in an approximate constant power mode gauging the probe resistance variations (thermal conductance change), which can be derived from the changes in the output voltage. The interface circuit includes a Wheatstone bridge, two low noise instrumentation amplifiers (AD621), and a low pass filter (<1 kHz) for noise reduction. The thermal image is represented by the output voltage. The changes in the output voltage represent changes in the resistance of the probe due to sample variations. The resistance changes are associated with the conductive heat loss between the sample and probe (or thermal conductance changes of the sample) [Li ², 2001].

The probes are operated with an AFM. The thermal information from the probes was fed to a circuit such as the one described above, which in return interfaced with an AFM controller (Fig. 11.6). The probe was operated in a contact mode by scanning a thermal probe tip across a sample and making measurements at discrete points. The probe movement is controlled using the AFM's position-sensitive photodetector (PSPD). The interface circuit is then connected to the controller of a PicoMAPS AFM from Agilent.

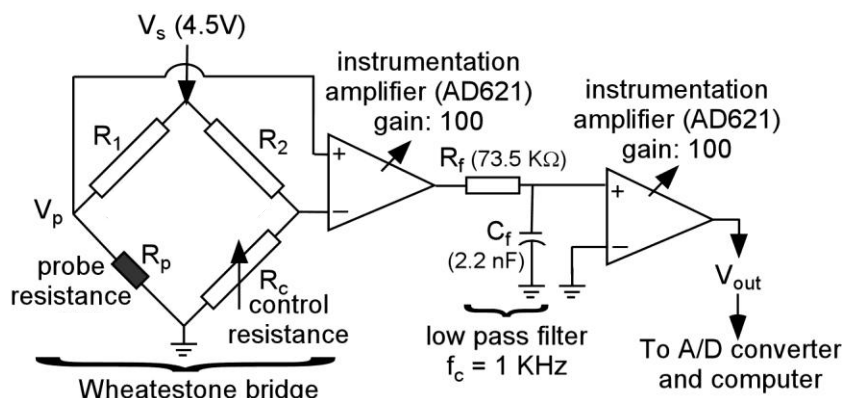


Fig. 11.6 The diagram for the Wheatstone bridge interface circuit shows the various components that include two instrumentation amplifiers AD621 with a gain set at 100 x and a low pass filter [Li², 2001].

Fig. 11.7 illustrates topographical and thermal images obtained simultaneously when a patterned sample is scanned by the bolometer probe. The sample is a silicon calibration grating with 10 μm long and 200 nm deep pitches. The plot of the circuit output voltage represents the thermal conductance changes of the sample.

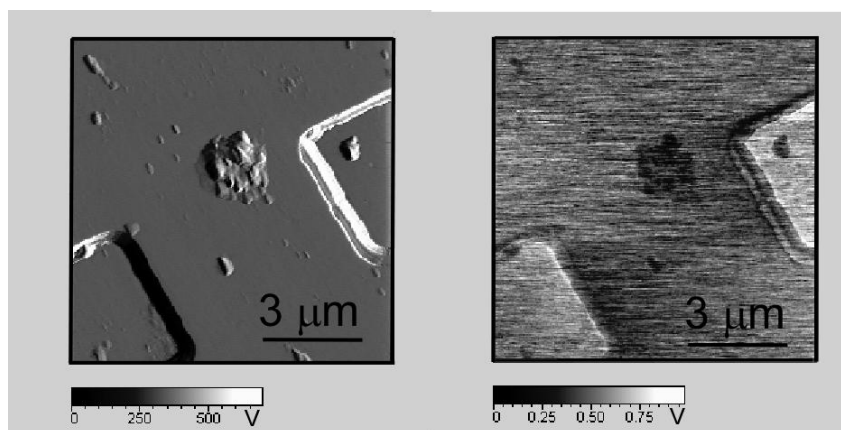


Fig. 11.7 a) Topographical and b) thermal scan.

These scans were performed with a $7.2 \text{ k}\Omega/\square$ thin film titanium probe with a measured TCR of $-3,638 \text{ ppm/K}$. Submicron features are visible. The noise equivalent temperature difference (NETD), which is also dependent on the circuitry, is calculated from [Li 2, 2001] to be approximately 18 mK. These microbolometers have operating temperatures of up to $115 \pm 0.1 \text{ }^\circ\text{C}$. Significant improvements in the NETD can be made by using more advanced circuitry. The probe design can be improved by further confining the bolometer thin film to the tip area. The TCR can be further improved by using alternative materials at the metal-insulator transition regime that may provide a higher TCR.

11.5 Conclusions

Titanium and tungsten thin film properties have been studied near the MIT regime in order to improve the sensitivity of titanium microbolometers. Sheet resistances corresponding to the highest TCR and the lowest TCR, in absolute values, were determined. The relationship between TCR and resistance may be typical for many metal and semimetal thin films near room temperatures. These findings were then used to develop scanning thermal probes. Applications of metal or semimetal films with resistances thicknesses near the MIT can be extended to infrared imaging and chemical sensing. Further study of metals and semimetal films is subsequently needed in order to determine the highest TCR as well as the lowest noise characteristics.

12

Conclusions and future research

This work studied two different general themes for cantilever based sensing, which were also combined in one cantilever. First, deflection sensing with ultra thin gold films was studied on silicon and polyimide cantilevers. It was found that the sensitivity of ultra thin gold films is considerably enhanced compared to bulk gold. Second, thermal imaging and heating were studied with ultra thin films on silicon nitride and silicon cantilevers. It was found that the thermal sensitivity is enhanced as one moves to thinner films. In order to carry out these studies a number of novel cantilevers were fabricated. These devices were used in applications of industrial importance.

First, a micromachined probe that includes two monolithically integrated sensors, one for measuring the mechanical movement of the probe and another for providing localized heating, has been used. The probe has a very large dynamic range, enabling monitoring movement of tens of microns in the out-of-plane axis. It is made from silicon and silicon oxide with a total thickness of 2 μm and a 5 nm or 10 nm gold sensing element. A method for calibrating a thermal probe is presented. Using this method the minimum detectable temperature change of a substrate is measured at 0.4 K, corresponding to 17 ppm changes in probe resistance. The maximum gauge factor of the probe is 4.1 ± 0.1 . Topographical scans were demonstrated. Plots of the change in resistance and cantilever deflection with the displacement of the sensing element on different materials demonstrate that the probe can be used to distinguish between materials with different mechanical properties. Furthermore, the probe was used to estimate the Young's modulus of the elastomer studied. The melting temperature of naphthalene is measured near 78.5 $^{\circ}\text{C}$, which is close to the reported melting point (79-81 $^{\circ}\text{C} \pm 0.3$ $^{\circ}\text{C}$). An array of these probes was also developed for high throughput SPM.

Similarly, silicon cantilever micro-heaters were used for nanofabrication. A moving nano-heater directed a chemical vapor deposition reaction (nano-CVD) demonstrating a tip-based nanofabrication (TBN) method. Localized nano-CVD of copper (Cu) and copper oxide (CuO) on a silicon (Si) and silicon oxide (SiO_2) substrate from gasses was demonstrated. These gasses included sublimated copper acetylacetonate ($\text{Cu}(\text{acac})_2$), argon (Ar), and oxygen (O_2). This technique is applicable to other materials.

A polyimide microcantilever with a thin film gold sensing element was developed for stress-based sensing of molecular analytes. The potential utility of the device for explosive detection was explored further by coating the cantilever with TTF-C4P, a colorimetric

receptor, to detect TNB vapor at 10 ppb level. It is important to note that this concentration is set by the vapor pressure of TNB, and is not the actual detection limit of the device, which is expected to be much lower. Nevertheless, even at this concentration, this new setup provides a marked improvement on the detection limit (low ppm level) seen for organic solutions containing TTF-C4P. The system can be used for the detection of other nitroaromatic explosives, including 2,4,6-trinitrotoluene (TNT), by using a modified TTF-C4P receptor with improved sensitivity.

Finally, titanium and tungsten thin film properties were studied near the MIT regime in order to improve the sensitivity of titanium microbolometers. The relationship between TCR, thickness and resistance seems to be typical for many metal and semimetal thin films near room temperatures. These findings indicate a dramatic increase in TCR close to 1%/K. These results were then used to develop a scanning thermal probe.

Table 12.1 Summary of major findings

Scientific findings	<ul style="list-style-type: none"> • 2x increase in deflection sensor gauge factor and sensitivity with decreasing thickness. • 3x increase in TCR (compared to typical metal thin films) with decreasing thickness near the metal to insulator transition regime. TCR near zero at certain thicknesses where the cross over from metal to insulator occurs. TCR has a maximum negative value at ultrathin levels.
Novel devices and experimental findings	<ul style="list-style-type: none"> • Device that combines deflection sensor and thermal element in one that can be used for melting point measurements and other applications in scanning probe microscopy. • 30x improvement in chemical detection with polymer cantilever coated with colorimetric receptor compared to stand alone colorimetric receptor sensing. • Number of new fabrication methods were developed including methods for polymer cantilevers. • A novel calibration method based on noise thermometry is developed and successfully used to calibrate the thermal probe. • New design improvements for thermal imaging have been proposed such as the "bow-tie" metallization design that increases sensitivity. • Manufacturing of individual nanostructures using a moving nano-heater that directs a chemical vapor deposition reaction (nano-CVD) is demonstrated for the first time. This technique is applicable to other materials.

12.1 Future work

Sensitivity and compliance can be further improved with the use of polymer, instead of silicon, as a structural material for the cantilevers. Sensitivity and gauge factors can be further improved using alternative sensing elements instead of gold such as thin films of other metals and metal oxides.

These innovations would allow for a wealth of new nanoscale high throughput applications including integrated circuit hot spot detection, material characterization, nano-indentation, dip pen nanolithography, cellular imaging, multiple single cell elastography and patch clamping. The author has already started working in the development of hollow microfluidic cantilevers with hollow tips and embedded sensing mechanisms and electrodes for high throughput patch clamping and other biological and materials applications. Additional applications the author has already explored include measuring cardiac rat and human myocyte contractility and contractile force and cancer cell adhesion using polymer cantilevers with embedded sensing elements.

These innovations could produce cantilever probes with a variety of sensing mechanisms that would enable multifunctionality, cost reductions, and higher throughput. The results presented in this thesis demonstrated that the AFM cantilever probes are well suited for liquid measurements of live cells. Furthermore, future devices may enable the development of new single cell disease biomarkers that combine electrophysiology and elastography measurements.

The findings relating to the increased TCR near the MIT regime may be extended to infrared imaging and chemical sensing. Further study of metals and semimetal films is subsequently needed in

order to determine the highest TCR as well as the lowest noise characteristics.

The polyimide cantilever used in chemical sensing can be modified for biological sensing such as measuring concentrations of low copy bio-molecules in serum.

The design improvements suggested for scanning thermal probe microscopy indicate that new metallization designs could yield an additional 5- to 7-fold increase in sensitivity.

Finally, nano-heaters can be used for CVD. Several materials can be grown on the substrate eliminating the need for multiple fabrication steps. Localization and control of heat allows the user to change conditions at the level of individual nanostructures enabling research in the thermodynamics and kinetics of growth. Applications are found in semiconductor and nano-device manufacturing, functionalizing surfaces and electrically connecting nanotubes and other nanostructures by growing electrically conductive lines. Future experiments will include controlling growth by intermittent heating and cooling, vertical growth (3D nanofabrication), applying of an electric field between the tip and the substrate, exploration of additional chemistries, and high throughput growth using multi-probe arrays.

Appendix 1. Fabrication processes

1. Fabrication of silicon cantilever

This process is based on an SOI wafer. Device thickness is selected depending on the desired thickness of the cantilever and the tip height.

1. TIP Formation

- a) Thermal Oxidation: At 1,100 °C, thickness: 300 nm
- b) Spin, expose, develop photoresist
- c) SiO₂ Etch: BHF
- d) Photoresist removal
- e) KOH; 30% KOH, 84°C, etch rate 0.9 μm/min, selectivity Si:oxide=500:1, Etch time approx. 6-7 min. until oxide caps fall off
- f) SiO₂ removal: BHF 4 min.

2. Oxidation sharpening & insulation

- a) Hydrofluoric acid etch
- b) Thermal Oxidation: 950°C
- c) Hydrofluoric acid etch
- d) Thermal Oxidation: 1,100°C, thickness: 100 nm

3. Cantilever formation

- a) Spin, expose, develop photoresist: 10 μm
- b) DRIE Si Etch: STS, cantilever thickness: 2 μm
- c) PR removal

4. Metal 1

- a) Spin, expose, develop photoresist
- b) Sputter: Ti 2 nm / Au 10 nm
- c) PR removal

5. Metal 2 (Au Pad Deposition)

- a) Spin, expose, develop photoresist
- b) Sputter: Ti 10 nm / Au 100 nm

6. Backside STS

- a) Spin, expose, develop photoresist for front side protection
- b) Oxide removal; BHF to remove the 100 nm thermal oxide on the back side for a better uniformity of STS
- c) Spin, expose, develop photoresist processing on the back side of wafer
- d) STS DRIE: 2 hr

7. Device Release

- a) BHF release: Remove the buried oxide with BHF.
- b) PR removal: Acetone / PRS-2000/ IPA / DI water.

8. Metal Deposition for Reflection

- a) Sputter TiW/Al: TiW (Ti10%) 110 nm / Al 50 nm

2. Fabrication of silicon nitride cantilever

This process is based on a Si_3N_4 cantilever. The steps include:

1. Tip formation

- a) PECVD SiO_2 50 nm
- b) Spin, expose, develop photoresist
- c) SiO_2 Etch BHF
- d) STS Isotropic Etch

2. Oxidation sharpening

- a) Thermal Oxidation 1100°C 1210 nm
- b) Etch 10:1 HF 30 sec

3. Cantilever formation

- a) LPCVD O/N/O deposition: 500 nm/200 nm/400 nm

- b) Spin, expose, develop photoresist
 - c) Oxide Etch: BHF
 - d) Nitride/oxide Etch: RIE, BHF
4. Tip O/N/O layer removal
- a) Spin, expose, develop photoresist
 - b) Oxide Etch: BHF
 - c) Nitride/oxide etch: RIE, BHF
5. Metal 1
- a) Spin, expose, develop photoresist
 - b) Sputter
 - c) Ti/W: Ti 20 nm / W 100 nm
 - d) Lift-Off
6. Metal 2
- a) Spin, expose, develop photoresist
 - b) Evaporate Cr/Au: 10 nm /250 nm
 - c) Lift-Off
7. Backside STS
- a) Backside nitride etch
 - b) Backside oxide etch
 - c) STS DRIE
 - d) Al evaporation for reflection
 - e) PR removal
 - f) Release

3. Fabrication of polyimide cantilever

1. Oxidation of a silicon wafer.
 - a) Thermal Oxidation: 1,100 °C, target thickness: 1500 nm, process time 5:30 hr
2. Polyimide coating

- a) Spin 1.5 μm PI 2610
- b) Bake
- c) Cure

3. Cantilever formation

- a) Spin, expose, develop photoresist
- b) Al deposition: evaporate 150 nm
- c) Lift-off
- d) Polyimide patterning
- e) Al removal: etchant

4. Metal

- a) Spin, expose, develop photoresist
- b) Evaporate Cr/Au
- c) Lift-off

5. Backside STS

- a) Spin, bake photoresist
- b) Oxide removal on the back side: BHF for removal of 1500 nm thermal oxide
- c) Spin, expose, develop photoresist
- d) STS DRIE

6. Device Release

- a) BHF release
- b) Remove the buried oxide with BHF
- c) PR removal

Bibliography

[Adkins, 1987] C J Adkins, *J. Phys. C: Solid State Phys.* 20, 235-244 (1987)

[Akamine, 1990] Akamine, R. C. Barrett, C. Quate, "Improved atomic force microscope images using microcantilevers with sharp tips", *Appl. Phys. Lett.* 57, 316 (1990)

[Albrecht,1990] T. R. Albrecht, S. Akamine, T. E. Carver, and C. F. Quate, "Microfabrication of cantilever styli for the atomic force microscope", *Journal of Vacuum Science & Technology A: Vacuum, Surfaces, and Films*, Vol. 8, No. 4. (1990)

[Allen, 2009] N.J. Allen, D. Wood, M.C. Rosamond and D.B. Sims-Williams, "Fabrication of an in-plane SU-8 cantilever with integrated strain gauge for wall shear stress measurements in fluid flows", *Procedia Chemistry*, Volume 1, Issue 1 (2009)

[Arlett, 2010] J. L. Arlett and M. L. Roukes, "Ultimate and practical limits of fluid-based mass detection with suspended microchannel resonators", *Journal of Applied Physics* 108, 084701 (2010)

[Baller, 2000] M.K. Baller, H.P. Lang, J. Fritz, C. Gerber, J.K. Gimzewski, U. Drechsler, H. Rothuizen, M. Despont, P. Vettiger, F.M. Battison, J.P. Ramseyer, P. Fornaro, E. Meyer, H.J. Güntherodt. "A cantilever array-based artificial nose". *Ultramicroscopy*, 82, 1-9 (2000)

[Basu, 2004] A. Basu, S. McNamara, and Y.B. Gianchandani, "Scanning Thermal Lithography: Maskless, Submicron Thermochemical Patterning of Photoresist by Ultracompliant Probes," *Journal of Vacuum Science and Technology B: Microelectronics and Nanostructures*, 22(6) (2004)

[Berger, 1997] R. Berger, E. Delamarche, H.P. Lang, Ch. Gerber, J.K. Gimzewski, E. Meyer, H.-J. Güntherodt, *Science* 276, 2021

(1997).

[Bhushan, 1999] Bhushan, B. Handbook of Micro/Nanotribology. Boca Raton : CRC press (1999)

[Binnig, 1986] G. Binnig, C. Quate, C. Gerber. Phys. Rev. Lett. 3; 56(9): 930-933 (1986)

[Bird, 2012] John Bird, Electrical and Electronic Principles and Technology, Routledge (2012)

[Blaine, 1999] Roger L. Blaine, C. Gray Slough and Duncan M. Price, "Micro Thermal Analysis Calibration, Repeatability and Reproducibility", Proceedings of the Twenty-Seventh Conference of the North American Thermal Analysis Society (1999)

[Block, 1973] W. H. Block, O. L. Gaddy, IEEE Journal of Quantum Electronics, Vol. Qe-9, Ko. 1 I, (1973)

[Bosman, 2001] G. Bosman (editor), Proceedings of the 16th International Conference, Noise in physical systems and 1/f fluctuations, ICNF (2001)

[Calleja, 2003] M. Calleja, P. A. Rasmussen, A. Johansson, A. Boisen, "Polymeric mechanical sensors with piezoresistive readout integrated in a microfluidic system", Proc. SPIE, 5116, 314 (2003)

[Chabloz, 2000] M. Chabloz, J. Jiao, Y. Yoshida, T. Matsuura, K. Tsutsumi, "A Method to Evade Microloading Effect in Deep Reactive Ion Etching for Anodically Bonded Glass-silicon Structures," IEEE Intl. Conf. on Micro Electro Mechanical Systems (2000)

[Chen, 1995] G.Y. Chen, T. Thundat, E.A. Wachter, and R.J. Warmack. "Adsorption-induced surface stress and its effects on resonance frequency of microcantilevers". Journal of Applied Physics, 77(8) (1995)

[Chopra, 1979] K. L. Chopra, "Thin Film Phenomena" (McGraw-

Hill, New York) (1979)

[Chui, 1996] B. W. Chui, H. J. Mamin, B. D. Terris, T. D. Stowe, D. Rugar, and T. W. Kenny, "Low stiffness silicon cantilevers for thermal writing and piezoresistive readback with the atomic force microscope", *Appl. Phys. Lett.*, 69, 2767 (1996)

[Chui, 1998] B. W. Chui, T. D. Stowe, Y. S. Ju, K. E. Goodson, T. W. Kenny, H. J. Mamin, B. D. Terris, "Low-stiffness silicon cantilevers with integrated heaters and piezoresistive sensors for high-density AFM thermomechanical data storage", *Journal of Microelectromechanical Systems*, vol. 7, issue 1, pp. 69-78 (1998)

[Condorelli, 1994] G. G. Condorelli, G. Malandrino, I. Fragala. *Chem. Mater.* 6, 1861-1866 (1994)

[Condorelli, 1995] G. G. Condorelli, G. Malandrino, I. Fragala. *Chem. Mater.* 7, 2096-2103 (1995)

[Costa, 2004] K. D. Costa, "Single-cell elastography: Probing for disease with the atomic force microscope", *Disease Markers*, Vol. 19, pp 139-154 (2004)

[Cross, 2007] S. E. Cross, Y. Jin, J. Rao and J. K. Gimzewski, "Nanomechanical analysis of cells from cancer patients", *Nature Nanotechnology*, vol. 2, pp. 780-783 (2007)

[Dow] dowcorning.com/DataFiles/090007c8801c2d86.pdf

[Eminoglu, 2003] S. Eminoglu, D. S. Tezcan, M. Y. Tanrikulu, T. Akin, *Sensors and Actuators A* 109, 102–113 (2003)

[Engel, 2000] A. Engel, and D.J. Müller, "Observing single biomolecules at work with the atomic force microscope", *Nature Structural Biology*, vol. 7, no. 9, pp. 715-718 (2000)

[Ercag, 2009] Ercag, A. Uezer, R. Apak, *Talanta*, 78, 772 (2009)

[Erlandsson, 1988] R. Erlandsson, G.M. McClelland, C.M. Mate, S. Chiang, "Atomic force microscopy using optical

interferometry". J. Vac. Sci. Technol. A, 6(2), 266-70 (1988)

[Esfahani, 1992] R. N. Esfahani, G. J. Maclay, G. W. Zajac, Thin Solid Films, 219, 257-265 (1992)

[Fair, 1999] V. K. Fair, R. B. Pamula, "Detection of nanogram explosive particles with a MEMS sensor", 321, Proc. SPIE, Vol. 3710 (1999)

[Favre, 2011] M. Favre, J. Polesel-Maris, T. Overstolz, P. Niedermann, S. Dasen, G. Gruener, R. Ischer, P. Vettiger, M. Liley, H. Heinzemann, A. Meister, "Parallel AFM imaging and force spectroscopy using two-dimensional probe arrays for applications in cell biology", Journal of Molecular Recognition, Special Issue: AFM on Life Sciences and Medicine, Volume 24, Issue 3 (2011)

[Fenwick, 2009] O. Fenwick, L. Bozec, D. Credgington, A. Hammiche. Nature Nanotechnology 4, 664 - 668 (2009)

[Fischer, 2008] H. Fischer, "Calibration of Micro-Thermal Analysis for the Detection of Glass Transition Temperatures and Melting Points", Journal of Thermal Analysis and Calorimetry, Vol. 92 (2008)

[Florin, 1995] E. L. Florin, M. Rief, H. Lehmann, M. Ludwig, C. Dornmair, V. T. Moy, H. E. Gaub, "Sensing specific molecular interactions with the atomic force microscope", Issues 9-10, Pages 895-901 , Biosensors and Bioelectronics (1995)

[French, 2005] P.J. French & P.M. Sarro, "Chapter 15 Micromachining Technology", from book edited by: Jan Korvink, Oliver Paul, "MEMS: A Practical Guide to Design, Analysis and Applications", Springer (2005)

[Fritz, 2000] J. Fritz, M. K. Baller, H. P. Lang, H. Rothuizen, P. Vettiger, E. Meyer, H. -J. Güntherodt, Ch. Gerber, J. K. Gimzewski, Science 288, 316 (2000)

[Fryer, 2000] D.S. Fryer, P.F. Nealey, J.J. de Pablo, "Thermal

probe measurements of the glass transition temperature for ultrathin polymer films as a function of thickness", *Macromolecules* 33 (2000)

[Fung, 2011] C. K. M. Fung, N. Xi, R. Yang, K. Seiffert-Sinha, K. Lai, and A. A. Sinha, "Quantitative analysis of human keratinocyte cell elasticity using atomic force microscopy (AFM)", *IEEE Transactions on Nanobioscience*, vol. 10, issue 1, pp. 9-15 (2011)

[Gaitas, 2006] A. Gaitas, "Polyimide Probes for Contact Mode Subsurface SPM Thermal Imaging", *Microscopy and Analysis*, Volume 20, Issue 2 (2006)

[Gaitas, 2006^B] A. Gaitas, Y. B. Gianchandani, "An Experimental Study of Contact Mode Scan Speed Constraints For Polyimide Cantilever Probes", *Ultramicroscopy*, Volume 106, Issues 8-9, Pages 874-880 (2006)

[Gaitas, 2008] A. Gaitas, "A Preliminary Study of Spatial Resolution Enhancement of Confocal and Triangulation Displacement Meters Using Contact Mode Scanning Probes", *Rev. Sci. Instrum.* 79, 023703 (2008)

[Gaitas, 2009] A. Gaitas, W. Zhu, N. Gulari, E. Covington, C. Kurdak, "Characterization of room temperature metal microbolometers near the metal-insulator transition regime for scanning thermal microscopy", *Appl. Phys. Lett.* 95, 153108 (2009)

[Gaitas, 2009^B] A. Gaitas, B. Mitra, A. Basu, W. Zhu, "Scanning Probe Assisted localized CNT growth", Patent application number 12/464,039, Publication number US 2010/0055349 A1 (2009)

[Gaitas, 2011^B] A. Gaitas, S. Gianchandani, and W. Zhu, *Review of Scientific Instruments*, 82 053701 (2011)

[Gaitas, 2011^C] A. Gaitas, T. Li, W. Zhu, *Sensors and Actuators*

A: Physical, 168 2 (2011)

[Gaitas, 2011^{Mag}] A. Gaitas, P. French, "Magnetic Microheaters For Cell Separation, Manipulation, and Lysing", The 16th International Conference On Solid-State Sensors, Actuators and Microsystems (2011)

[Gaitas, 2012] A. Gaitas, P. French. Sensors & Actuators A: Physical, Volume 186 Pages 125–129 (2012)

[Gennissen, 1997] P.T.J. Gennissen, M. Bartek , P.M. Sarro, P. J. French, "Bipolar compatible epitaxial poly for smart sensor-stress minimisation and applications", Sensors and Actuators, VolA62, pp 636-645 (1997)

[Godin, 2010] M. Godin, V. Tabard-Cossa, Y. Miyahara, T. Monga, P. J. Williams, L. Y. Beaulieu, R B. Lennox and P. Grutter, Nanotechnology, 21, 075501 (2010)

[Gorbunov, 1994] A.A. Gorbunov, W. Pompe. Physica Status Solidi (a) 145(2):333–338 (1994)

[Gregory, 2003] O.J. Gregory, T. You, "Stability and piezoresistive properties of indium-tin-oxide ceramic strain gages", Sensors, Vol.2 (2003)

[Guckel, 1988] H. Guckel, D.W. Burns, C. Visser, H. Tillmans, D. Deroo, "Fine-grained polysilicon films with built-in tensile strain", IEEE Trans. Electron. Dev. 35 pp 800–801 (1988)

[Guntherodt, 2000] Guntherodt et al., "A cantilever array-based artificial nose," Ultramicroscopy, 82, 1-9 (2000)

[Hamill, 1981] O. P. Hamill, A. Marty, E. Neher, B. Sakmann, F. J. Sigworth, "Improved patch-clamp techniques for high-resolution current recording from cells and cell-free membrane patches," *Pflugers Arch.*, vol. 391(2) (1981)

[Hammiche, 1996] A. Hammiche, D. J. Hourston, H. M. Pollock, M. Reading and M. Song, "Scanning thermal microscopy: subsurface imaging, thermal mapping of polymer blends, and

- localized calorimetry", *J. Vac. Sci. Technol., B*, 14 (1996)
- [Hammiche, 1996B] A. Hammiche, H.M. Pollock, M. Song, D.J. Hourston, *Meas. Sci. Technol.*, V 7, pp. 142 (1996)
- [Hammiche, 1999] A. Hammiche, H. M. Pollock, M. Reading, M. Claybourn, P. H. Turner, and K. Jewkes, *Applied Spectroscopy*, 53 7 810 (1999)
- [Hammiche, 2000] A. Hammiche, L. Bozec, M. Conroy, H. M. Pollock, G. Mills, J. M. R. Weaver, D. M. Price, M. Reading, D. J. Hourston, and M. Song, *Journal of Vacuum Science & Technology B: Microelectronics and Nanometer Structures*, 18, 1322 (2000)
- [Hammiche, 2001] A. Hammiche, H. M. Pollock, M. Reading, patent number 6,200,022 (2001)
- [Harsányi, 2000] G. Harsányi, "Sensors in Biomedical Applications: Fundamentals", *Technology & Applications*, CRC Press (2000)
- [Henini, 2002] M. Henini, M. Razeghi, "Handbook of infrared detection technologies", Elsevier, p. 450 (2002)
- [Horber, 2003] J. K. H. Horber, and M. J. Miles, "Scanning probe evolution in biology," *Science*, vol. 302, pp. 1002-1005 (2003)
- [Hull, 1999] R. Hull, "Properties of Crystalline Silicon", *The Institution of Engineering and Technology*, p. 426 (1999)
- [Ishihara, 1999] K. Ishihara, C. F. Tung, A. A. Ayón, "An Inertial Sensor Technology Using DRIE and Wafer Bonding with Interconnecting Capability," *J. Micromech. Sys.*, 8 (4) (1999)
- [Iyer, 2009] S. Iyer, R. M. Gaikwad, V. Subba-Rao, C. D. Woodworth and I. Sokolov, "Atomic force microscopy detects differences in the surface brush of normal and cancerous cells," *Nature Nanotechnology*, vol. 4, pp. 389-393 (2009)

- [Jen, 2003] S.U. Jen, C.C. Yu, C.H. Liu, G.Y. Lee, "Piezoresistance and electrical resistivity of Pd, Au, and Cu films", *Thin Solid Films* 434, 316–322 (2003)
- [Jiang, 2008] Y. Jiang, H. Zao, N. Zhu, Y. Lin, P. You, L. Mao, *Angew. Chem.* 120, 8729 (2008)
- [Johansson, 2005] A. Johansson, M. Calleja, P.A. Rasmussen, A. Boisen. "SU-8 cantilever sensor system with integrated readout", *Sensors and Actuators A: Physical.*, Vols. 123-124, Pages 111-115 (2005)
- [Kalpakjian, 2006] S. Kalpakjian, S. R. Schmid. "Manufacturing Engineering and Technology". 5th Edition. Pearson Prentice Hall (2006)
- [Kidong Park, 2008] K. Park, J. Jang, D. Irimia, J. Sturgis, James Lee, J. P. Robinson, M. Toner, R. Bashir, "Living cantilever arrays for characterization of mass of single live cells in fluids", *Lab Chip*, 8, 1034-1041 (2008)
- [Kim, 2003] B.H. Kim, O. Mader, U. Weimar, R. Brock, D.P. Kern, "Detection of antibody peptide interaction using microcantilevers as surface stress sensors". *J. Vac. Sci. Technol. B*, 21(4), 1472-1475 (2003)
- [King, 2002] W.P. King, K.E. Goodson, "Thermomechanical Formation and Thermal Imaging of Polymer Nanostructures" in *Heat Transfer and Fluid Flow in Microscale and Nanoscale Devices*, M. Faghri and B. Sunden, Eds., Southampton: WIT Press (2002)
- [King, 2010] K. Lai, A. Gaitas, R. Yang, C. K. M. Fung, N. Xi, "Ultra-compliant Thermal AFM Probes for Studying of Cellular Properties", *IEEE NANO* (2010)
- [King, 2011] K. Lai, A. Gaitas, N. Xi, R. Yang, C. K. M. Fung, "Development and Testing of Nano Robot End Effector For Cell Electrophysiology and Elastography Studies", *Proceedings of the*

IEEE Nano (2011)

[Knight, 1969] M. J. Knight, "Effect of Structure on the Piezoresistive Properties of Thin Metal Films", *J. Vac. Sci. Technol.* 6, 706 (1969)

[Kovacs, 1998] G.T.A. Kovacs, "Micromachined Transducers Sourcebook", McGraw-Hill, New York, NY (1998)

[Kühl, 1998] K. Kühl, S. Vogel, U. Schaber, R. Schafflik, B. Hillerich, "Advanced Silicon Trench Etching in MEMS Applications," *SPIE*, vol. 3511 (1998)

[Kunieda, 2005] M. Kunieda, B. Lauwers, K.P. Rajurkar, B.M. Schumacher. *Annals of the CIRP* 54(2):599–622 (2005)

[Lai, 1995] J. Lai, M. Chandrachood, A. Majumdar, J.P. Carrejo, *IEEE Electron Dev. Lett.* 16 (1995)

[Lee, 2005] J. Lee, Y. B. Gianchandani, "A temperature-dithering closed-loop interface circuit for a scanning thermal microscopy system", *J. Microelectromech. Syst.*, 14 (2005)

[Lee, 2006] J. Lee, T. Beechem, T. L. Wright, B. A. Nelson, S. Graham, W. P. King, *Journal of Microelectromechanical Systems*, Vol. 15, No. 6 (2006)

[Lee, 2007] J. Lee, W. P. King, "Microcantilever actuation via periodic internal heating", *Review of Scientific Instruments*, 78, 126102, 2007

[Lee, 2010] Y. H. Lee, H. Liu, J. Y. Lee, S. H. Kim, S. K. Kim, J. L. Sessler, Y. Kim, J. S. Kim. *Chem. Eur. J.* 16, 5895 (2010)

[Lefèvre, 2006] S. Lefèvre, S. Volzb, P.-O. Chapuis, "Nanoscale heat transfer at contact between a hot tip and a substrate", *International Journal of Heat and Mass Transfer* Volume 49, Issues 1-2 (2006)

[Lerchner, 2000] J. Lerchner, D. Caspary, G. Wolf, *Sensors and Actuators B*, V 70, pp. 57-66 (2000)

- [Li², 2001] M.-H.Li, "Surface Micromachined Polyimide Scanning Thermocouple and Bolometer Probes", University of Wisconsin-Madison, Thesis (2001)
- [Li, 1994] C. Li, P. Hesketh, G. Maclay, "Thin gold film strain gauges", 813, J. Vac. Sci. Technology, Vol. A12 (3) (1994)
- [Li, 2000] M.-H. Li, Y. B. Gianchandani, "Microcalorimetry applications of a surface micromachined bolometer-type thermal probe", J. Vac. Sci. Technol. B 18, 3600 (2000)
- [Li, 2001] M.-H. Li, J.J. Wu, and Y.B. Gianchandani, IEEE/ASME Journal of Micro-electromechanical Systems, 10(1) (2001)
- [Li, 2003] M.-H. Li, Y.B. Gianchandani, Sensors and Actuators, 104 (2003)
- [Li, 2007] M. Li, H. X. Tang, M. L. Roukes, "Ultrasensitive NEMS-based cantilevers for sensing, scanned probe, and very-high frequency applications", Nature Nanotechnology 2, 114 - 120 (2007)
- [Luo, 1996] K. Luo, Z. Shi, J. Lai, A. Majumdar, Appl. Phys. Lett., V 68, pp. 325(1996)
- [Majumdar, 1992] A. Majumdar, P. I. Oden, J. P. Carrejo, L. A. Nagahara, J. J. Graham, and J. Alexander, "Nanometer scale lithography using the atomic force microscope", Appl. Phys. Lett. 61, 2293 (1992)
- [Majumdar, 1999] A. Majumdar, "Scanning thermal microscopy", Annu. Rev. Mater. Sci., V 29 (1999)
- [Malshe, 2010] A.P. Malshe, K.P. Rajurkar, K.R. Virwani, C.R. Taylor, D.L. Bourell, G. Levy, M.M. Sundaram, J.A. McGeough, V. Kalyanasundaram, A.N. Samant. CIRP Annals - Manufacturing Technology, Volume 59, Issue 2 (2010)
- [Mamin, 1992] H. J. Mamin and D. Rugar, "Thermomechanical writing with an atomic force microscope tip", Appl. Phys. Lett.

61, 1003 (1992)

[Mamin, 1995] H. J. Mamin, B. D. Terris, L. S. Fan, S. Hoen, R. C. Barrett, and D. Rugar, "High-density data storage using proximal probe techniques", pp. 681-699, IBM J. Res. Develop. (1995)

[Manalis, 1996] S.R. Manalis, S.C. Minne, A. Atalar, C.F. Quate, "Interdigital cantilevers for atomic force microscopy". Appl. Phys. Lett., 69 (1996)

[Martin, 1987] Y. Martin, Y.; H.K. Wickramasinghe, "Magnetic imaging by force microscopy with 1000 Å resolution", Applied Physics Letters, Volume 50, Issue 20 (1987)

[Mattews, 1983] J. W. Mattews, "Epitaxial Growth", Part B, Academic Press, New York (1983)

[Meyer, 1988] Meyer, G., Amer, N.M. "Novel optical approach to atomic force microscopy". Appl. Phys. Lett., 53(12) (1988)

[Minne, 1995] S. Minne, S. Manalis, C. Quate, "Atomic force microscopy for high speed imaging using cantilevers with an integrated actuator and sensor", Appl. Phys. Lett. 67 (1995)

[Mitra, 2009] B. Mitra, A. Gaitas, "Thermally actuated tapping mode atomic force microscopy with polymer microcantilevers", Rev. Sci. Instrum. 80, 023703 (2009)

[Moore 2004] D. S. Moore, "Instrumentation for trace detection of high explosives", Rev. Sci. Instruments, v 75 (8) (2004)

[Morris, 1977] J. Morris and T. Coutts, Thin Solid Films, 47, 1 65 (1977)

[Moulin, 2000] A.M. Moulin, S.J. O'Shea and M.E. Welland, Ultramicroscopy 82, 23 (2000)

[Nelson¹, 2007] B. A. Nelson, Dissertation, "Nanoscale Thermal Processing Using a Heated Atomic Force Microscope Tip", Georgia Institute of Technology (2007)

- [Nelson², 2007] B.A. Nelson, W.P. King, "Temperature calibration of heated silicon atomic force microscope cantilevers", *Sensors and Actuators A* 140 (2007)
- [Nelson³, 2007] B. A. Nelson, W. P. King, "Measuring Material Softening With Nanoscale Spatial Resolution Using Heated Silicon Probes", *Review of Scientific Instruments* 78, 023702 (2007)
- [Neugebauer, 1962] C. A. Neugebauer and M. B. Webb, *J. Appl. Phys.*, 33, 74-82 (1962)
- [Nielsen, 2004] K.A. Nielsen, W-S. Cho, J.O. Jeppesen, V. M. Lynch, J. Becher, J. L. Sessler, "Tetra- TTF Calix[4]pyrrole: A Rationally Designed Receptor for Electron-Deficient Neutral Guests", *J. Am. Chem. Soc.*, 126(50), pp. 16296-16297 (2004)
- [Nikiforov, 2011] M. P. Nikiforov, Roger Proksch, "Dynamic SPM Methods for Local Analysis of Thermo-Mechanical Properties", in *Scanning Probe Microscopy of Functional Materials, Part 3*, 199-229 (2011)
- [Nowroozi-Esfahani, 1990] R. Nowroozi-Esfahani and G. J. Maclay, *J. Vac. Sci. Technol. A*, 8 (4) 3591-3597 (1990)
- [Ocola, 1996] L.E.Ocola, D.Fryer, P.Nealey, J.dePablo, F.Cerrina, S. Kämmer, *J. Vac. Sci. Technol. B*, V 14(6), pp. 3974-9 (1996)
- [Park, 2010] J.S. Park, F. Le Derf, C.M. Bejger, V. M. Lynch, J.L. Sessler, K.A. Nielsen, C. Johnsen, J. O. Jeppesen, "Positive Homotropic Allosteric Receptors for Neutral Guests: Annulated Tetrathiafulvalene-Calix[4]Pyrroles as Colorimetric Chemosensors for Nitroaromatic Explosives," *Chemistry*, 18;16(3):848-54 (2010)
- [Parker, 1963] R. L. Parker and A. Krinsky, "Electrical Resistance-Strain Characteristics of Thin Evaporated Metal Films," *J. App. Phys.*, v 34, n 9, pp.2700-2708 (1963)

- [Pearce, 2006] T. C. Pearce, S. S. Schiffman, H. T. Nagle, J. W. Gardner, Handbook of Machine Olfaction: Electronic Nose Technology, Wiley Vch. (2006)
- [Pedrak, 2003] R. Pedrak, Tzv. Ivanov, K. Ivanova, T. Gotszalk, N. Abedinov, I. W. Rangelow, K. Edinger, E. Tomerov, T. Schenkel, P. Hudek, "Micromachined atomic force microscopy sensor with integrated piezoresistive sensor and thermal bimorph actuator for high-speed tapping-mode atomic force microscopy phase-imaging in higher eigenmodes", Journal of Vacuum Science & Technology B, 21(6) (2003)
- [Peiner, 2006] E. Peiner, A. Tibrewala, R. Bandorf, S. Biehl, H. Lüthje and L. Doering, "Micro force sensor with piezoresistive amorphous carbon strain gauge", Sensors and Actuators A: Physical, Volumes 130-131 (2006)
- [Piner, 1999] R.D. Piner, J. Zhu, F. Xu, S. Hong, C.A. Mirkin. Science 283(5402):661–663 (1999)
- [Pinnaduwege, 2004] L. A. Pinnaduwege, A. Wig, D. L. Hedden, A. Gehl, D. Yi, T. Thundat, and R. T. Lareau, "Detection of trinitrotoluene via deflagration on a microcantilever", J. Appl. Phys., v. 95, 5871 (2004)
- [Pinnaduwege, 2005] A. L. Pinnaduwege, H-F. Ji, and T. Thundat, "Moore's Law in Homeland Defense: An Integrated Sensor Platform Based on Silicon Microcantilevers" IEEE Sensors Journal, v. 5(4), pp. 774–785 (2005)
- [Price, 1999] D. M. Price, M. Reading, A. Hammiche, H. M. Pollock, International Journal of Pharmaceutics, 192, issue 1 (1999)
- [Priest, 2006] B. Priest, G. J. Kaczorowski and M. L. Garcia, "Ion channel modulators: new targets and new indications for old targets," *Curr. Opin. Drug Discovery Dev.*, vol. 9 (2006)
- [Randall, 2010] J. N. Randall, J. B. Ballard, J. W. Lyding, S. Schmucker, J. R. Von Ehr, R. Saini, H. Xu, Y. Ding.

Microelectronic Engineering. Volume 87, Issues 5-8, The 35th International Conference on Micro- and Nano-Engineering (2010)

[Ricci, 2006] A. Ricci, E. Giuri and C. Ricciardi, Presentation at the COMSOL users conference, Milano (2006)

[Riga, 1991] A.T. Riga, C.M. Neag, ASTM Committee E-37 on Thermal Measurements (1991)

[Rogers, 2004] B. Rogers, L. Manning, T. Sulchek, J.D. Adams, "Improving tapping mode atomic force microscopy with piezoelectric cantilevers", *Ultramicroscopy* 100 (2004)

[Rohsenow, 1998] W. M. Rohsenow, J. P. Hartnett, Y. I. Cho, *Handbook of heat transfer*, McGraw-Hill, New York, (1998)

[Ryu, 2008] H. Ryu, S. H. Cheon, S. M. Cho, W. S. Yang, B. G. Yu, C. A. Choi, M. L. Lee, "Sputtered silicon antimony thin film for the infrared detection layer of microbolometer", *IEEE SENSORS* (2008)

[Sarid, 1991] D. Sarid, "Scanning Force Microscopy: With Applications to Electric, Magnetic, and Atomic Forces I-XI", 253, Oxford Univ. Press, New York (1991)

[Schofield, 2012] A. R. Schofield, K. P. Bloschock, T. W. Kenny. *Proceedings of the SPIE*, Volume 7637, pp. 76371D-76371D-6 (2010)

[Shi, 2001] L. Shi, Mesoscopic, "Thermophysical Measurements of Microstructures and Carbon Nanotubes", University of California, Berkeley, Thesis (2001)

[Shi, 2002] L. Shi, A. Majumdar, "Thermal Transport Mechanisms at Nanoscale Point Contacts," *Journal of Heat Transfer*, Vol. 124, pp. 329-337 (2002)

[Soofi, 2009] S. S. Soofi et al., *J. Struct. Biol.* 167(3): 216-219 (2009)

[Stepien, 2007] M. Stepien, B. Donnio, J. L. Sessler. *Angew.*

Chem. 119, 1453 (2007)

[Subramanian, 2002] A. Subramanian, P.I. Oden, S.J. Kennel, K.B. Jacobson, R.J. Warmack, T. Thundat, M.J. Doktycz, "Glucose biosensing using an enzyme-coated microcantilever", *Appl. Phys. Lett.*, 81 (2002)

[Suresh, 2007] S. Suresh, "Nanomedicine: elastic clues in cancer detection," *Nature. Nanotechnology*, vol. 2, pp. 748-749 (2007)

[Thaysen, 2001] J. Thaysen, Technical University of Denmark, Thesis (2001)

[Tortonesi, 1993] M. Tortonesi, R. C. Barrett, and C. F. Quate, "Atomic resolution with an atomic force microscope using piezoresistive detection", *Appl. Phys. Lett.* 62, 834 (1993)

[Vettiger, 2000] P. Vettiger, M. Despont, U. Drechsler, U. Dürig, W. Häberle, M. I. Lutwyche, H. E. Rothuizen, R. Stutz, R. Widmer, G. K. Binnig. *IBM Journal of Research and Development*, Volume: 44 Issue: 3 (2000)

[Wei, 2010] Z. Wei, D. Wang, S. Kim, S.-Y. Kim, Y. Hu, M. K. Yakes, A. R. Laracuente, Z. Dai, S. R. Marder, C. Berger, W. P. King, W. A. de Heer, P. E. Sheehan, E. Riedo. *Science* 328, 1373-1376 (2010)

[Wetzig, 2006] K. Wetzig, C. M. Schneider, "Metal Based Thin Films for Electronics", Edition: 2, Published by Wiley-VCH (2006)

[Williams, 1986] Williams, C. C.; Wickramasinghe, H. K., "Scanning thermal profiler", *Applied Physics Letters*, Volume 49, Issue 23 (1986)

[Wisitsoraat, 2007] A. Wisitsoraat, V. Patthanasetakul, T. Lomas, A. Tuantranont, "Low cost thin film based piezoresistive MEMS tactile sensor", *Sensors & Actuators A* 139 (2007)

[Witt, 1974] G. R. Witt, "The Electromechanical Properties of Thin Films and the Thin Film Strain Gauge", *Thin Solid Films*, 22

(1974)

[Wood, 1993] A. Wood, "Use of vanadium oxide in microbolometer sensors", Patent #5450053 (1993)

[Wu, 2001] G.H. Wu, R.H. Datar, K.M. Hansen, T. Thundat, R.J. Cote, A. Majumdar, "Bioassay of prostate-specific antigen (PSA) using microcantilever", *Nat. Biotechnol.*, 19, 856-60 (2001)

[Wu, 2007] B. Wu, A. Ho, N. Moldovan, H.D. Espinosa. *Langmuir* 23:9120–9123 (2007)

[Wu, 2008] J.Wu, M.Reading, D. Q. M. Craig, "Application of Calorimetry, Sub-Ambient Atomic Force Microscopy and Dynamic Mechanical Analysis to the Study of Frozen Aqueous Trehalose Solutions", *Pharma. Research*, v 25 (6), pp. 1396-1404 (2008)

[Yinon, 2003] J. Yinon, "Detection of explosives by electronic noses", *Anal. Chem.*, 75, 99A-105A (2003)

[Yue, 2010] Z. Yue, X. Liu, "A Preliminary Study of Micro Heat Conduction by Hot-Tip Tribological Probe Microscope", *Key Engineering Materials* Vol. 437 (2010)

[Zellers, 2007] E. T. Zellers, W. H. Steinecker, M. P. Rowe, G. R. Lambertus, S. M. Reidy, J. A. Potkay, H. Kim, C. Avery, H. K. Chan, R. D. Sacks, K. Najafi, L. P. Bernal, and K. D. Wise, "A MEMS Gas Chromatograph for Determination of Toxic Industrial Chemical Mixtures," *Pittcon* (2007)

[Zhang, 2002] M. Zhang, D. Bullen, S.-W. Chung, S. Hong, K. S. Ryu, Z. Fan, C. Mirkin, C. Liu, "MEMS nanoplotter with high-density parallel dip-pen nanolithography probe arrays", *Nanotechnology* 13 212-217 (2002)

[Zhu, 2011] W. Zhu, J. S. Park, J. L. Sessler, and A. Gaitas, *Appl. Phys. Lett.* 98, 123501 (2011)

Summary

This dissertation aims to advance the current state of cantilevers with integrated metal thermal and deflection sensing elements. Metallic sensing elements enable the use of alternative substrate materials (such as polymers), that tend to exhibit higher compliance properties and are more robust (less brittle) compared to Si or Si₃N₄ cantilevers. To this end, the research consists of exploring the properties of thin films with thicknesses of 100 nm or less and studying a number of applications in thermal sensing, micro-heating, and deflection sensing. In order to achieve these goals three fabrication processes for microcantilevers were developed.

The minimum detectable temperature change of a cantilever with the 10 nm gold thermal sensing element was measured at 0.4 K, corresponding to 17 ppm changes in probe resistance. Finite element analysis simulations indicate a strong correlation between thermal probe sensitivity and probe tip curvature, suggesting that the sensitivity of the thermal probe can be improved by increasing the probe tip curvature, though at the expense of the spatial resolution provided by sharper tips. Simulations also indicated that new designs such as a bow-tie metallization design could yield an additional 5- to 7-fold increase in sensitivity.

The gauge factor of the thin film is enhanced to 3.24 for a 10 nm gold sensor and 4.1 for the 5 nm gold sensor doubling that of bulk gold. The sensors on silicon cantilevers exhibited large dynamic range of tens of microns and were used to measure: the mechanical properties of materials, the melting points of materials, topographical imaging, and high throughput measurements.

Moving nano-heater were used to direct chemical vapor deposition reactions (nano-CVD) demonstrating a tip-based nanofabrication

(TBN) method. The silicon cantilevers with embedded thin film heaters were used for localized nano-CVD to grow copper (Cu) and copper oxide (CuO) from gases.

Polyimide cantilevers with thin metallic sensing elements were coated with colorimetric sensing material and used for explosive detection enhancing the sensitivity by 30x compared to what was previously found when the colorimetric sensing material was used alone.

Metal thin films on cantilevers with thicknesses <10 nm exhibited temperature coefficients approaching 0.95%/K demonstrating that these devices can be used as bolometers.

In addition to the micromachined devices developed and the new findings in terms of enhanced performance, simple scanning systems and new methods of characterizing thermal probes were developed. These new systems include a calibration sample consisting of a 1 μm -wide gold wire, which can be heated electrically by a small bias current. The Joule heating in the calibration sample wire is characterized using noise thermometry and then the thermal probe is scanned in contact over the gold wire measuring temperature changes.

Samenvatting

Dit proefschrift heeft tot doel de huidige stand van zaken weer te geven van cantilevers bedekt met dunne metaallagen welke als thermische- en doorbuigingssensoren kunnen worden gebruikt. Vergeleken met doped-silicon sensoren hebben metaalfilm sensoren een belangrijk voordeel zoals eenvoudiger vervaardiging, lagere productie kosten en de mogelijkheid tot het verder terug schalen van de afmetingen met behoud van de gevoeligheden.

Metaalfilm sensoren maken het ook mogelijk om alternatieve substraat materialen te gebruiken (zoals polymeren), die blijk geven van een grotere flexibiliteit in de eigenschappen en zijn daarom robuuster (minder broos) vergeleken met Si of Si₃N₄ cantilevers.

Het onderzoek bestaat uit het verkennen van de eigenschappen dunne folies met een dikte van minder dan 10 nm en bestuderen van een aantal toepassingen in de wereld van de thermische sensoren, micro-heating en verplaatsingssensoren. Om deze doelen te verwezenlijken zijn drie nieuwe fabricatie processen voor micro cantilevers ontwikkeld.

De kleinst detecteerbare temperatuurverandering welke werd gemeten met een temperatuursensor bestaande uit een substraat met een 10 nm goudlaag was 0,4 K, wat overeenkomt met 17 ppm verandering in de probe weerstand. Simulaties met behulp van de eindige elementen methode laten een sterke correlatie zien tussen de gevoeligheid van de thermische sensor en de kromming van de probe tip, dit suggereert dat de gevoeligheid van de thermische sensor verbeterd kan worden door een toename van de kromming van de probe tip, hoewel dit ten koste gaat van de ruimtelijke resolutie die door de scherpere tips geboden wordt.

Simulaties lieten tevens zien dat nieuwe ontwerpen zoals het toepassen van “bow-tie” metallisatie ontwerp kan een 5 tot 7 voudige toename van de gevoeligheid opleveren.

De gauge-factor van de dunne film is verhoogd naar 3,24 voor een 10 nm dik goudlaagje waarmee de sensor is opgebouwd en 4,1 voor een sensor die met een 5 nm dikke goudlaag is opgebouwd hetgeen een verdubbeling is ten opzichte van dat van bulk-goud. De sensoren op silicium cantilevers vertoont een groot dynamisch bereik van tientallen microns en werden gebruikt om te meten: de mechanische eigenschappen van materialen, voor het bepalen van smeltpunten van materialen, topografische imaging en het meten bij grote doorvoersnelheden.

Polyimide cantilevers met sensoren opgebouwd uit dunne metaallagen welke werden bedekt met een colorimetrisch sensor materiaal en gebruikt worden voor het detecteren van explosieven vergrootte de gevoeligheid met 30x vergeleken met wat eerder gemeten werd toen alleen het colorimetrisch sensor materiaal werd gebruikt.

Dunne metaal films op cantilevers met een dikte van < 10 nm laten temperatuur coëfficiënten zien die 0,95%/K benaderen en uitwijzen dat deze sensoren als bolometers gebruikt kunnen worden.

Naast de micromachined ontwikkelde componenten en de nieuwe doorbraken op het gebied van verbeterde prestaties als gevolg van dunnere sensormaterialen zijn eenvoudige scan-systemen ontwikkeld en beschreven alsmede nieuwe methoden om thermische sensoren te karakteriseren. Deze nieuwe systemen omvatten een ijkmonster welke een 1 μ m brede gouden draad bevat, welke elektrisch kan worden opgewarmd door een kleine instelstroom.

De Joule opwarming in het ijkmonster wordt gekarakteriseerd door gebruik te maken van noise thermometrie waarbij de thermische probe wordt gescanned in vergelijking met de temperatuur veranderingen in de gouden draad.

Acknowledgements

This thesis would have not been possible without help from the following individuals. I hope I can be there for them as they were for me. I also hope that this work makes a small contribution to science and technology and proves to be useful to someone in the future.

First, I want to acknowledge Prof. Paddy French for recognizing that, perhaps, I have something noteworthy to say and put into a thesis format. He allowed me to be part of the Delft program and mentored me throughout. Equally importantly, I wanted to acknowledge Prof. Yogesh Gianchandani for being my mentor, friend, and advisor for more than a decade. Thank you for putting up with me and for giving me several breaks.

There are two people without whom this work would have not been possible, Dr. Weibin Zhu and Dr. Tao Li, both worked with me for many years and I really owe them a huge thanks. They are both my friends and colleagues. Our joint work produced several of these devices.

Prof. Kurdak for his mentorship, help, and for teaching me several very interesting concepts in Physics as well as guiding me in the work presented in Chapters 5 and 10. Prof. Sessler for help on the chemical sensing project (Chapter 9). I want to thank Dr. Amar Basu for his mentorship, friendship, and help.

I want to acknowledge the National Science Foundation and the National Institutes of Health for providing with the funding through several grant awards.

I am thankful for my parents support. My mother instilled in my interest in science. My father always encouraged and supported me

182

throughout my endeavors. Last but not least, Kristin Ledgerwood for her support and patience.

This thesis is dedicated to my dear brother, Alex Gaitas, 1979-2009.

List of Publications

Journal Publications

1. A. Gaitas, "Polyimide Probes For Contact Mode Subsurface SPM Thermal Imaging", *Microscopy and Analysis* (2006)
2. A. Gaitas And Y. B. Gianchandani, "An Experimental Study of Contact Mode Scan Speed Constraints For Polyimide Cantilever Probes", *Ultramicroscopy* (2006)
3. A. Gaitas, "A Preliminary Study of Spatial Resolution Enhancement of Confocal and Triangulation Displacement Meters Using Contact Mode Scanning Probes", *Rev. Sci. Instrum.* (2008)
4. B. Mitra, A. Gaitas, "Thermally actuated tapping mode atomic force microscopy with polymer microcantilevers", *Rev. Sci. Instrum.* (2009)
5. A. Gaitas, W. Zhu, N. Gulari, E. Covington, C. Kurdak, "Characterization of Room Temperature Metal Microbolometers near the Metal-Insulator Transition Regime for Scanning Thermal Microscopy," *Applied Physics Letters* (2009)
6. A. Gaitas, S. Gianchandani, W. Zhu, "A Piezo-Thermal Probe for Thermomechanical Analysis", *Review of Scientific Instruments* (2011)
7. A. Gaitas, T. Li, W. Zhu, "A Probe With Ultrathin Metal Piezoresistive Sensor for Scanning Probe Microscopy and Material Characterization", *Sensors and Actuators* (2011)

8. W. Zhu, J. S. Park, J. L. Sessler, A. Gaitas, "A Colorimetric Receptor Combined With A Microcantilever Sensor For Explosive Vapor Detection", *Applied Physics Letters* (2011)
9. A. Gaitas, P. French, "Piezo-thermal probe array for high throughput applications", *Sensors and Actuators. A: Physical* (2012)
10. A. Gaitas, S. Wolgast, E. Covington, C. Kurdak, "Hot spot detection and Johnson noise thermometry calibration of a bolometer type scanning thermal probe", *Journal of Applied Physics* (2013).
11. A. Gaitas, "Tip-based chemical vapor deposition with a scanning nano-heater", *Applied Physics Letters* (2013)
12. A. Gaitas, B. McNaughton, "Nickel Foil Microprobes For Magnetic Manipulation and Localized Heating", under review (2013)
13. A. Gaitas, R. Malhotra, K. Pienta, "A new method to measure adhesion utilizing a polymer micro-cantilever", *Applied Physics Letters* (2013)

Conference Publications (Presentations or Posters)

1. V. Petrashov, I. Sosnin, A. Gaitas, A. Parsons, "Deviations from the Kohler Rule in Mesoscopic Conductors", *Conference of Condensed Matter and Materials Physics* (1998)
2. K. Lai, A. Gaitas, R. Yang, C. Fung and N. Xi, "Ultra-compliant Thermal AFM Probes for Studying of Cellular Properties", *IEEE NANO* (2010)

3. A. Gaitas, Y.B. Gianchandani, "Polyimide probes for contact mode high-speed Atomic Force Microscopy imaging", Seventh International Conference on Scanning Probe Microscopy, Sensors and Nanostructures (2005)
4. A. Gaitas, S. Xu, "High Resolution Scanning Thermal Microscopy Using Polymer Probes With Embedded Metal Thermistors", Seventh International Conference on Scanning Probe Microscopy, Sensors and Nanostructures (2005)
5. S. Wolgast, C. Kurdak, A. Gaitas, W. Zhu, "Measuring Transport Properties Of Thin Films, Under Isotropic And Anisotropic Strain Using Piezoelectric Substrates", APS, Volume 56, No 1 (2011)
6. A. Gaitas, P. French, "Magnetic Microheaters For Cell Separation, Manipulation, And Lysing", The 16th International Conference On Solid-State Sensors, Actuators and Microsystems (2011)
7. K. Lai, A. Gaitas, N. Xi, R. Yang, Fung, "Development And Testing of Nano Robot End Effector For Cell Electrophysiology and Elastography Studies", Proceedings of The IEEE Nano (2011)
8. A. Gaitas, P. French, "Piezoresistive Probe Array For High Throughput Applications", Eurosensors XXV (2011)

Patents

(out of 5 issued and 3 pending - pending not listed)

1. 8,394,625; Lab-on-a-pipette
2. 8,326,838; Education credentials management method and system

3. 8,297,837; Metal and semimetal sensors near the metal insulator transition regime
4. 8,192,809; Scanning probe assisted localized CNT growth
5. 8,156,568; Hybrid contact mode scanning cantilever system

About the author

Angelo Gaitas was born in Athens, Greece. After graduating from the University of Wales-Swansea with a Bachelor in Physics and Mathematics, Angelo obtained a Master in Research in Mesoscopic Physics and Nanotechnology from the University of London - Royal Holloway College with a Distinction in 1998. He worked in Athens, Greece and the Minneapolis, Minnesota, USA. He completed a short internship at the Department of Energy in Washington DC in 2000 and then went on to pursue a Master in Business Administration (MBA) from the University of Wisconsin in Madison graduating in 2002. He was employed, for a few years, as a Research Associate at the Electrical Engineering Dept. of the University of Michigan-Ann Arbor. He won several business plan competitions and with the proceeds founded PicoCal Inc. with Professor Gianchandani. During his tenure at PicoCal Inc. he commercialized several products. In addition, he served as a Principal Investigator on 8 US government funded grants from the National Science Foundation and the National Institutes of Health bringing in and managing over \$1,700,000. At PicoCal he managed, mentored, and taught several employees including recent PhD graduates and several undergraduates doing their internships or projects with the company. He has 13 journal and 8 conference publications, 5 issued and 3 pending US patents. He has served on proposal review panels for the National Science Foundation and the National Institutes of Health. He has served as a reviewer for the following journals: Ultramicroscopy, Sensors and Actuators, and Sensor. Finally, he served as the Exhibition Chair of the IEEE Nanotechnology Materials and Devices Conference 2009. Angelo is fluent in English, Spanish, and Greek.

